

DOCTOR OF PHILOSOPHY

Fatigue crack initiation and small crack propagation in additive manufactured Ti-6Al-4V

Shamir, Muhammad

Award date:
2022

Awarding institution:
Coventry University

[Link to publication](#)

General rights

Copyright and moral rights for the publications made accessible in the public portal are retained by the authors and/or other copyright owners and it is a condition of accessing publications that users recognise and abide by the legal requirements associated with these rights.

- Users may download and print one copy of this thesis for personal non-commercial research or study
- This thesis cannot be reproduced or quoted extensively from without first obtaining permission from the copyright holder(s)
- You may not further distribute the material or use it for any profit-making activity or commercial gain
- You may freely distribute the URL identifying the publication in the public portal

Take down policy

If you believe that this document breaches copyright please contact us providing details, and we will remove access to the work immediately and investigate your claim.

Fatigue crack initiation and small crack propagation in additive manufactured Ti-6Al-4V

January 2022

*A thesis submitted in partial fulfilment of the University's requirement for the Degree of
Doctor of Philosophy*





Certificate of Ethical Approval

Applicant:

Muhammad Shamir

Project Title:

Effect of material defect on the fatigue and fracture properties of additive
manufactured high strength alloys

This is to certify that the above named applicant has completed the Coventry
University Ethical Approval process and their project has been confirmed and
approved as Low Risk

Date of approval:

07 February 2019

Project Reference Number:

P86748

Articles published during this PhD

Journal papers:

1. **Shamir M**, Syed AK, Janik V, Biswal R, Zhang X. The role of microstructure and local crystallographic orientation near porosity defects on the high cycle fatigue life of an additive manufactured Ti-6Al-4V. *Materials Characterization* 2020;169:110576. <https://doi.org/10.1016/j.matchar.2020.110576>

2. **Shamir M**, Zhang X and Syed AK. Characterising and representing small crack growth in an additive manufactured titanium alloy. *Engineering Fracture Mechanics* 2021;253:107876 <https://doi.org/10.1016/j.engfracmech.2021.107876>

Contribution to following publications

Journal papers:

3. Biswal R, Zhang X, **Shamir M**, Al Mamun A, Awd M, Walther F, et al. Interrupted fatigue testing with periodic tomography to monitor porosity defects in wire + arc additive manufactured Ti-6Al-4V. *Additive Manufacturing* 2019;28:517–27. <https://doi.org/10.1016/j.addma.2019.04.026>

4. Syed AK, Zhang X, Caballero A, **Shamir M**, Williams S. Influence of deposition strategies on tensile and fatigue properties in wire + arc additive manufactured Ti-6Al-4V. *Int Journal of Fatigue* (Accepted 4.4.2021) <https://doi.org/10.1016/j.ijfatigue.2021.106268>

Acknowledgement

I want to pay my profound gratitude to Professor Xiang Zhang and Dr Abdul Khadar Syed for their tiring efforts and continuous support during my whole PhD, especially during these challenging times where we are locked down in our homes. It would not have been possible for me to conclude my research without their sincere guidance and encouragement. I would also like to thank Dr Vit Janik and Wayne Sadler for helping me with my experiments.

I am also very grateful to Coventry University and BAE Systems for jointly funding this PhD, Cranfield University team, especially Professor Stewart Williams and Dr Jialuo Ding, for providing the experimental material for this research. I extend my appreciation to the technical staff working in the workshop and laboratories; Mr Barry Meek, Mr Steven Allitt, Mr Steve Damms, Mr Martyn Cockell.

To the most amazing and supportive group of friends of our tea-time; Dr Ibrahim Almakky, Dr Romali Biswal, Dr Rohit Kshirsagar, Anees Abu-Monshar, Mohamed Marei, Shirine El Zaatari, who continued to inspire during these challenging times even though we were thousands of miles apart. I would also like to thank Emre Akgun, Mitchell Leering, Dr Yiding Liu and Dr Yao Li for their guidance and support. Apart from Academia, I am very much thankful to Dr Fahd Nawaz Khan, Dr Adil Khan, Dr Arpit Goyal and Dr Adul Rehman for their constant motivation.

Finally, I am sincerely grateful to my parents and siblings for their countless prayers, love, and belief in me, my wife Ayesha and my son Mohid for their love, continuous struggle, and utmost support throughout my PhD.

Abstract

This research aims to quantify the effect of as-deposited surface on crack initiation and early-stage propagation in a wire + arc additive manufactured Ti-6Al-4V (WAAM Ti64). The main objectives were: 1) to conduct fatigue testing and microstructural examination of specimens in the as-deposited conditions; 2) to develop a model to predict a fatigue life; 3) to study the effect of crystallographic orientations of grains surrounding a defect on crack initiation and small crack propagation. To achieve these objectives, fatigue testing and numerical modelling were designed and conducted. Key findings are summarised below.

Firstly, specimens with as-deposited surface were tested under bending fatigue load. The surface waviness feature was characterised using a metrology tool and represented as "groove" or "notch" as in the classic fatigue method. Therefore, fatigue life prediction was based on the stress concentration factor of the centre notch geometrical profile using the notch-stress approach. A range of values representing the shallowest and deepest notches in the WAAM Ti64 build was investigated. The model has worked well for test samples under higher applied stresses while it over-estimated the fatigue life at lower applied stresses.

An alternative approach was subsequently proposed based on the fracture mechanics method assuming the surface notch as an initial crack length based on the equivalent initial flaw size (EIFS) concept. Given the notch size being sub-mm range, small crack growth testing was performed using a recommended geometry by ASTM E647 standard. It was found that small cracks grow faster than long cracks under the same applied stress intensity factor. Hence small crack data must be used to estimate the fatigue life of AM parts containing defects.

Furthermore, the small crack test data was used to verify the Hartman-Schijve variant of NASGRO equation that only requires testing a long crack specimen. Based on this work, a recommendation was made to use long crack data to predict small crack growth behaviour. Moreover, a unified crack growth rate curve was computed using the Hartman-

Schijve equation, and as a demonstrator, it was further used for the durability prediction of another geometry in as-deposited condition. Predicted life was found to be slightly conservative compared with the notch stress approach.

Finally, microstructure characterisation of internal gas pores was conducted showing one of the reasons for fatigue test scatter in WAAM Ti64 being the variation in the α lath crystallographic orientation and its width in the vicinity of the crack initiating pore. Pyramidal slip systems with high Schmid factor and smaller α laths resulted in longer fatigue life.

In summary, a unified crack growth curve was proposed and verified by small crack experimental data. The model capability was demonstrated by durability analysis of as-deposited WAAM Ti64 and found to be in good agreement with the test result. The fracture mechanics based approach is more suitable for durability analysis of AM parts containing defects as the crack length is included in the model. Nevertheless, the classical notch stress method has also worked well for predicting the crack initiation life from sub-mm notches. The microstructural analysis has shown that the durability of AM parts with defects could be improved by reducing the α lath width and/or increasing the number of active pyramidal slip systems.

Table of contents

Publications.....	i
Acknowledgement.....	ii
Abstract.....	iii
List of Figures.....	viii
List of Tables.....	xiv
Chapter 1. Introduction.....	1
1.1 Background and motivation.....	1
1.2 Aim and objectives.....	4
1.3 Thesis Structure.....	5
Chapter 2. Literature review: AM processes, their microstructure and defect occurrence.....	7
2.1 Introduction.....	7
2.2 Additive manufacturing.....	8
2.2.1 Powder bed AM processes.....	9
2.2.2 Powder feed AM process.....	9
2.2.3 Wire feed AM processes.....	10
2.3 Metallurgy of Titanium.....	11
2.4 Defects in the AM process.....	15
2.5 Characterisation AM defects.....	18
2.6 Mechanical properties of AM parts.....	20
2.6.1 Tensile and hardness.....	20
2.6.2 Fatigue properties.....	22
2.7 Fatigue life prediction models.....	24
2.8 Summary.....	27
Chapter 3. Theoretical framework and methodologies.....	29
3.1 Introduction.....	29
3.2 Notch fatigue method.....	30
3.2.1 Material property ($S-N$, $\varepsilon-N$).....	30
3.2.2 Cyclic stress-strain relation.....	32
3.2.3 Stress raisers in part and life prediction.....	33
3.3 Fracture mechanics based approach.....	36
3.3.1 Small crack growth rate.....	39
3.4 Summary.....	49
Chapter 4. The behaviour of small fatigue cracks in WAAM Ti-6Al-4V.....	51
4.1 Introduction.....	51
4.2 Experimental procedures.....	52
4.3 Results and discussion.....	54
4.4 Calculation of the stress intensity factor.....	61
4.4.1 FE modelling of EDM notch.....	65
4.5 Predicting small crack growth behaviour.....	67
4.6 Summary.....	71
Chapter 5. Durability of as-deposited WAAM Ti-6Al-4V: Experimental investigation.....	73
5.1 Introduction.....	73
5.2 Materials and methods.....	74

5.2.1	Material manufacturing	74
5.2.2	Surface roughness characterisation	75
5.2.3	Characterisation of a single notch	77
5.2.4	Fatigue testing.....	79
5.3	Results and discussion	80
5.3.1	Effect of surface waviness on fatigue.....	80
5.3.2	Microstructure and crack path in as-deposited 3PB samples	82
5.3.3	Fracture mechanism.....	85
5.4	Summary	87
Chapter 6. Durability of as-deposited WAAM Ti-6Al-4V: Modelling.....		89
6.1	Introduction.....	89
6.2	Notch-stress approach.....	89
6.2.1	Stress concentration factor of a typical notch in as-deposited surface	89
6.2.2	Fatigue life prediction.....	92
6.3	Fracture mechanics approach.....	94
6.3.1	Calculation of stress intensity factor by FEM	94
6.3.2	Fatigue life prediction.....	97
6.4	Summary	100
Chapter 7. Effect of microstructure and crystallographic orientation on fatigue life scatter..		101
7.1	Introduction.....	101
7.2	Materials and experimental methods	102
7.3	Results and discussions.....	104
7.3.1	Fatigue life and fractography.....	104
7.3.2	Crack initiation from embedded defects.....	106
7.3.3	Crack initiation from surface defects.....	111
7.4	Summary	115
Chapter 8. Conclusions and future work.....		117
8.1	Conclusions.....	117
8.1.1	Small crack growth testing	117
8.1.2	Fatigue behaviour of as-deposited WAAM Ti64	118
8.1.3	Fatigue life prediction methods	119
8.1.4	Microstructure effect on fatigue test scatter	120
8.2	Future work.....	120

List of Figures

Figure 1.1: Research roadmap for durability assessment of WAAM Ti64 in as-deposited condition. 6

Figure 2.1: Schematic representation of (a) laser-based powder bed fusion process, (b) wire + arc-based directed energy deposition process, (c) laser-based directed energy deposition process [57]. 10

Figure 2.2: Different types of Ti64 microstructure formed as a result of different cooling rates and processing conditions; (a) forged and mill annealed Ti64 [61] (b) directed energy deposition laser metal wire deposition (cooling rate = 7×10^6 °C/min) [45,62] (c) laser powder bed fusion (cooling rate = 10^4 - 10^6 °C/min) [45,63]. 12

Figure 2.3: Thermal history of WAAM Ti64 calculated from FEA during deposition of the first ten layers [12]. 13

Figure 2.4: (a) Young's modulus (E) of α -Ti single crystal as a function of loading direction with respect to the c-axis (b) The unit cells of α phase (hcp) and β phase (bcc). Reproduced from [42] 14

Figure 2.5: Schematic representation of the twin boundary and the adjacent atoms [66]. 14

Figure 2.6: Porosity defect found in (a) electron beam melting [71] (b) wire + arc additive manufacturing [13]. 16

Figure 2.7: LoF defects in different AM Ti64 (a) selective laser melting (SLM) [81] (b) electron beam melting (EBM) [82] (c) laser metal wire deposition (LMwD) [67]. 17

Figure 2.8: Comparison of as-deposited electron beam melting surface and selective laser melting surface with the machined surface [80]. 18

Figure 2.9: (a) micro-CT examination of porosity defects in WAAM Ti64 where porosity was induced intentionally [72] (b) aspect ratio vs. sphericity visualisation characterised by μ -CT for Ti64 [95]. 20

Figure 2.10: Effect of porosity on tensile properties of WAAM Ti64 [13]. 21

Figure 2.11: Effect of surface roughness and HIPing on fatigue performance of Ti64. All tests were conducted at R = 0.1. [5,27,108,109]. 23

Figure 2.12: Correlation between fatigue life at two different stress levels and square root of R_a (a) $R = -1$ data, (b) $R = 0.1$ data [24].	24
Figure 2.13: FE model using X-ray computed tomography (CT) scanned geometry, meshing using image-based FE algorithm (b) variation of stress concentration factor at the root of the pore A with distance x_1 from the free surface compared with idealised pore geometry.	26
Figure 3.1: Different phases of fatigue life and relevant factors reproduced from [122].	29
Figure 3.2: The total strain amplitude vs. life obtained from the elastic and plastic strain amplitude superposition, reproduced from [125].	31
Figure 3.3: (a) Schematic of stress distribution around an open hole [127], (b) FE model showing stress distribution around the open hole in a wide plate.	34
Figure 3.4: (a) crack in a plate, (b) schematic representation of the da/dN vs. ΔK in a double-logarithmic plot with the Paris law represented as a straight line.	39
Figure 3.5: Different phases of fatigue life and relevant factors modified by [132].	40
Figure 3.6: Kitagawa-Takahashi diagram for transition crack length [134,135].	41
Figure 3.7: Comparison of long crack growth data of AM Ti64 tested at $R=0.1$ [34,35,119,139].	43
Figure 3.8: Comparison of microstructurally small and long crack growth data of LENS Ti64 tested at $R=0.1$ [139]	44
Figure 3.9: (a) Plot of da/dN vs. $\Delta \kappa$ for determining material constants D and p of Ti64 by the fitting curve, (b) da/dN vs. ΔK experimental data and prediction [41].	47
Figure 4.1: (a) Schematic of the WAAM Ti64 wall showing welding torch movement direction and sample extraction plan, (b) compact tension specimen for a long crack test, (c) geometry and dimensions of tensile sample (d) small crack sample and starter notch. [WD: welding torch movement direction, TD: transverse (thickness) direction, ND: normal direction. Unit: mm, not to scale.]	53
Figure 4.2: (a) Lower magnification optical micrographs of ND-TD plane for showing columnar primary β -grains and heat-affected zone (HAZ) bands, (b) SEM image of basketweave alpha microstructure found between two columnar primary β grains (c) SEM secondary electron (SE) high magnification images showing typical transformation microstructure.	55

Figure 4.3: Tensile test curves of three vertical extracted samples	56
Figure 4.4: Evolution of the lead crack at different number of cycles in the interrupted test of small crack samples; (a) SC-Test-1, (b) SC-Test-2	57
Figure 4.5: (a) Schematic of actual and projected crack length (b) evolution of tortuosity (tortuosity = actual crack length/projected crack length) of a lead crack in each test. Note: actual crack length was measured using ImageJ	58
Figure 4.6: Local crack front configuration with two adjacent areas A and B having different crystallographic orientations and therefore differently oriented major slip planes, i.e. crack planes (adapted from [42]).	60
Figure 4.7: (a) Small crack test results: (a) a vs. N ; crack length was measured by replication of the lead crack, and the projected crack length was plotted, (b) da/dN vs. a . (Note: crack length includes the notch size).	59
Figure 4.8: (a) Secondary electron SEM image of a typical fracture surface of the small crack sample showing the EDM starter notch, crack initiation location from the notch, crack propagation FE modelling benchmark direction, and fast fracture region, (b) Higher magnification image of the starter notch and dimensions, (c) optical microscopy image of the starter notch before the start of the test.	62
Figure 4.9: Schematic showing crack tip displacement adapted from [130].	62
Figure 4.10: The half model of quarter elliptical corner crack sample showing (a) partition definition and boundary condition (b) meshing strategy and mesh refinement around the crack front (c) mesh distribution near the crack front.	63
Figure 4.11: (a) S33 stress contour maps around quarter-elliptical corner crack (b) U3 displacement field in ND-TD plane, (c-f) K values calculated by displacement extrapolation method for CL-1, CL-2, CL-3 and CL-4, respectively. Applied stress was 150 MPa for this illustration	64
Figure 4.12: Finite element model of one-half of the test sample: (a) starter notch with a small crack extension of 0.1 mm, load and boundary conditions, (b) FE mesh, (c) and (d) contour maps of stress in load direction (S33). Applied stress was 150 MPa for this illustration.	66
Figure 4.13: Calculated stress intensity factor for the small crack sample with initial notch being modelled as quarter-elliptical shape (Newman-Raju eq.) or triangular (FEA). Applied stress = 150 MPa, crack length includes notch size.	67

Figure 4.14: da/dN vs. ΔK for the long crack (LC) [119,162] and small crack (SC) samples tested in this study. The long crack data shows small cracks growing faster under the same applied ΔK 67

Figure 4.15: H-S equation fitted to long crack test data: (a) da/dN vs. Δk for determining material constants D and p by the fitting curve, (b) da/dN vs. ΔK . Material data used in eq. (3.21): $A = 90 \text{ MPam}$ and $\Delta K_{th} = 4.5 \text{ MPam}$ 69

Figure 4.16: Prediction of small crack growth rate using long crack data fitted H-S equation with $\Delta K_{thr} = 2 \text{ MPam}$, and comparison with a prediction in the literature on SLM Ti64 [111]. 71

Figure 4.17: Small crack behaviour and comparison of test results with prediction using eq. (3.21): (a) da/dN vs. a , (b) a vs. N (Note: crack length includes the notch size.) 70

Figure 5.1: (a) Photo of an actual WAAM Ti64 wall built by single-pass deposition method (b) schematic of WAAM Ti64 wall and sample extraction plan (c) location of sample extraction along thickness direction (d) geometry and dimensions of a bending test sample (unit: mm), WD = welding torch movement direction, TD = transverse (thickness) direction, ND = normal direction. 74

Figure 5.2: Schematic representation of surface roughness parameters: the arithmetical mean height, R_a , the maximum valley depth, R_y , while R_z is the average value of five R_y (eq. (5.3)) 76

Figure 5.3: (a) Schematic showing surface characterisation of as-deposited WAAM Ti64 using a form tracer, (b) three-line scans on each sample at a distance of approx. 5 mm. 78

Figure 5.4: Procedures for measurement of notch configuration parameters, starting from identifying notch to optical microscope image of the notch along the TD-ND plane overlapped with metrology data taken from form tracer (FT) and spline created using metrology data to calculate r of the notch. 80

Figure 5.5: (a) 3PB fatigue test setup showing the position of the supporting rollers and plunger with the as-deposited surface facing downwards. Schematic of 3PB fatigue testing of (b) as-deposited sample, (c) machined sample. 79

Figure 5.6: $S-N$ data of three-point bending tests for machined and as-deposited WAAM Ti64 samples. Y-axis represents the maximum bending stress on the beam centre. 81

Figure 5.7: Three-point bending fatigue test setup showing monitoring of crack initiation and propagation from a centre “notch”, which was one of the “dents” caused by as-deposited surface waviness.....	83
Figure 5.8: 3PB-Test 1 ($\sigma_{\max}=380$ MPa, $N_f=74,000$): Global macroscopic image showing the crack path and detailed zoom views: (a) crack branching near prior beta grain boundary, (b) primary crack arrest at $\sim 46,000$ cycles, (c) secondary crack initiation ~ 10 μm away from the primary crack.	83
Figure 5.9: 3PB-Test 2 ($\sigma_{\max}=380$ MPa, $N_f=33,000$): Global macroscopic image showing the crack path and detailed zoom views: (a) lead crack growing in a transgranular manner, (b) branching and coalescence of lead crack at $\sim 14,000$ cycles, (c) secondary crack branching and arrested at around 10 μm away from the lead crack.	84
Figure 5.10: Crack growth history of the lead crack measured with the travelling microscope. 3PB-Test 1 ($\sigma_{\max}=380$ MPa, $N_f=74,000$) 3PB-Test 2 ($\sigma_{\max}=380$ MPa, $N_f=33,000$) and 3PB-Test 3 ($\sigma_{\max}=380$ MPa, $N_f=110,000$).....	85
Figure 5.11: Fracture surfaces for (a) polished samples tested at 800 MPa with $N_f=74,813$ (b) as-deposited surface, with arrows showing the crack growth direction tested at 500 MPa with $N_f=25,575$	86
Figure 5.12: Fracture surfaces showing different fracture regions in as-deposited sample tested at 500 MPa with $N_f=25,575$	87
Figure 6.1: Effect of notch mouth angle on stress concentration factor keeping r and d constant.....	90
Figure 6.2: (a) Finite element model for the sample tested in 3PB fatigue and zoom-in view of a single notch imported from FT data, (b) stress distribution along the notch area (where the notch is corresponding to “distance” = 1 mm, applied bending stress = 1 MPa)	92
Figure 6.3: S - N relation of fatigue life prediction based on K_t and experimental data of as-deposited and polished WAAM Ti64.....	93
Figure 6.4: The FE model of an SEN(B) geometry: (a) a line crack as in standard SEN(B) geometry and in reference [192], (b) notch+crack (where the notch mimics the surface roughness “dent”), (c) FE mesh used to model notch+crack.	95

Figure 6.5: Stress intensity factor vs crack length in 3PB sample, compared with [192].
..... 96

Figure 6.6: Calculated K as a function of crack length for 3PB samples 96

Figure 6.7: Schematic representation of as-deposited notch. 97

Figure 6.8: Predicted fatigue life for a WAAM Ti64 bending specimen in its as-deposited condition based on a small crack growth approach. 98

Figure 6.9: $S-N$ curve showing experimental data of as-deposited WAAM Ti64 and durability prediction based on the modified Hartman-Schijve equation. 99

Figure 7.1: Schematic illustration of (a) WAAM Ti64 wall, (b) geometry and dimensions of a fatigue sample (unit: mm, not to scale). Build direction was along with the ND, and torch movement was oscillated along with the TD for each layer. 102

Figure 7.2: (a) Example of a fracture surface showing the crack initiating defect, (b) schematic of a fractured sample showing sample extraction for EBSD analysis, (c) sample for EBSD analysis showing sectioned micrograph on the TD-WD plane and location of EBSD measurement area around crack initiating defect. 104

Figure 7.3: (a) Fatigue test results indicating defect location where the crack was initiated; redrawn from [13]; filled symbols represent samples selected for this study; (b) schematic of defect location and definition of distance to sample surface. Surface defects, if the $x/d < 0.8$ and embedded defects, $x/d > 0.8$ 104

Figure 7.4: Fatigue life and crack initiating defect size for samples under maximum applied stress 700 MPa (S1-S4), 600 MPa (S5, S6) and 500 MPa (S7-S9). 106

Figure 7.5: SEM images of fracture surfaces showing the embedded defect for the 700 MPa sample group. The crack initiating defect is indicated with an arrow. 108

Figure 7.6: EBSD orientation maps of 700 MPa fractured samples showing crack initiation location and Schmid factor distribution analysis. The build and loading directions are parallel to TD. The number of cycles to failure for S1, S2, S3 and S4 are 152×10^4 , 89×10^4 , 20×10^4 and 121×10^4 respectively. 110

Figure 7.7: SEM images of fracture surfaces showing the crack initiating defect (indicated with an arrow) for samples tested at 600 and 500 MPa. 111

Figure 7.8: EBSD orientation maps of 600 MPa fractured samples showing crack initiation location and Schmid factor distribution analysis in S5 and S6. The build and

loading direction is parallel to TD. The number of cycles to failure for S5 and S6 are 9×10^4 , and 160×10^4 respectively.	112
Figure 7.9: EBSD orientation maps of 500 MPa fractured samples showing crack initiation location and Schmid factor distribution analysis in S7, S8 and S9. The build and loading direction is parallel to TD. The number of cycles to failure for S7, S8 and S9 are 22×10^4 , 69×10^4 and 700×10^4 respectively.	113
Figure 7.10: Distribution of α lath size obtained from EBSD analysis for tests S7 and S8	114

List of Tables

Table 4.1: Comparison of Newman-Raju and FEA results	64
Table 6.1: Comparison of r calculated by eq. (6.1) and measured from OM.....	78
Table 7.1: Slip directions and slip planes in Ti64, used for Schmid factor calculation.	103
Table 7.2: Fatigue life of samples with the defect details that led to crack initiation ..	105

Chapter 1

Introduction

1.1 Background and motivation

Additive manufacturing (AM) of titanium alloy Ti-6Al-4V (Ti64) has received particular attention due to its widespread applications in the aerospace, biomedical, and other industries [1–6]. The high manufacturing and production cost and significant material wastage (approximately 90%) of high-value materials to produce final parts by traditional manufacturing methods also attracted significant interest from both industry and academia [7]. Apart from material savings, AM offers the capability to produce complex shapes through layer-by-layer deposition allowing more design flexibility and significant weight reductions in the parts produced by AM. The wire + arc additive manufacturing (WAAM) is a directed energy deposition (DED) AM process where a wire is fed into an electric or plasma arc heat source at a constant feed rate to build large near-net-shape parts at a much-reduced cost compared to powder-based AM processes [8,9]. The deposition rate of Ti64 by the WAAM process is approx. 2 kg/h as compared to 0.1 kg/h in selective laser melting and 1 kg/h in laser metal deposition [10,11]. Due to higher deposition rates and high heat input, residual stresses and distortions are higher in WAAM components. Furthermore, the larger layer height ranging between 0.8 and 2 mm results in higher surface roughness. Consequently, it needs machining as a final step.

All load-bearing parts on aero-structures must be designed to be durable and damage tolerant. Durability is related to the economic life of a component under cyclic loads, while damage tolerance is the ability of a structure to safely operate in the presence of defects or cracks until the damage becomes a critical size. The failure criteria for aero-engine components, such as turbine blades and discs, are based on fatigue crack initiation.

In contrast, airframe structural components such as wing and fuselage panels are designed for damage tolerance, i.e. based on the crack propagation life from initial crack length to critical crack size. AM is expected to provide a range of new materials within aerospace manufacturing. These newly developed processes and materials need to be tested for their durability and damage tolerance. There is limited literature available on the fatigue behaviour of WAAM Ti64. Wang et al. [12] only tested Ti64 build by single-pass deposition at a single stress level of 600 MPa. They demonstrated significantly better fatigue properties than the conventionally manufactured samples except for a few samples where the early crack initiation was found due to the process inherent defects degrading the fatigue life. Biswal et al. [13] performed fatigue testing of WAAM Ti64 made by the oscillation built strategy to see the material performance with and without internal porosity defects. It was concluded that defects not only considerably reduced the fatigue life but also caused a large scatter in the test result. The scatter in fatigue life in the defect containing WAAM parts is also associated with a local microstructure and crystallographic orientation around the defects [14].

Apart from internal defects, as-deposited surface roughness is also a concern in AM parts as it affects the fatigue performance of AM parts. However, surface machining cannot always be performed, especially for complex geometries. Furthermore, machining will also result in material waste, increase the buy-to-fly ratio and reduce the AM advantages such as net-shaped manufacturing. Moreover, parts with lower design life may not need to worry about the surface roughness. Therefore, having a profound understanding of surface roughness on fatigue performance can improve the post-deposition machining process, which could be prioritised for critical locations contributing significantly to the design optimisation. Surface roughness has been a topic of almost all AM processed materials and parts [4,15–18]. Depending on the AM process and raw materials, the as-deposited surface can be divided into two types. In the case of powder-based processes, the high occurrence of waves termed surface roughness, while in the case of wire feed processes, there are low-occurrence waves, termed as “waviness” [10,16].

To understand and quantify the impact of surface roughness on structural integrity, considerable research has been carried out on the tensile and fatigue properties of AM

parts with as-deposited surfaces [19–24]. The effect of surface roughness on fatigue behaviour is analysed through the surface roughness parameter R_a representing the general topography of the sample's surface. A higher R_a value generally means a rougher surface which consequently leads to lower fatigue life. However, despite being used by some researchers and as a general guideline for manufacturing, the R_a does not describe the critical effects of the crack initiation process as R_a is an average parameter [25,26]. Therefore, to further improve the quantification of fatigue life due to surface roughness, researchers have used other surface parameters, such as maximum valley depth, an average of five highest-profile depths and the peak height of the profile termed as R_y , R_z and R_t , respectively (further discussed in Chapter 5), or a combination of these parameters [27,28]. Furthermore, to achieve a more comprehensive understanding, the conventional fatigue notch stress model proposed by Neuber has been used in the literature to analyse the effect of small defects such as porosity and as-deposited surface roughness [29,30].

Recent research has also demonstrated that the durability of parts due to initial damage or defects can be predicted using the fracture mechanics approach [31]. In the analysis, the concept of equivalent initial flaw size (EIFS) was used to define the initial damage source, such as the defects, and the material's crack growth rate vs. applied stress intensity factor range is employed to calculate the fatigue life of the component. The defects and surface features found in AM are in the sub-millimetre range, and the current linear elastic fracture mechanics (LEFM) models hold limitations in the case of physical small cracks [32]. It has been further demonstrated that using long crack growth rate data can overestimate the fatigue life as the cracks initiating from defects or surface roughness are in the small crack domain, which grows faster than long cracks under the same value of applied stress intensity factor [33–35]. Furthermore, fatigue cracks of relevance to many structural applications are often small or short, and a significant portion of fatigue life is spent in growing small cracks [36]. Therefore, when adopting the fracture mechanics approach for durability analysis, there is a need for small crack growth rate data. Owing to the absence of a standardised approach for small crack growth test and the time and cost constraints in testing small cracks, designers for aerospace structures often do not test small crack propagation behaviour [37]. Hence, for durability analysis of conventional and AM materials, empirical models representing the small crack growth

behaviour by testing only the long crack specimens have been proposed and is shown to be able to predict small crack growth rate for a range of aerospace and rail materials tested at a variety of cyclic load ratios [32,38–41].

The small cracks grow faster than long cracks in conventional materials and therefore should be used to predict the fatigue life in the presence of sub-millimetre defects. However, there is no such study available for WAAM Ti64. To further use this small crack data to predict fatigue life, there is a subsequent need for unified crack growth laws. The Hartman-Schijve variant of the NASGRO equation is one such method, but it needs to be verified for the small crack behaviour of WAAM Ti64.

The WAAM parts cannot always be machined due to their complex geometry or cost-saving. Therefore, the evaluation of surface roughness and its effect on fatigue life is crucial. There is also a subsequent need to develop more robust prediction methods for the as-deposited surface for AM parts to optimise the design and machining requirements.

Additionally, to investigate the scatter in fatigue life observed by Biswal et al. [13], a further investigation on the effect of local microstructure and local crystallographic orientations on fatigue life of WAAM parts needs to be performed in the presence of defects.

1.2 Aim and objectives

Therefore, the aim of this research was to study the small crack growth behaviour in WAAM Ti64 and use the small crack growth rate property to predict the durability of a specimen with as-deposited surface condition. The main objectives are:

- To investigate the small crack growth behaviour, measure and represent the small crack growth rate using an empirical law
- To characterise the surface waviness of as-deposited WAAM Ti64
- To understand the effect of as-deposited surface waviness on fatigue durability through testing and modelling

- To develop fatigue models based on the notch stress and fracture mechanics approaches for predicting the durability life of as-deposited WAAM Ti64
- To identify the effect of crystallographic orientation (texture) of grains surrounding a defect on fatigue life scatter.

1.3 Thesis Structure

Following this introduction Chapter, a literature review is presented in **Chapter 2**, which consists of a state of the art and analysis of different additive manufacturing processes and types of defects encountered in these processes, the techniques used to identify them, and the effect of surface defect on fatigue life and prediction models. In **Chapter 3**, the classical theories of notch-fatigue and fracture mechanics are presented to understand the damage mechanism in materials, which are used later to develop the predictive models.

Chapter 4 presents the experimental details of small crack growth testing. To obtain materials data, small crack testing was carried out as recommended by ASTM E647 [36]. Classical Newman-Raju solution overestimated the stress intensity factor, K . Hence, FE modelling was performed to identify the small crack driving force, K and NASGRO equation was calibrated to predict the small crack growth behaviour of WAAM Ti64 and to develop a unified crack growth curve.

Chapters 5 and **6** report work related to as-deposited surface waviness. **Chapter 5** provides the experimental design and details of surface characterisation of as-deposited WAAM Ti64 using different metrology techniques, i.e., coordinate measuring machine (CMM), form tracer (FT), white light interferometer (WLI) and optical microscopy (OM). The durability study of the as-deposited WAAM Ti64 was then performed under a three-point bending load and compared with the polished samples. The fracture surface and microstructural analysis were also performed to better understand the fracture behaviour. Furthermore, crack growth from the as-deposited “groove” was also measured and presented as crack length vs. life. **Chapter 6** proposes the prediction methodologies based

on the classical notch-fatigue approach and modern fracture mechanics approach for the durability analysis of as-deposited WAAM Ti64.

Chapter 7 discuss the role of local microstructure and crystallographic orientation on the fatigue life scatter of WAAM Ti64 in the presence of as-deposited defects, especially internal porosity.

Chapter 8 summarises the research findings and draws the conclusions and the scope for future research that this research has opened.

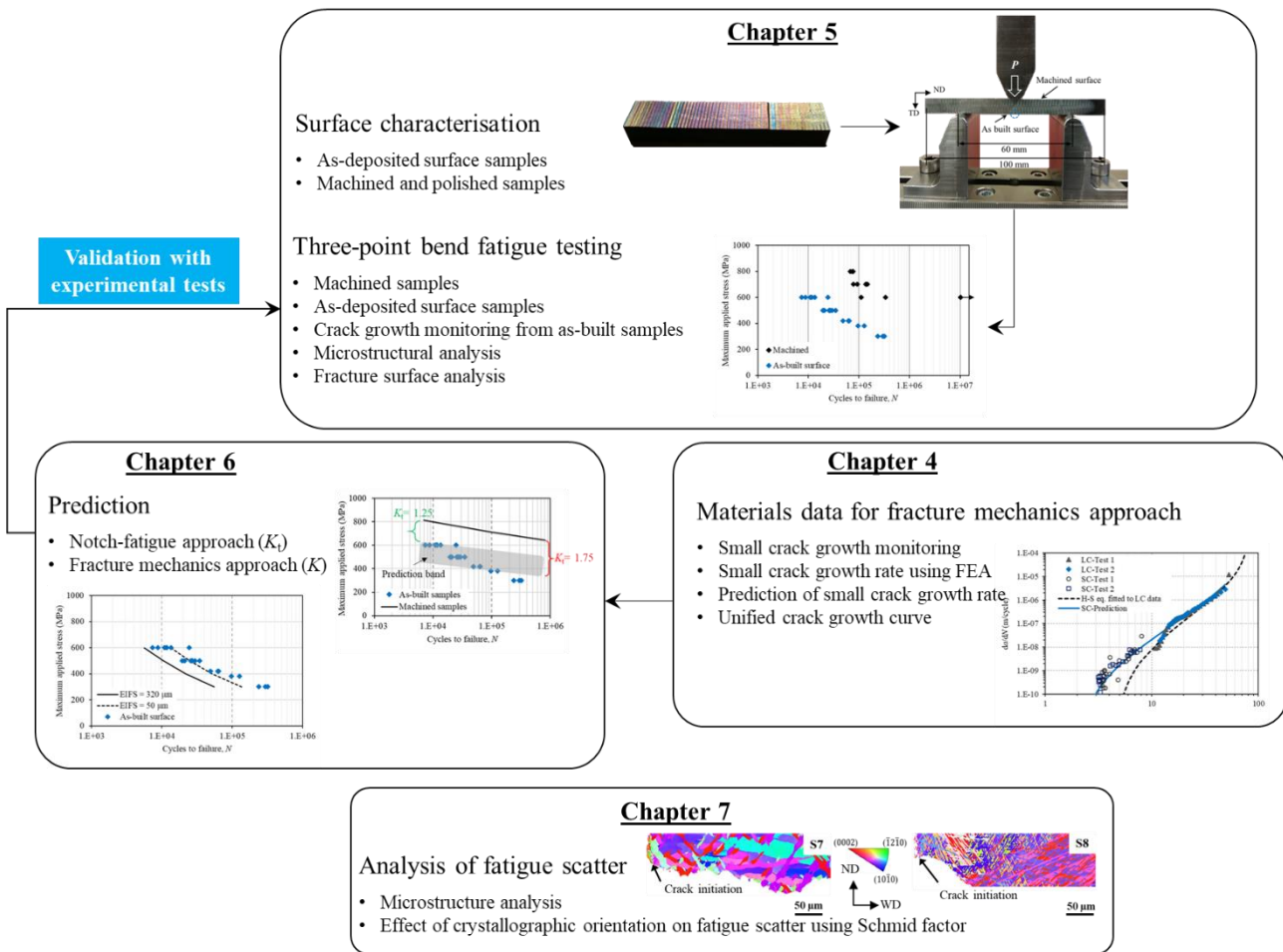


Figure 1.1: Research roadmap for durability assessment of WAAM Ti64 in as-deposited condition.

Chapter 2

Literature review: AM processes, their microstructure and defect occurrence

2.1 Introduction

The aim of this Chapter is to provide state of the art on the structural integrity of additive manufactured parts specifically for titanium alloys. Titanium (Ti) alloys have found its applications in the aerospace industry due to its high specific strength, low thermal expansion, compatibility with composites and high corrosion resistance [42]. The specific application of Ti includes fan disks in aero-engines subjected to moderate temperatures of about 500° C and booster case of GE-90 [42–44]. Ti is the fourth most abundant structural metal found in the earth's crust at a level of about 0.6%. However, the relative cost for the production of pure Ti is almost 100 times higher than steel [42]. This relative high cost of Ti metal makes additive manufacturing (AM) attractive technology as it produces parts in near net shape with minimal machining required at the end of the process, thus decreasing the buy-to-fly ratio (the mass ratio of the raw material used to produce a component compared to the mass of the component) and lead time to deliver parts [45]. The typical buy-to-fly ratio of Ti aerospace component produced from the traditional manufacturing process is 12-25:1, which reduces to 3-12:1 in the case of AM Ti [46,47]. Furthermore, AM has high flexibility of feedstock material, and in the case of powder feed processes such as selective laser melting (SLM) and electron beam melting (EBM), powders can be reused [48,49]. Therefore, the application of AM is growing rapidly in the aerospace industry and driving the research interest in this area. Finnish Air force was the first to conduct a flight test on a F/A-18 with an AM part in its engine, which was a safety-critical component and subjected to extreme loading conditions [50]. Boeing announced its first flight with 600 AM parts in 2020, and Airbus, in collaboration

with GKN aerospace on “wings for the future” project working towards the qualification of AM parts [51]. The US Navy's recent announcement for commissioning of 3D manufacturing lab at US Navy aircraft carrier John C. Stennis, which will become the first aircraft carrier having this advanced manufacturing facility, has verified this interest in using AM for manufacturing replacement parts for aerospace [52].

However, the service quality, durability and other mechanical properties of final products need to be understood to decide whether the AM process can be an acceptable manufacturing technique and could replace traditional manufacturing techniques. Therefore, the assessment of AM parts should be considered for practical application requirements and compared with the counterparts built with conventional manufacturing processes. Among different Ti alloys, Ti-6Al-4V (Ti64) is an attractive structural alloy occupying almost half of the market share of Ti products used in the world today. For Ti64, the foremost demand is in the load-bearing structures and therefore, tensile, and fatigue properties should be particularly considered.

This Chapter summarises the AM processes for Ti64 and the effect of process inherent defects on fatigue properties.

2.2 Additive manufacturing

Additive manufacturing (AM) is a relatively novel manufacturing process that has evolved from rapid prototyping. According to ASTM F2792 [53], AM is defined as the “process of joining materials to make objects from three-dimensional (3D) models data, usually layer upon layer as opposed to subtractive manufacturing technologies”. As compared to traditional manufacturing methods, the most significant advantage of AM is the freeform fabrication capability of complex geometries directly from the feedstock material [45]. The capability of AM to produce near net shape parts makes it cost-effective compared to traditional manufacturing processes due to waste minimization.

AM processes include a wide range of versatile methods depending on the feedstock material and heat source. According to ASTM F2792 [53], the AM process can be categorised as directed energy deposition (DED) and powder bed fusion (PBF). A further distinction can be made depending on the heat source, such as laser, electron beam,

plasma arc and gas-metal arc. However, this PhD is on wire + arc additive manufacturing (WAAM) process which is a type of DED process. Nevertheless, other AM processes are discussed briefly to better understand the properties and differences between them.

2.2.1 Powder bed AM processes

Selective laser melting (SLM) and electron beam melting (EBM) is a type of powder-bed AM techniques, using a laser beam or electron beam, respectively, to selectively melt the powder bed [54]. It starts with a CAD model, which is sliced into planar layers, and a scan path is then defined based on the geometry. The parts are then formed by spreading thin layers of powder and fusing them layer by layer of this powder in an inert chamber while incrementally lowering the part after each layer. The heat generated by the laser melts the powder particles fusing them together (Figure 2.1a).

However, in the case of the electron beam (EB), a vacuum chamber is used. The process consists of two steps; at first, each layer of powder is lightly sintered to avoid electrostatic charging, which can cause repulsion in powder particles, followed by an additional pass that fuses the region defined as part geometry. As the alloy powder is already slightly sintered, the overall initial temperature is higher and therefore, cooling rates are slower. Furthermore, the EB process is limited to conductive materials only.

2.2.2 Powder feed AM process

The powder feed process is a type of DED in which the part is manufactured by melting and subsequently spraying the metal powder to the surface (Figure 2.1b). The operation is carried out in an inert environment created by argon or helium to protect the molten pool from oxidation and reacting from other gases such as nitrogen in the case of Ti. The heat energy is provided by the laser, and powder is fed by the nozzle. However, compared to the powder bed system, powder feed systems are more efficient in building rates, and more build volumes are produced. Build rates up to 300 cm³/h can be achieved with a layer thickness of 0.04 mm to 1 mm. Feed rates of up to 30 grams/min have been used for Ti64 [55]. The two types of powder feed systems have been developed: (i) In which

the work piece moves and the feed head are stationary (ii) the feed head moves and the work piece is stationary [56].

2.2.3 Wire feed AM processes

In the wire feed process, the feedstock is a wire, and the energy source can be a laser beam, electron beam, electric arc or plasma arc. The wire feed processes have a higher deposition rate compared to powder bed and powder feed processes [55].

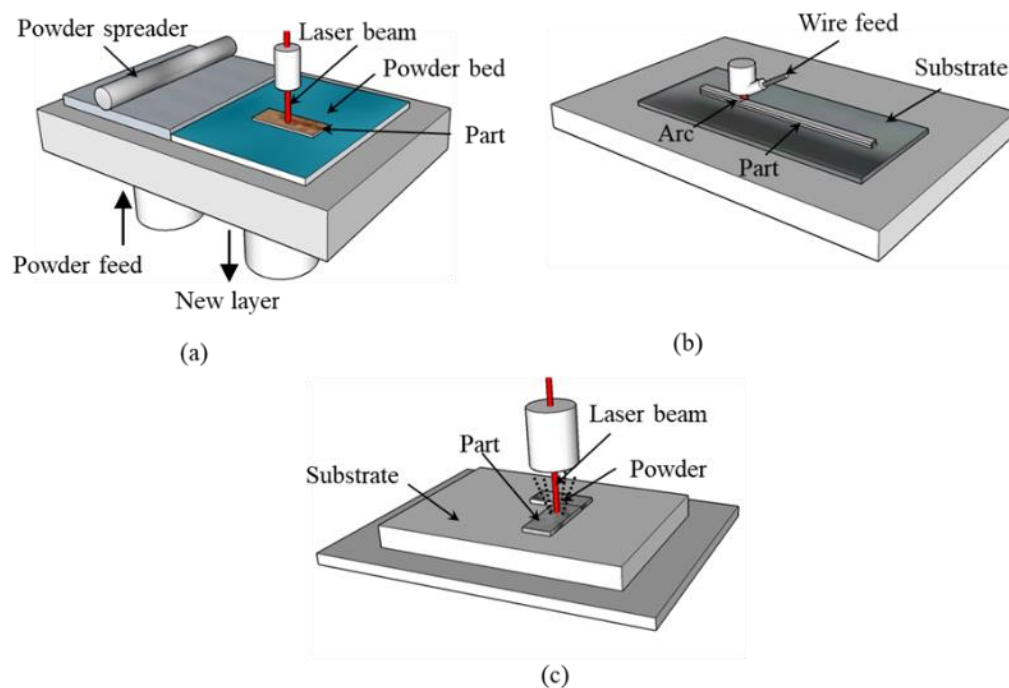


Figure 2.1: Schematic representation of (a) laser-based powder bed fusion process, (b) wire + arc-based directed energy deposition process, (c) laser-based directed energy deposition process [57].

The wire + arc additive manufacturing (WAAM) is a type of wire feed additive manufacturing process. It uses an electric arc or a plasma arc to melt the wire and deposit it on a substrate plate to form a 3D structure (Figure 2.1c). The part may be mounted on a multi-axis controlled rotator to alter the build direction while manufacturing. The typical deposition rates in WAAM Ti64 is 2 kg/h with a feeding accuracy of ± 0.2 mm compared to ± 0.04 mm in powder bed and powder feed processes [10,58]. Therefore, the surface finish of WAAM is not very good compared to powder bed and powder fed processes and

require more extensive machining [58]. Nevertheless, the large parts can be manufactured using WAAM technology due to high deposition rates with a layer height of approx. 1-2 mm [9]. The introduction of WAAM technology has reported to further reduce the buy to fly ratio to even less than 1.5 as it fully utilises the raw material [7,59].

2.3 Metallurgy of Titanium

Ti is an attractive structural material due to its high strength, good corrosion properties and low density. There are many manufacturing processes by which Ti parts are made that includes casting, forming, forging and powder metallurgy. However, Ti is very difficult to machine because of its high reactivity, low thermal conductivity and high strength at elevated temperature. Therefore, in machining Ti alloys, slow speeds are recommended with flood tooling, and maintaining sharp tools, which increases Ti alloys' machining cost. Nevertheless, with AM, the manufacturing cost of Ti parts can be significantly reduced [44].

Since AM involves melting and solidification while making a component and these alternate thermal cycles produce a nonconventional microstructure affecting the mechanical properties of AM Ti alloys. The effect of resultant microstructure on durability and damage tolerance of Ti alloys needs to be investigated and to understand this typical microstructure of Ti, the metallurgy of Ti is discussed briefly in the following paragraph.

Ti undergoes an allotropic transformation from hexagonal closed-pack (hcp) crystal structure (α phase) to body centred-cubic (bcc) crystal structure (β phase) on heating. This transformation occurs at a specific temperature depending on alloying elements present in the Ti alloy and the purity of the metal. For pure Ti, the α to β transformation temperature is 882 °C and cooling from temperatures higher than 882 °C, and the α is transformed according to the Burger relationship, i.e., $\{110\}_{\beta} // (0002)_{\alpha}$, $\langle 111 \rangle_{\beta} // \langle 11\bar{2}0 \rangle_{\alpha}$ [60]. In Ti alloys with intermediate solute contents, which are slowly cooled from single β phase to $\alpha+\beta$ phase, the β phase decomposes by the nucleation of α phase

at β grain boundaries with diffusion-controlled growth taking place into the retained β phase [60].

The resultant microstructure is α phase distributed as individual laths and colonies in a matrix of β phase. The microstructural parameters of the α phase, i.e. the width of individual α lath and α colony size, decreases with increasing cooling rates. The α lath width decreases drastically from about $5\ \mu\text{m}$ to $0.5\ \mu\text{m}$ for a cooling rate of $100^\circ\text{C}/\text{min}$, whereas a further reduction in cooling rate reduces the α lath width to almost $0.2\ \mu\text{m}$, which is an average width of the martensitic plate. Whereas the α colonies can be as large as $300\ \mu\text{m}$ in a slow cooled Ti64, which reduces to approx. $100\ \mu\text{m}$ at cooling rates of $100^\circ\text{C}/\text{min}$ to down to a width of an individual α lath at $8000^\circ\text{C}/\text{min}$ [61]. Figure 2.2 shows the effect of different cooling rates on the microstructure of Ti64.

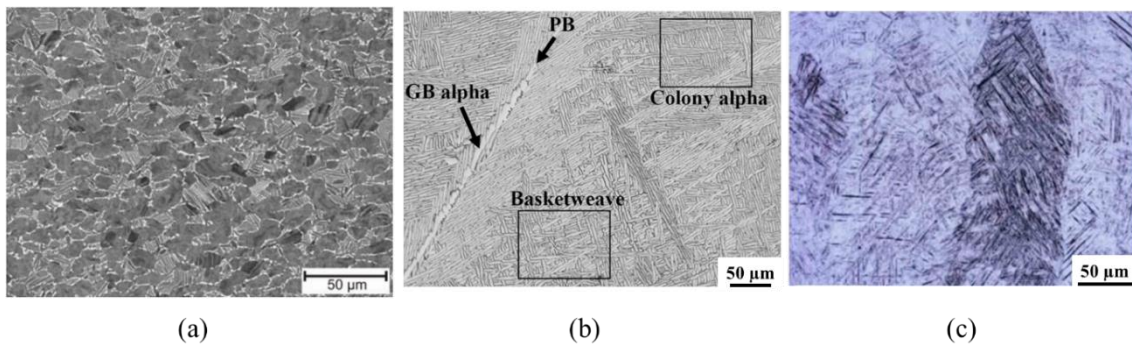


Figure 2.2: Different types of Ti64 microstructure formed as a result of different cooling rates and processing conditions; (a) forged and mill annealed Ti64 [61] (b) directed energy deposition laser metal wire deposition (cooling rate = $7 \times 10^6\ ^\circ\text{C}/\text{min}$) [45,62] (c) laser powder bed fusion (cooling rate = 10^4 - $10^6\ ^\circ\text{C}/\text{min}$) [45,63].

Furthermore, to better understand the WAAM Ti64 microstructure, the thermal cycle was studied and presented in [12]. It can be observed from Figure 2.3 that Ti64 transforms to β phase above $996\ ^\circ\text{C}$ and melts at $1646\ ^\circ\text{C}$ [64]. Solidification occurs instantly at a localised area, and the repeated heating and cooling with short and steep thermal gradients affect the resulting microstructure of WAAM Ti64. It can be further observed from Figure 2.3 that with subsequent layers being deposited, the temperature reaches above β transus and cools down rapidly, resulting in fine α laths. Nevertheless, underneath 4-5 layers, the

temperature remains below β transus and would coarsen the α laths. The prior β grains grow epitaxially in the deposition direction due to this thermal gradient, which ranges from 500 μm to 5 mm (Figure 2.2b) [65]. This type of microstructure induces anisotropy in the AM Ti64, affecting the mechanical properties depending on the orientation of the samples.

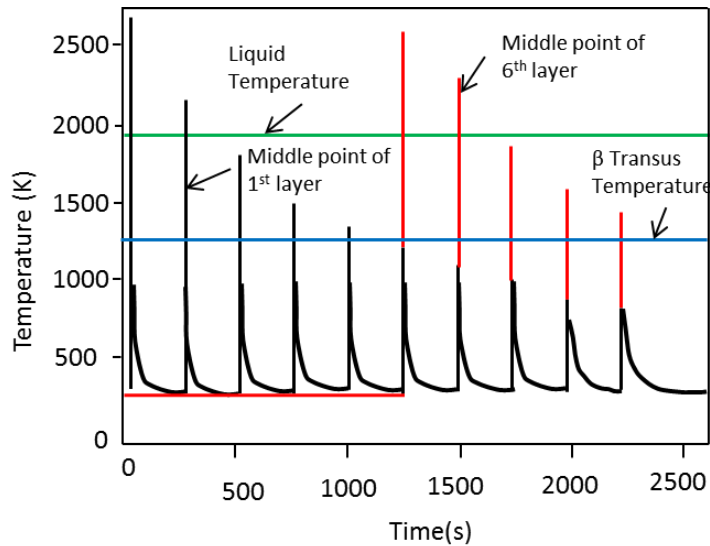


Figure 2.3: Thermal history of WAAM Ti64 calculated from FEA during deposition of the first ten layers [12].

Ti alloys deform plastically either due to the activation of slip planes or the twinning mechanism. Besides numerous other physical factors, the intrinsic anisotropic behaviour of hcp in the α phase influences the elastic and plastic properties of Ti and its alloys. The variation of Young's modulus, E of pure α phase Ti single crystal at room temperature, is given as a function of the angle γ between the c-axis of the unit cell and the stress axis (Figure 2.4a). The modulus varies between 145 GPa (stress axis parallel to c-axis) and 100 GPa (stress axis perpendicular to c-axis). Although such differences are less pronounced in polycrystalline α Ti, there can still be variations for highly textured materials [42]. This variation in modulus is associated with the activation of different slip systems at different critical resolve shear stress (CRSS) values. The active slip planes in α -Ti are $\{10\bar{1}0\}$, followed by $\{10\bar{1}1\}$ and (0002) as shown in Figure 2.4b with CRSS depending on the alloy contents and operating temperatures.

Figure 2.4: (a) Young's modulus (E) of α -Ti single crystal as a function of loading direction with respect to the c -axis (b) The unit cells of α phase (hcp) and β phase (bcc). Reproduced from [42]

Twinning is another plastic deformation mechanism where the atoms on one side of the boundary are located in a mirror-image position of the atoms of the other side (Figure 2.5) [66]. The twinning observed in α -Ti are $\{10\bar{1}2\}$, $\{11\bar{2}1\}$ and $\{11\bar{2}2\}$. Twinning modes are especially important for plastic deformation at low temperatures if the stress axis is parallel to the c -axis and dislocations with basal Burgers vector cannot move and $\{10\bar{1}2\}$ and $\{11\bar{2}1\}$ twins are activated under tension leading to extension in the c -axis. The solute atoms in α -Ti suppress the twin deformation, and hence this type of deformation is most common in pure Ti or CP Ti with lower solute concentration [42].

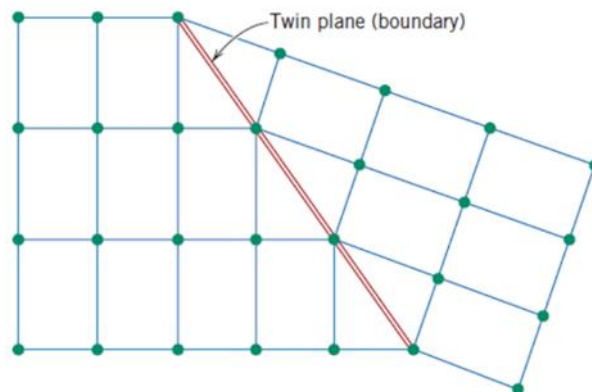


Figure 2.5: Schematic representation of the twin boundary and the adjacent atoms [66].

2.4 Defects in the AM process

The process-induced defects are formed due to wetting and de-wetting of powder particles, hydrodynamic forces and feedstock quality (powder and wire) [67,68]. The process parameters such as energy input, layer thickness, and deposition rates also influence the defects formation. In AM, two different types of internal defects are reported, i.e. gas pores and lack of fusion (LoF) defects [67,69,70]. The gas pores consist of trapped inert gases that arise from hollow powder particles or turbulence in the melt pool due to hydrodynamic forces resulting in a regular shaped defect in the case of the powder-based AM process. While in the wire-based AM process, porosity is formed primarily due to feedstock contamination (Figure 2.6) [13,71,72]. Simultaneously, the LoF defects are usually generated due to lack of energy when the molten pool is not large enough to penetrate the previously deposited layer resulting in elongated defects [73,74]. The fast scanning speeds cause inadequate penetration, which reduces the melt pool size and enhances the formation of LoF defects that ranges from 20 μm to 200 μm [57]. These voids are generally larger than the gas pores and can be distinguished by sharp edges within the build and act as stress raisers under applied loads (Figure 2.7). Furthermore, the LoF defects are irregular in shape but are less in number than gas pores [75]. The formation of internal defects can be minimised using high-quality feedstock material and optimised process parameters such as energy input, layer thickness, scanning speed, and hatch spacing (in case of the powder-bed process) or by post-process operation such as hot isostatic pressing (HIPing) [73,76].

Bauereiß et al. [77] discussed the LoF formation mechanism in powder-based processes and observed that when the particle is bonded with a molten particle instead of the molten layer which coalesce together to form a liquid droplet, this droplet is then free to move in all direction, and instead of fusing to the already deposited layer, it will move towards the free powder and depending on the surface tension, a spherical shape is formed. Due to this phenomenon, the energy is distributed, and less energy is available to melt the previously deposited layer due to the shadow effect of this powder particle. This lack of energy, accompanied by fast coalescence of the powder particles, results in lower heat input, leaving only conduction as a possibility to melt and close the cavity preventing the

closure of the cavity. Nevertheless, by increasing the beam power, these defects can be reduced. However, once the defect has been initiated, it will be robust and expand to many layers [77].

This item has been removed due to 3rd Party Copyright. The unabridged version of the thesis can be found in the Lanchester Library, Coventry University.

(a)

(b)

Figure 2.6: Porosity defect found in (a) electron beam melting [71] (b) wire + arc additive manufacturing [13].

Kasperovich et al. [78] studied the effect of energy density on defect morphology and concluded that low energy density causes the LoF defects. These LoF defects were found between the layers and were normally perpendicular to the build direction. They further observed that an increase in power density eliminated the LoF defects at the cost of porosity might be useful as porosity creates lower stress concentration factors [29]. However, higher energy density prevents the formation of LoF but may introduce the chances of another type of defect, as studied by Dilip et al. [79]. These are termed as keyhole defects where the material evaporates locally, forming a round pore entrapped in the melt pool due to high energy input. They normally appear on top of the melt pool and are not considered critical as they can escape during the remelting of the previous layer. Keyhole defects can be avoided by higher scan speeds and lower energy density.

Another concern with the AM built parts is the process inherent surface roughness. Due to the repetitive nature of the deposition process, the surface and subsurface defects and unmelted powder particles create a rough surface on the as-deposited part. A typical surface profile of SLM and EBM Ti64 can be seen in Figure 2.8. The surface roughness

of AM parts appears as a periodic profile and is dependent on the process, feedstock material (powder or wire) and geometry of the part [15,24,80]. Therefore, the surface roughness of the AM built parts can be controlled by optimizing process parameters.

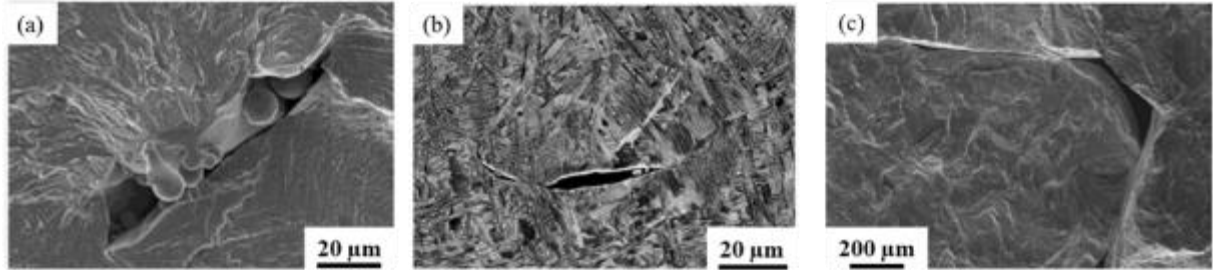


Figure 2.7: LoF defects in different AM Ti64 (a) selective laser melting (SLM) [81] (b) electron beam melting (EBM) [82] (c) laser metal wire deposition (LMwD) [67].

El-Sayed et al. [83] proposed a theoretical model to correlate laser power and surface roughness for SLM Ti64. They demonstrated that at a speed of 250 mm/s and constant hatch spacing of 78 μm, the increase in laser power from 35 to 50 W resulted in a significant improvement in surface roughness as the R_a value decreased from 21 to 9 μm. They observed that a better surface was formed when the laser power was increased, creating considerable recoil pressure, which flattened the melt pool. Moreover, the high laser power improved the wettability of the powder particles, thus significantly improving the surface finish. Gong H. et al. [84] observed that large overlapping of melt pool areas has shown to improve the surface roughness. Similarly, Gockel et al. [85] reported a decrease in surface roughness parameter R_a and R_v with an increase in laser power from 80 to 120 W for L-PBF IN 718.

Apart from the process parameters, other factors such as inclination angle of the surface, powder size and layer thickness also affect the surface condition of the AM parts [86]. Machining the as-deposited surface of an AM part is not always possible due to the complexity of the geometry. Nevertheless, the surface roughness can be improved to an acceptable degree by using various remelting strategies. Yu et al. [87] proposed the remelting strategy for AlSi10Mg and observed that remelting improved the top surface roughness from $R_a = 20.67$ to 10.87 μm and also decreased the porosity volume. An

improved surface roughness ($R_a=19.3$ to $R_a=0.93\ \mu\text{m}$) has been reported by Han and Jiao [88] for SLM AISi10Mg.

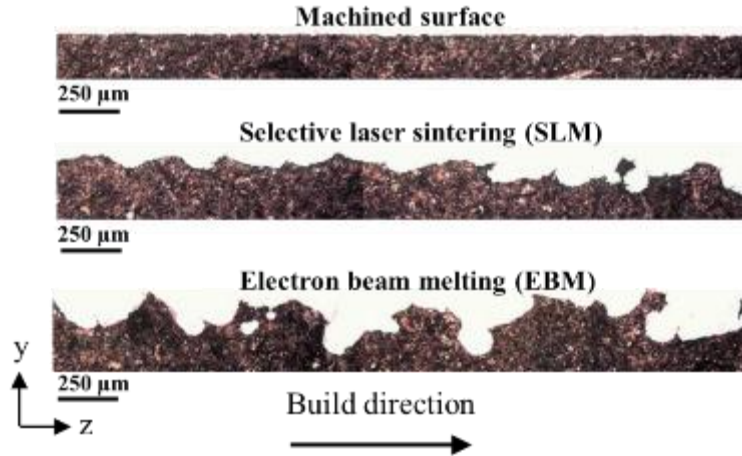


Figure 2.8: Comparison of as-deposited electron beam melting surface and selective laser melting surface with the machined surface [80].

2.5 Characterisation AM defects

Parts with large defects are more prone to fatigue failures than small defects, and therefore fatigue life is dependent on the size of defects present in the material [89]. Predicting the defect size based on the process parameters is not a practical approach due to the number of process parameters involved in the manufacturing process. Therefore, defects are characterised in terms of size, shape, type, location, frequency and density from a selected set of samples, and their correlation to mechanical properties have been studied [3,90,91].

The defects can be presented as either 2D or 3D geometries. Murakami [89] suggested that the defect can be represented as an effective area in 2D, and many authors have adopted this approach. However, for 3D representation of defects, their shape, sphericity (the sphericity of a shape is the ratio of the surface area of a sphere with a same volume as the given particle to the surface area of the particle [92]) and aspect ratio should be determined. Biswal et al. [72] and Seifi et al. [93] analysed the distribution of porosity in WAAM and EBM Ti64, respectively, using micro-CT and found porosity defects with an aspect ratio close to 1 (Figure 2.9a). Ziolkowski et al. [94] and Sanaei et al. [95] further

characterised the defects based on their sphericity and found that most of the defects were irregular in shape with the sphericity less than one and was dependent on the size of the defect (Figure 2.9b). On the other hand, Kabir et al. [96] used the discretisation method to represent pores with complex geometries by overlapping the pores with different sizes of spheres and examined the pore geometry [96].

The surface roughness of AM parts caused as a result of the AM process can be characterised using traditional surface roughness equipment. Among other techniques, the stylus profilometer is the most common equipment used for the surface roughness characterisation of AM parts [4,5,18,97,98]. However, stylus tip diameter should be carefully chosen for better resolution of the surface profile and accessibility to the surface.

The surface roughness of AM parts can be expressed by R_a , R_v , R_y , R_z (arithmetic mean surface roughness, maximum valley depth, maximum depth, and an average of five deepest valleys) [80,98]. The values can be correlated to the fatigue life of the as-deposited surface of AM parts and can be further used to predict the fatigue life of AM parts.

Although R_a has been widely reported in the literature, it may not be a suitable parameter to analyse the fatigue performance of as-deposited AM parts. In terms of powder-based processes, the partially melted particles on the surface affect the surface roughness value. However, as partially melted particles, they do not bear the load and hence do not contribute to the stress concentration associated with the rough surface. Nevertheless, R_v may be more relevant in correlating fatigue life with a surface roughness of as-deposited AM parts.

Due to the appearance of the surface of AM parts, it is sometimes impossible to capture all the details using the contact method. Hence, different techniques such as areal topography measurement, white light interferometry, and 2D imaging using optical and scanning electron microscopy are employed to understand the as-deposited AM surface better.

This item has been removed due to 3rd Party Copyright. The unabridged version of the thesis can be found in the Lanchester Library, Coventry University.

Figure 2.9: (a) micro-CT examination of porosity defects in WAAM Ti64 where porosity was induced intentionally [72] (b) aspect ratio vs. sphericity visualisation characterised by μ -CT for Ti64 [95].

2.6 Mechanical properties of AM parts

2.6.1 Tensile and hardness

The ultimate tensile strength of AM Ti64 is higher as compared to conventional manufactured Ti64. However, a range of properties has been reported in the literature. The yield strength (YS) and ultimate tensile strength (UTS) reported in wire feed, and powder feed AM Ti64 ranges from 522-1105 MPa and 797-1163 MPa, respectively [13,99–101]. The YS and UTS for the powder bed process are between 736-1330 MPa and 947-1400 MPa, respectively [102,103]. However, in the cast and annealed Ti64, the YS is 896 and 855 MPa, while UTS is 1000 and 930 MPa, respectively [42].

This item has been removed due to 3rd Party Copyright. The unabridged version of the thesis can be found in the Lanchester Library, Coventry University.

Figure 2.10: Effect of porosity on tensile properties of WAAM Ti64 [13].

The ductility of AM Ti64 is generally lower as compared to conventionally manufactured Ti64. Nevertheless, an elongation range of 1-19% has been reported in the literature as compared to 8-12% in conventionally made Ti64 [42,99–103]. This wide range of elongation in AM Ti64 is largely dependent on the presence of defects such as porosity, lack of fusion and surface roughness which acts as stress raisers and reduces the ductility [29]. Another factor in the wide range of elongation in AM Ti64 is the anisotropy induced by the resultant microstructure.

Biswal et al. [13] investigated the YS and UTS of WAAM Ti64 and compared it with samples having porosity defects (Figure 2.10). The WAAM samples without defect are marked as reference samples, and it can be seen that difference in monotonic strength is less than 5% between the two types of samples, while the elongation is significantly lower in “Porosity specimens” and is a result of the formation of microcracks in the vicinity of pores.

The hardness varies in AM Ti64 even in the same process. The Vickers hardness reported in the case of AM Ti64 is between 341-372 Hv. This high hardness in AM Ti64 is due to fine α laths, which impedes the dislocation movement.

2.6.2 Fatigue properties

The fatigue performance of AM parts is affected by the presence of defects discussed in Section 2.5. These defects act as either crack initiation sites or small cracks. The assumption of these defects (initial cracks, crack initiation sites) defines which model can be used to compute the fatigue life of AM parts. Most of the studies showed that surface roughness is the most detrimental on fatigue performance of as-deposited AM parts, and machining of the as-deposited surface seems to have improved fatigue performance. However, machining cannot be performed on all the parts depending on design consideration, time, and cost constraints [5,27]. Therefore, the effect of the as-deposited surface on the fatigue performance of AM parts has been the topic of discussion in the literature.

The repeated cyclic loading of the material causes irreversible displacement of slip bands resulting in the roughening of the material's surface. This roughening is manifested as 'intrusions' and 'extrusions' at the sites where slip bands emerge on the free surface and create stress concentration sites. These stress concentration sites promote additional slips and cause crack nucleation. Therefore, surface roughness and surface defects are more detrimental to fatigue life compared to internal defects as most of the cracks initiate from the surface [17,18,24,31,104]. However, various AM materials have a range of surface roughness values depending on the process type and parameters manifesting different fatigue behaviour.

Greitemeier et al. [5] studied the high cycle fatigue performance of SLM and EBM Ti64 having surface roughness values of $R_a = 13 \mu\text{m}$ and $R_a = 27$ in SLM and EBM, respectively (Figure 2.11). The higher surface roughness in the case of EBM resulted in a much reduced fatigue life as compared to SLM. The same observation was made by Chan et al. [20]. While HIPing significantly reduces the size and population of internal defects, but no improvement was reported on the surface roughness of AM parts [105,106]. Nevertheless, a significant improvement in fatigue life was observed in the machined samples (Figure 2.11). The improvement was more significant in SLM than EBM due to the lesser number of internal defects in the SLM process [27]. Edward and Ramulu et al.

[27] has also reported the dominating effect of surface roughness on fatigue life of AM parts. However, they observed that in the absence of surface roughness, internal defects governed the fatigue life. The detrimental effect of surface roughness in SLM Ti64 samples has also been reported [4,107] in various loading conditions.

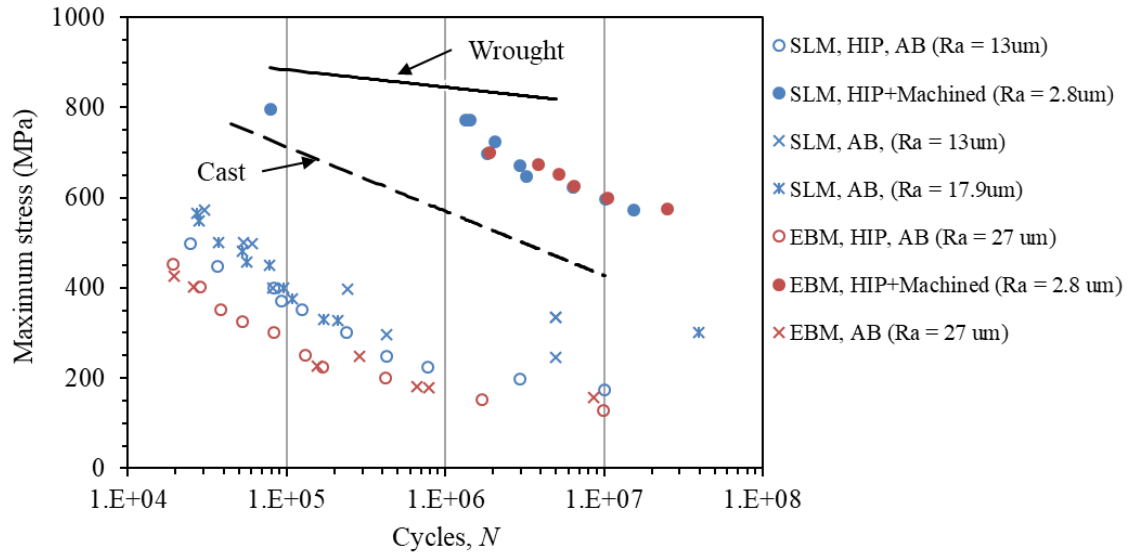


Figure 2.11: Effect of surface roughness and HIPing on fatigue performance of Ti64. All tests were conducted at $R = 0.1$. [5,27,108,109].

Fatigue life as a function of square root R_a is shown in Figure 2.12 for SLM Ti64, derived from the concept of Murakami's square root area. It can be seen that at a given stress amplitude, the fatigue life of as-deposited AM Ti64 decreased as the surface roughness increased [24]. It was further observed that in the presence of surface roughness, fatigue life was more affected by the presence of a small internal defect and relatively larger microstructure as compared to larger internal defects and fine lamellar microstructure [14].

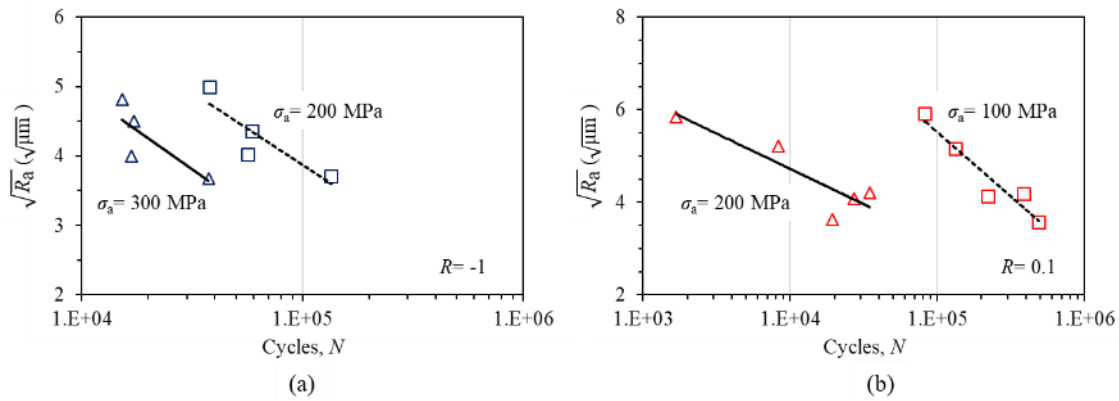


Figure 2.12: Correlation between fatigue life at two different stress levels and square root of R_a (a) $R = -1$ data, (b) $R = 0.1$ data [24].

2.7 Fatigue life prediction models

Conventional fatigue notch stress models proposed by Nueber have been used in the literature to analyse the effect of small defects such as porosity and surface roughness [29,30,110]. Nevertheless, linear elastic fracture mechanics (LEFM) has also been adopted for the surface roughness effect on fatigue by considering the defect as an initial crack [31,73,98]. For AM parts, sub-millimetre size defects are the source of fatigue crack initiation or initial fatigue damage [111]. However, the current LEFM models hold limitations in the physically small crack domain [32].

Hoorewedew et al. [112] studied the effect of artificial notches on fatigue behaviour of AM parts and later applied it to the naturally occurring AM defects. By employing the theory of critical distance (TCD), they calculated the fatigue limit of the SLM Ti64 notched component. Benedetti et al. [113] also investigated the application of TCD on SLM Ti64 notched component containing defects and concluded that fatigue strength is dependent on the size of the defect. They observed that fatigue notch factor K_f decreased as the critical size of the defect increased, which was more pronounced in the sharp notches.

Pegues et al. [114] considered the surface roughness as a notch and calculated the K_t at a depth of the valleys acting as a notch, and reported a reasonable agreement with the

fatigue strength. Vayssette et al. [115] proposed a multistage model to predict the fatigue life of SLM Ti64 and concluded that a profilometer might not well describe micro notches in the case of SLM Ti64.

Gunther et al. [73] studied the fracture mechanics approach for L-PBF Ti64 using Murakami's [89] \sqrt{area} parameter defined as the square root of the projected area and classified the defects based on their location from the surface. They concluded that the most critical defects are the ones closer to or on the surface. Masanori et al. [116] and Yamashita et al. [117] also followed this methodology for powder-based AM Ti64 and IN 718 alloy. However, for specimens failing due to LoF defects, the error of estimation was largely due to the irregular shape of the LoF defects. Romano et al. [118] observed that fatigue life was governed by the defects which had the highest stress intensity factor and were located at the surface or subsurface. The size of the most critical defects causing failure was identified using fracture surface analysis and through polished cross-sections using optical microscopy. To predict the fatigue life, an estimation of the semi-circular defect was used, and the stress intensity factor was calculated using eq. (2.1) [89]

$$\Delta K = C \times \Delta \sigma \sqrt{\pi \sqrt{area}} \quad (2.1)$$

where ΔK is the stress intensity factor range, parameter C is 0.65 for surface defects or 0.5 for embedded defects, $\Delta \sigma$ the applied stress range, and \sqrt{area} the square root of the projected area of the defect. A variant of the NASGRO equation was further used to calculate the fatigue life. Apart from it, various modifications of NASGRO equations have also been adopted in the literature to predict the fatigue life of AM parts with defects [32,41,119,120].

Wycisk et al. [98] proposed the use of AFGROW to predict the crack growth life of L-PBF Ti64 employing LEFM while considering defects as initial cracks. It is a damage tolerance approach to predict the fatigue life by analysing crack initiation, crack growth

and final fracture. They observed that the fatigue life was dominated by fatigue crack initiation and was greatly influenced by the resultant microstructure.

A FASTRAN code to predict the fatigue life of AM parts with the surface defect was used by Yadollahi et al. [17] by considering the initial size and aspect ratio of the defects. Initial cracks were modelled as semi-circular and semi-elliptical surface flaws with varying aspect ratios. They proposed using maximum valley depth, R_v gives a better estimate of initial damage of surface flaw. Furthermore, it was assumed that the samples were defect-free and contained only surface roughness. Therefore, the interaction of surface and internal defects was ignored. Their prediction results appear to be in good agreement with the experimental results.

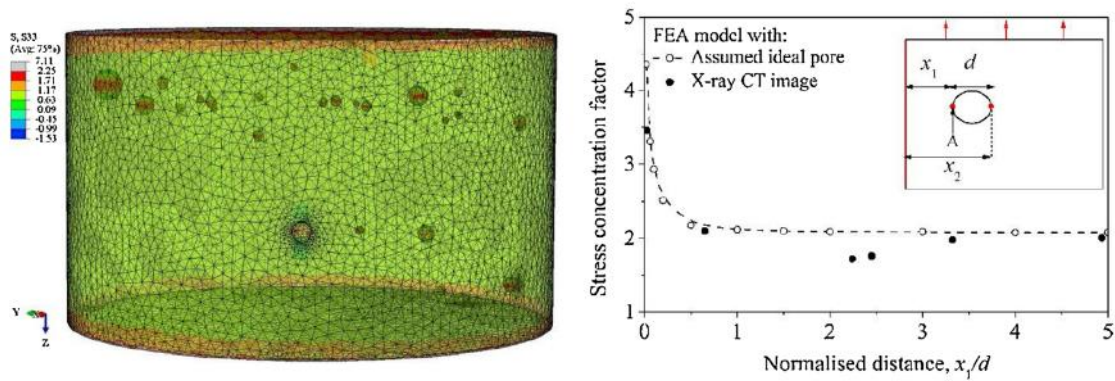


Figure 2.13: FE model using X-ray computed tomography (CT) scanned geometry, meshing using image-based FE algorithm (b) variation of stress concentration factor at the root of the pore A with distance x_1 from the free surface compared with idealised pore geometry.

Zhang et al. [18] also suggested R_v as the initial damage and used LEFM to predict the effect of surface roughness on fatigue life. Their prediction for L-PBF Ti64 under different loading conditions showed good agreement with the experimental data and was within the ± 3 scatter band. Ramano et al. [121] proposed elastic-plastic fracture mechanics (EPFM) by adopting J -integral and studied different AM materials.

Apart from the semi-empirical models, fatigue life prediction of AM parts has been conducted using multistage models. For example, Biswal et al. [72] investigated the porosity in wire arc additive manufactured Ti64 using CT, which were used to model

defects using Image-based FEA (Figure 2.13). The local stress and strains were calculated using cyclic plasticity and used Basquin equation to predict the fatigue life. The fatigue life predictions were improved by CT informed Image-based models by providing exact shape size and location of the defects.

2.8 Summary

The additive manufacturing process offers design freedom through layer by layer deposition and material saving which ultimately reduces the cost of the final product. Nevertheless, the layer by layer deposition of molten material introduces complex thermal history resulting in unconventional microstructure and texture, introducing anisotropic behaviour of AM parts. Therefore, the effect of this microstructure on fatigue properties needs to be further explored, especially in the presence of defects.

The layer by layer deposition of molten material introduces a wavy appearance which introduces the surface roughness on the finished part, and machining such parts is not always possible. The as-deposited surface affects the fatigue performance of AM parts; thus, identification and characterisation of surface roughness is crucial for AM parts to be used in as-deposited condition. The literature shows considerable fatigue life reduction for as-deposited AM parts. However, there is no such study available for as-deposited WAAM Ti64.

There are different surface representation models available in the literature which may work well in the case of SLM and EBM, but due to the wavy nature of the WAAM surface, other roughness parameters needs to be explored. Therefore, there is a subsequent need to develop robust models to characterise the surface roughness of as-deposited WAAM parts using actual roughness data rather than creating idealised geometry.

Different approaches have been used in the literature to predict the fatigue life, i.e., notch-fatigue approach and fracture mechanics approach. Both approaches seem to be working well depending on the process and resultant defect type. Nevertheless, both of these approaches require proper characterisation of defect type, size and location.

Hence, this study aims to understand the role of as-deposited surfaces and unconventional microstructure of the wire + arc additive manufactured Ti64 towards fatigue crack initiation and small crack propagation behaviour. The AM components cannot always be machined due to the complex geometry and to save the cost of post-processing. Therefore, identifying and correlating the correct surface roughness parameter with fatigue life is essential for structural integrity analysis. This study has not been performed in the literature. Thus, a systematic experimental and modelling strategy has been developed and detailed in the following Chapters.

Chapter 3

Theoretical framework and methodologies

3.1 Introduction

Fatigue is a multistage phenomenon where the failure mechanism depends on the crack initiating feature. Fatigue damage broadly starts with microstructural changes (formation of persistent slip bands), leading to microscopic cracks. These microscopic cracks coalesced together to form a lead crack which would eventually cause catastrophic failure. The different stages of fatigue are shown in Figure 3.1. However, in the presence of notches and defects, stress concentration location will act as a crack initiating site, and the crack will grow under cyclic loads until the component's failure. Fatigue analysis can be done using either the traditional notch-stress approach or fracture mechanics approach (Figure 3.1). This Chapter discusses the framework of both approaches. It concludes with the derived assumptions and models applicable to the present problem, i.e., durability analysis of AM parts with internal defects and surface features.

This item has been removed due to 3rd Party Copyright. The unabridged version of the thesis can be found in the Lanchester Library, Coventry University.

Figure 3.1: Different phases of fatigue life and relevant factors reproduced from [122].

3.2 Notch fatigue method

3.2.1 Material property (S-N, ϵ -N)

The fatigue life is obtained by experimenting on smooth test specimens guided by the ASTM standard and presented in the form of stress-life (S - N) or strain-life (ϵ - N), respectively [123,124]. The resultant life is the number of cycles to initiate a crack and cycles required to propagate the dominant crack until catastrophic failure. The number of cycles required to initiate a crack of engineering size (typically on the order of mm) may vary from 0% in specimens containing severe stress concentrations, induced by surface or subsurface defects to as high as 80% in carefully prepared laboratory coupons, which are theoretically defect-free with a high level of surface finish [125]. Many engineering alloys do not exhibit a fatigue limit. However, when presented in terms of a log-log scale with stress amplitude plotted as a function of the number of cycles, the stress amplitude decreases with the increasing number of cycles and a linear relationship is obtained. This linear relationship i.e., applicable to HCF under elastic conditions can be presented as the Basquin equation, eq. (3.1)

$$\frac{\Delta\sigma}{2} = \sigma'_a = \sigma'_f (2N_f)^b \quad (3.1)$$

where $\Delta\sigma$ is the applied stress range, σ'_f and b referred to as co-efficient and fatigue strength exponent respectively and are obtained from the intercept and slope of $\Delta\sigma/2$ vs. N plot of a logarithmic scale, respectively.

Some engineering components may go under plastic deformation in many practical applications, especially at and around stress concentration sites. In such a situation, it is more suitable to adopt the strain-life approach. The strain-life relationship of any alloy can be given by and Coffin-manson equation, eq. (3.2) [125]

$$\frac{\Delta\varepsilon_p}{2} = \varepsilon_f'(2N_f)^c \quad (3.2)$$

where $\Delta\varepsilon_p$ is the applied plastic strain range, ε_f' and c fatigue ductility constant and fatigue ductility exponent respectively obtained from $\frac{\Delta\varepsilon_p}{2}$ vs. N_f plot of a logarithmic scale.

This item has been removed due to 3rd Party Copyright. The unabridged version of the thesis can be found in the Lanchester Library, Coventry University.

Figure 3.2: The total strain amplitude vs. life obtained from the elastic and plastic strain amplitude superposition, reproduced from [125].

Furthermore, the total strain amplitude from the strain-controlled test can be written in the form of elastic strain amplitudes and plastic strain amplitudes given in eq. (3.3) and can be expanded to eq. (3.4).

$$\frac{\Delta\varepsilon}{2} = \frac{\Delta\varepsilon_e}{2} + \frac{\Delta\varepsilon_p}{2} \quad (3.3)$$

$$\frac{\Delta\varepsilon}{2} = \sigma_f'(2N_f)^b + \varepsilon_f'(2N_f)^c \quad (3.4)$$

The left and right terms in eq. (3.4) corresponds to the elastic and plastic terms of the total strain amplitude, respectively. The transition life (N_t) can then be calculated by drawing the tangents, as shown in Figure 3.2. At the N_t , the elastic and plastic amplitudes are equal. It can be further identified that at shorter lives, i.e., the number of cycles to failure, $N_f \ll N_t$, then the plastic strains will be dominant, and the fatigue life will be dictated by ductility, and if $N_f \gg N_t$, the elastic strains will be dominated.

3.2.2 Cyclic stress-strain relation

The deformation of engineering alloys subjected to uniaxial cyclic loads is characterised by the cyclic stress-strain curve. The cyclic hardening or softening of the material is manifested in the constant amplitude loading by increasing or decreasing the axial strain amplitudes. Generally, the engineering alloys are categorised as soft or hard alloys depending on the difference between its yield strength σ_{ys} and ultimate tensile strength σ_{uts} (hard alloys have $\sigma_{uts}/\sigma_{ys} > 1.4$ while soft alloys have $\sigma_{uts}/\sigma_{ys} < 1.2$) subject to the activity of the dislocation motion [126]. Suppose the arrangement of dislocations because of cyclic loading offers more resistance to deformation, cyclic hardening will be observed. However, if the arrangement of dislocations offers less resistance, cyclic softening will be observed.

The material's cyclic behaviour is obtained from a displacement controlled fully reversed cyclic load test. The hysteresis loops stabilise typically after 50 to 100 cycles, and the stress vs. strain response is then used to record material data, with the area under the hysteresis loop represents the accumulation of plastic strain energy in each cycle. The stabilised cyclic stress-strain curve of the material can be obtained by joining the tips of the loop and is given by eq. (3.5), known as the Ramberg-Osgood equation [125].

$$\frac{\Delta \varepsilon}{2} = \frac{\Delta \sigma}{2E} + \left(\frac{\Delta \sigma}{2K'} \right)^{1/n} \quad (3.5)$$

where $\Delta\varepsilon$ is the strain range, $\Delta\sigma$ stress range, E Young's modulus, K' cyclic strength coefficient and n' cyclic strain hardening exponent.

3.2.3 Stress raisers in part and life prediction

Engineering components may contain stress concentration sites in the form of surface scratches, dents, machining marks, fillets, and corrosion pits. To evaluate the severity of stress raisers, the most common term used is the stress concentration factor (K_t). It is defined as the ratio of maximum stress at the notch root to the applied stress. The maximum stress is calculated under the assumption of the linear elastic condition. The fatigue strength at N cycles in a notched component would be expected to decrease by a factor of K_t . The K_t is a geometric parameter and does not depend on the material property. For simple geometries such as open-hole in an infinitely wide plate, the K_t can be calculated using eq. (3.6) [127]

$$K_t = 1 + 2 \left(\frac{b}{a} \right) \quad (3.6)$$

where K_t is the stress concentration factor shown in Figure 3.3a, W width of the plate, which is significantly larger than a .

In the case of a spherical cavity in an infinite solid, the mathematical expression of K_t is derived as follows, eq. (3.7) [128]

$$K_t = \frac{27 - 15\nu}{14 - 10\nu} \quad (3.7)$$

where K_t is the stress concentration factor, ν the Poisson's ratio of the material.

The commonly used experimental techniques to measure K_t are photoelasticity and strain gauges. In photoelasticity, a transparent replica is loaded to study the changes in the optical properties of the material using a polariscope. While in the case of strain gauges, local strains are measured at the root of the notch by fixing strain gauges. The strains are proportional to the stress under the linear elastic condition and frequently used in the industry due to their ease in application.

Once the value of K_t is known, Neuber's approach can then be used to calculate the stress and strain amplitudes at the notch root using eq. (3.8).

$$\Delta\sigma\Delta\varepsilon = \frac{(K_t\Delta S)^2}{E} \quad (3.8)$$

where $\Delta\sigma$ is the local stress range $\Delta\varepsilon$ the local strain range and E Young's modulus of the material.

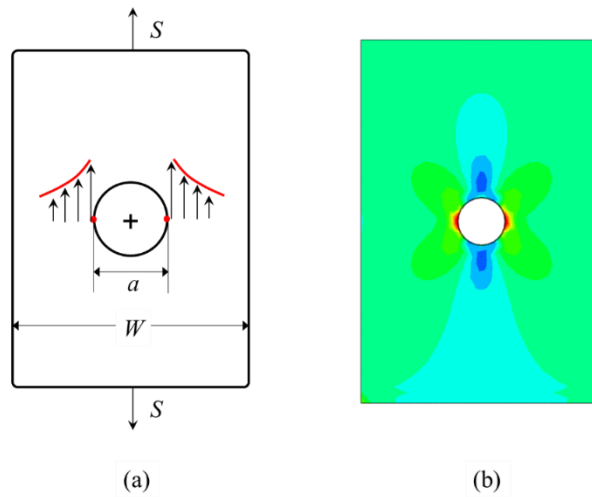


Figure 3.3: (a) Schematic of stress distribution around an open hole [127], (b) FE model showing stress distribution around the open hole in a wide plate.

Nevertheless, for fatigue life prediction, use of fatigue notch strength reduction factor (K_f) is preferred over K_t to avoid highly conservative estimation. K_f is the ratio of fatigue strength of smooth specimens to that of notched specimen and K_t and K_f are related by the notch sensitivity factor, q and given as eq. (3.9).

$$q = \frac{K_f - 1}{K_t - 1} \quad (3.9)$$

From [129] the value of q for Ti64 ELI can be determined to be 0.6. Hence, K_f is lower than K_t to account for the plasticity and notch sensitivity effects. Therefore, eq. (3.8) can be modified to eq. (3.10). Materials $S-N$ or $\epsilon-N$ data is then used to predict the crack initiation life of the component with stress raisers.

$$\Delta\sigma\Delta\epsilon = \frac{(K_f\Delta S)^2}{E} \quad (3.10)$$

Much of the fatigue life discussed in the above section is based on constant amplitude loading, but these results are not realistic in actual service conditions. Many structures are subjected to different loads and amplitudes. Predicting the fatigue life of a component subjected to variable loading history based on constant amplitude loading can be done using Miner's rule [126]. If the same amount of damage is done on a component at any stress level. The fraction of lifetime consumed will be n_1/N_1 , where n_1 is the number of cycles at σ_1 and $n_1 < N_1$. To determine how many additional cycles the component can survive at another stress level, σ_2 , an additional life will be available. The sum of the two fractions will be equal to one.

For solving the remaining cycles allowed at σ_2 , the generalised approach of Miner's law can be written as eq. (3.11):

$$\sum_{i=1}^k n_i/N_i = 1 \quad (3.11)$$

where k is the number of stress levels in a block loading diagram, n_i the number of cycles applied at σ_i and N_i the fatigue life at σ_i .

Nevertheless, Miner's law should be viewed as a reasonable approximation to be used in structural designs. However, damage accumulation in fatigue is usually a complicated mixture of several different mechanisms, and the linear damage accumulation inherent of Miner's law may not capture it.

3.3 Fracture mechanics based approach

Damage tolerant design takes up an approach to fatigue design, assuming that the component already has a flaw. This flaw is determined using different non-destructive techniques such as visual, dye penetration, X-ray, ultrasonic or acoustic emission methods. The smallest initial flaw size detectable using this NDT technique depends on the resolution of the technique available for inspection and prediction of fatigue life based on defect-tolerant approach is based on empirical crack growth laws of fracture mechanics.

Among various fracture mechanics approaches like Griffith fracture theory, energy release rate and linear elastic fracture mechanics (LEFM), the LEFM offers more precise terms of critical conditions for the growth of cracks developed to calculate or predict fatigue crack growth rate and life with loading condition [125]. The LEFM is a widely used technique to calculate the stress field ahead of the crack tip in terms of nominal applied stress and flaw length when the plastic zone ahead of the crack tip is considerably smaller than the crack length. The LEFM approach can be illustrated by the typical example of an internal sharp through-thickness crack with a crack length of $2a$ in a thin

plate, Figure 3.4a. In mode I, the local stresses at the polar coordinates (r, θ) close to the crack tip are given by eq. (3.12)-(3.14) [130]

$$\sigma_{xx} = \frac{K}{\sqrt{2\pi r}} \left[\cos \frac{\theta}{2} \left(1 - \sin \frac{\theta}{2} \sin \frac{3\theta}{2} \right) \right] \quad (3.12)$$

$$\sigma_{yy} = \frac{K}{\sqrt{2\pi r}} \left[\cos \frac{\theta}{2} \left(1 + \sin \frac{\theta}{2} \sin \frac{3\theta}{2} \right) \right] \quad (3.13)$$

$$\sigma_{xy} = \frac{K}{\sqrt{2\pi r}} \left[\sin \frac{\theta}{2} \cos \frac{\theta}{2} \cos \frac{3\theta}{2} \right] \quad (3.14)$$

where K is the stress intensity factor used in fracture mechanics to predict stress state (stress intensity) near the tip of the crack caused by remote load or residual stresses. It is defined in terms of applied stress σ and half crack length a as shown in eq. (3.15):

$$K = \sigma \sqrt{\pi a} f\left(\frac{a}{w}\right) \quad (3.15)$$

where $f(a/w)$ is a geometry factor. The stress intensity factor, K , is the most useful parameter near the crack tip and driving force for the crack propagation as it is function σ and crack size a and can be calculated considering specimen dimension and loading condition.

The fatigue life is determined by the number of fatigue cycles or time required to grow the dominant crack to a critical dimension. The crack growth rate can be correlated to the fracture mechanics parameter such as K . The fatigue crack growth rate is then calculated using Paris law [131]. Unlike the classical approach for fatigue design, where the part is

designed for crack initiation, this approach is based on the part's residual life and hence more cost-effective than the previous approach. The concept of K has been adopted in fatigue theory to characterise crack growth behaviour instead of using σ . By plotting fatigue crack growth rate (da/dN) against ΔK in the *log-log* coordinates, a sigmoidal curve is obtained and divided into three distinct regions, as shown in Figure 3.4b. *Region I* is characterised by a low ΔK and prolonged crack growth rate, and thereby a threshold stress intensity range ΔK_{th} is defined as the smallest driving force to attain a detectable crack growth rate. *Region II* is the stable crack growth and describes by the Paris equation, eq. (3.16), where da/dN is the crack growth rate, ΔK is the stress intensity factor range, C and m are material constants derived from the intercept and slope from da/dN vs. ΔK plot in a logarithmic scale from *Region II* (shown in Figure 3.4b). In *Region III*, the crack growth rate accelerates rapidly towards the final fast fracture. However, as mentioned in the above equations, eq. (3.12)-(3.14), the stress reaches infinity if r approaches zero, which is not practical as the yielding occurs ahead of the crack, making LEFM invalid in describing very near crack tip stress/strain behaviour.

$$\frac{da}{dN} = C(\Delta K)^m \quad (3.16)$$

eq. (3.16) is then numerically integrated to give the number of cycles to reach a critical crack length and can be rewritten as eq. (3.17)

$$N_f = \sum_{a_i}^{a_f} \frac{\Delta a}{f(\Delta K)} \quad (3.17)$$

3.3.1 Small crack growth rate

As shown in Figure 3.1, the fatigue life can be divided into several phases. The crack nucleation is related to the local stress and strain concentrations and notch constraints. While the slip mechanism may be necessary for pure metals, the presence of inclusions, defects, and surface appearance greatly affects the crack nucleation process. Small crack growth is the term referred to as cracks growing from these defects and surface appearances. Schijve et al. [122] have shown that the growth of small cracks, typically to a size of 100 μm in size, consumes about 60-70% of the total fatigue life. Thus, there is a lot of interest in the growth of small cracks and using them in the design criteria. Thus, Figure 3.1 is modified to Figure 3.5 by Newman et al. [132].

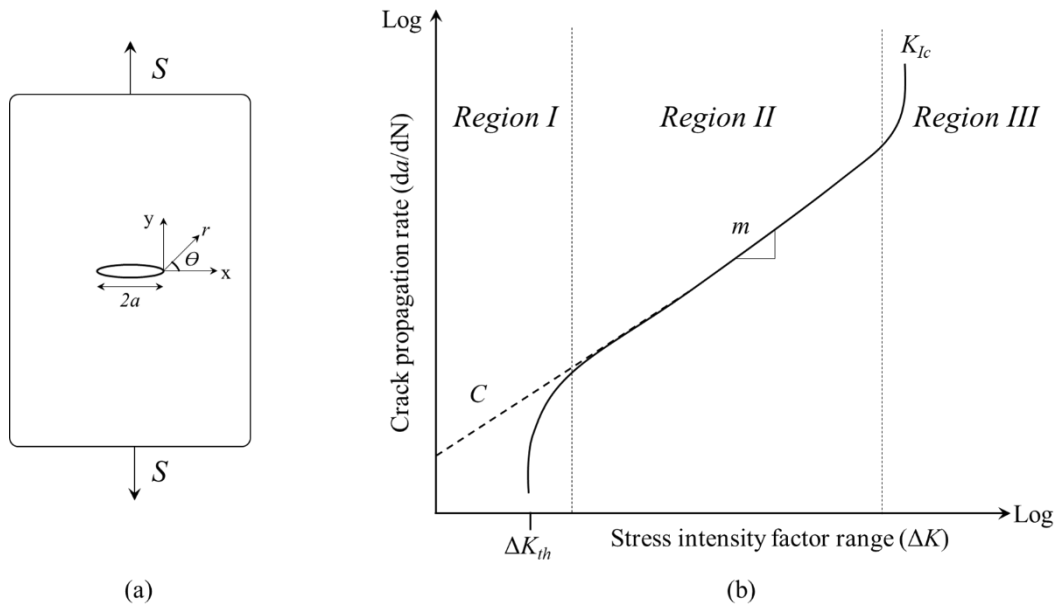


Figure 3.4: (a) crack in a plate, (b) schematic representation of the da/dN vs. ΔK in a double-logarithmic plot with the Paris law represented as a straight line.

There are different size scales below which the growth rates of fatigue cracks may exhibit size dependence. According to [133], the small cracks can be broadly classified as following four criteria:

- 1) Microstructurally small flaws: where the size of the crack is comparable to the microstructural dimension, such as grain size and interparticle spacing in the particulate reinforced composites
- 2) Mechanically small flaws: small cracks in which the near tip plasticity is comparable to the crack size.
- 3) Physically small cracks: These cracks are significantly larger than the microstructural characteristics and the scale of local plasticity but are merely physical small to the order of a millimetre
- 4) Chemically small cracks: Fatigue cracks that follow the LEFM but exhibit apparent anomalies in propagation rates below certain crack sizes due to the dependence of environmental stress corrosion fatigue effects on crack dimensions.

Furthermore, ASTM E647-15 defines the small into four categories, i.e. (i) mechanically small where the crack size, $a \leq$ plastic zone size (r_y) (ii) microstructurally small crack where $a \leq 5$ -10 times of characteristics microstructural dimension, often grain size (d_g) (iii) physically small cracks when the $a \leq 1$ mm and (iv) chemically small crack for a is up to 10 mm.

This item has been removed due to 3rd Party Copyright. The unabridged version of the thesis can be found in the Lanchester Library, Coventry University.

Figure 3.5: Different phases of fatigue life and relevant factors modified by [132].

This item has been removed due to 3rd Party Copyright. The unabridged version of the thesis can be found in the Lanchester Library, Coventry University.

Figure 3.6: Kitagawa-Takahashi diagram for transition crack length [134,135].

In stage I of the crack growth of small cracks and flaws, the apparent retardation and arrest behaviour point to the existence of threshold conditions that may be very different from the long cracks. The similitude concept of LEFM implies that intrinsic threshold stress intensity range ΔK_{th} for a long crack should be crack size independent of the crack size $\Delta K_{th} = \Delta K_0$. The short crack growth data obtained from a variety of ductile material by Kitagawa & Takahashi demonstrated a critical crack size, d below which ΔK_{th} decreases with decreasing crack length (Figure 3.6). For $a < d$, the threshold condition is characterised by a critical stress $\Delta\sigma_{th}$, which approaches to σ_e for a smooth sample with vanishingly small cracks. For $a > d$, $\Delta K_{th} = \Delta K_0$ and ΔK_{th} are independent of the crack size.

$$d = \frac{1}{\pi} \left(\frac{\Delta K_0}{\sigma_e} \right)^2 \quad (3.18)$$

$$\Delta K_{th} = \Delta K_0 \text{ for } a > a_0$$

$$\Delta\sigma_{th} = \sigma_e \text{ for } a < a_0$$

Attempts have been made to establish a link between the d and the d_g in various conventionally manufactured materials [134,136,137]. The d ranges between 1-100 μm

for very high strength steel ($\sigma_y = 2000$ MPa) to 100-1000 μm for low strength steels ($\sigma_y = 200$ MPa). Although there is no unique definition of d , which is representative of all materials. The measure of d can be extracted from continuum level measurements involving σ_e and the long crack fatigue threshold.

For aerospace applications where damage tolerance is an important design consideration, there is a need to assess this new AM technology. AM produces microstructure and texture, which are different from conventionally manufactured components and affect the mechanical properties. For example, the high cooling rates associated with AM produces fine α lamellar microstructure. However, in conventional manufactured Ti64, for instance in forged Ti64, slower cooling rates during heat treatment produces coarser α with single variant α colonies. Moreover, the microstructure inhomogeneity and crystallographic anisotropy in AM Ti64 affect the crack growth behaviour [34,35,138,139]. The long crack growth rate of AM Ti64 has been investigated by [35,138,140,141]. Zhai et al. [35] studied the long crack growth behaviour of LENS and EBM Ti64 at $R=0.1$. The data is summarised in Figure 3.7. For LENS and EBM specimens, the effect of different build directions was studied and compared. The samples where crack grew parallel to the scan direction were called horizontal samples, and where crack grew parallel to build direction were called vertical samples.

Furthermore, the effect of heat treatment was also compared with the as-built condition. It was observed that LENS Ti64 in both horizontal and vertical directions showed lower ΔK_{th} values due to the presence of the martensitic α' phase. Moreover, crack growth rates were slower in the vertical direction because the interference of deposited layers and grain boundaries caused more roughness induced closure effects. However, after annealing, a slight increase in the ΔK_{th} can be observed due to the transformation of α' to α phase. In the case of as-built EBM, ΔK_{th} is higher than LENS Ti64 due to the difference in the microstructure. Martensitic α' does not exist in EBM Ti64 due to lower cooling rates and powder bed heating than LENS Ti64, which leads to higher ductility and better damage tolerance. The microstructure of LENS and EBM Ti64 contains fine α lamellar and columnar β grains.

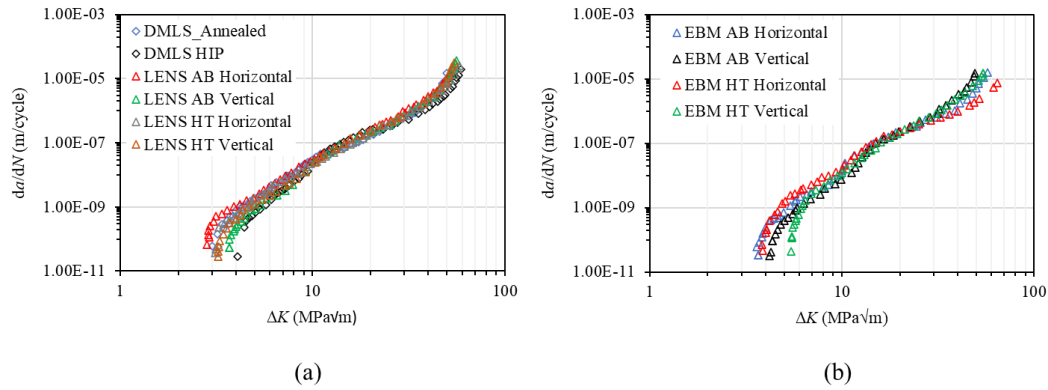


Figure 3.7: Comparison of long crack growth data of AM Ti64 tested at $R=0.1$ [34,35,119,139].

In single pass deposited WAAM Ti64, samples tested at $R=0.1$ with crack growing parallel and vertical to deposited layer showed similar crack growth rates [140]. However, Xie et al. [142] reported 5% lower crack growth rates for cracks growing parallel to deposited layers in single pass WAAM Ti64. According to [142], the epitaxial growth of prior β grain boundaries act as crack retardants and slows down the crack. However, a comprehensive study by Syed et al. [141] compared the crack growth rates of three different deposition strategies, i.e., single pass, parallel pass and oscillation. The crack growth rates were monitored in vertical and parallel orientation (crack growth was monitored parallel and vertical to deposition direction) observed different crack growth rates. It was further reported by [141] that the oscillation built samples had the lowest crack growth rates due to the wider layers of α colonies resulting in a more tortuous crack path. Nevertheless, the finer α laths in parallel and single pass deposition showed less crack deflection and higher crack growth rates. Furthermore, the crack growth rate anisotropy was observed in all three depositions with slower crack growth rates perpendicular to the build layers. A similar observation was made by Zhai et al. [35] in the case of LENS Ti64, where crack growth rates were slower in vertical direction because of the interference of deposited layers and grain boundaries causing more roughness induced closure effects.

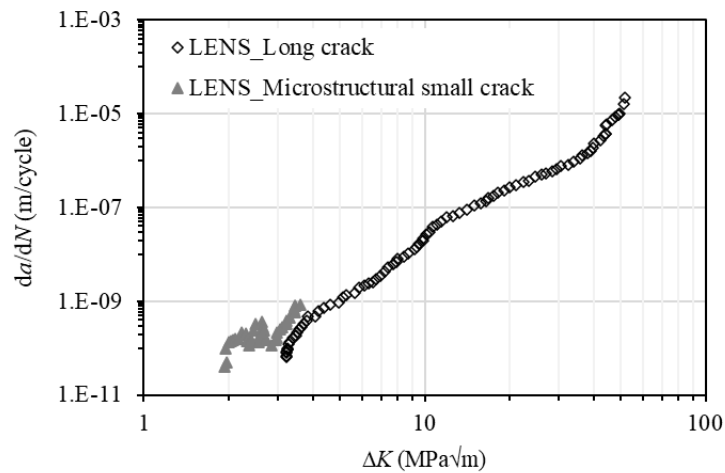


Figure 3.8: Comparison of microstructurally small and long crack growth data of LENS Ti64 tested at $R=0.1$ [139]

One of the main concerns for using AM parts for safety-critical components is the presence of defects. While these defects have little or no effect on the static strength, they cause a significant reduction in the ductility and fatigue properties [13,143]. Recent research has also demonstrated that the fracture mechanics approach can be used for predicting the durability of AM parts due to initial damage of small size [41,119,120,144,145]. In the latter approach, the equivalent initial damage size (EIDS) concept was used as the initial crack length, and the material's crack growth rate property was used to calculate the fatigue life of the component. Defects, surface roughness features and EIDS values are all in the sub-millimetre range. It has been shown that using long crack growth rate data can overestimate the fatigue life as the cracks initiating from defects or surface roughness are in the small crack domain, which grows faster than long cracks under the same value of applied stress intensity factor [33–35]. Furthermore, fatigue cracks of relevance to many structural applications are often small or short, and a significant portion of fatigue life is spent in growing small cracks [36]. Therefore, when adopting the fracture mechanics approach for durability analysis, there is a need for small crack growth rate data. For this reason, there has been an increasing interest to study the small crack growth behaviour of AM Ti64, and long crack and small crack growth behaviour has been presented in the literature [34,35,37,119,138,139,146–148]. Few studies have been performed on direct comparison of small and long crack growth

behaviour of AM Ti64 [35][139]. Sandgren et al. [139] compared the small crack growth behaviour with a long crack of LENS fabricated Ti64 and presented in Figure 3.8. Small crack growth rates are typically accelerated and retarded due to local interaction with the microstructure at a mesoscale at an early stage of crack growth. The specific interaction of small cracks with the β grain boundaries was observed at the location of crack retardation and termed as the blocking effect of grain boundaries. It was due to the difference in crystallographic orientation between the grains and the absence of atoms, and the presence of strains. It was worth observing that this blocking effect increased with decreasing grain size. Hence, fine grains had increased the resistance of small crack growth. As small crack has significantly lower ΔK_{th} as compared to long crack of the same material, it indicates the importance of considering the small crack growth data for structural application.

The behaviour of the small crack of a material can be predicted using long crack growth data as da/dN vs. ΔK relationship associated with the small cracks follows the long crack data by removing closure and other crack shielding effects [41,145]. Improved functions have been proposed in the literature to overcome these limitations.

The Forman law in eq. (3.19) [149] accounts for the effect of R ratio, and because of the term $[(1-R)K_C - \Delta K]$, crack growth goes to infinity when applied maximum SIF, ΔK approaching fracture toughness, K_C .

$$\frac{da}{dN} = \frac{C(\Delta K)^m}{[(1-R)K_C - \Delta K]} \quad (3.19)$$

The ΔK_{th} asymptote was later included in the Forman equation by Hartman-Schijve [150] by changing the numerator to $(\Delta K - \Delta K_{th})$, eq. (3.20). A similar equation was later proposed by Priddle [151].

$$\frac{da}{dN} = \frac{C(\Delta K - \Delta K_{th})^m}{[(1-R)K_c - \Delta K]} \quad (3.20)$$

Jones et al. [38] modified the original Hartman-Schijve equation (eq. (3.20)) to the form of eq. (3.22). They later referred to it as a variant of the NASGRO equation (Original NASGRO eq. (3.21)) [38,41,111,152] because the constant q in the original NASGRO equation was set as $p/2$ in eq. (3.22).

$$\frac{da}{dN} = C \left[\left(\frac{1-f}{1-R} \right) \Delta K \right]^n \frac{\left(1 - \frac{\Delta K_{th}}{\Delta K} \right)^p}{\left(1 - \frac{\Delta K_{max}}{K_{crit}} \right)^q} \quad (3.21)$$

$$\frac{da}{dN} = D \left(\frac{\Delta K - \Delta K_{thr}}{\sqrt{1 - K_{max}/A}} \right)^p \quad (3.22)$$

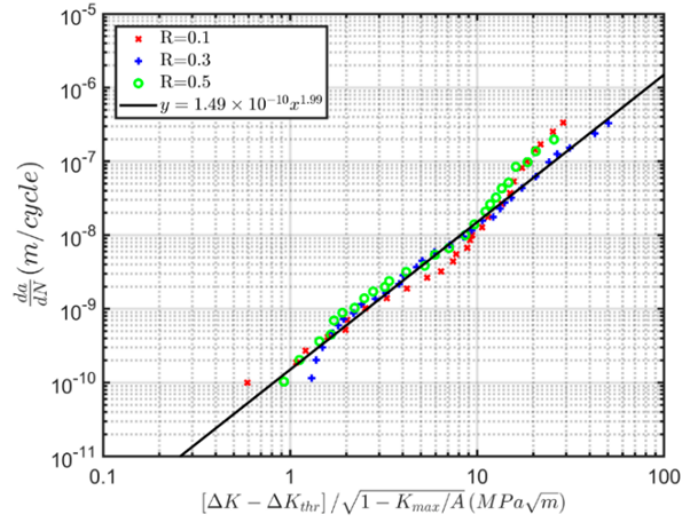
In Jones' papers, eq. (3.22) is written in a simpler form as eq. (3.23), where the $\Delta \kappa$ parameter was proposed by Schwalbe [153], eq. (24),

$$\frac{da}{dN} = D(\Delta \kappa)^p \quad (3.23)$$

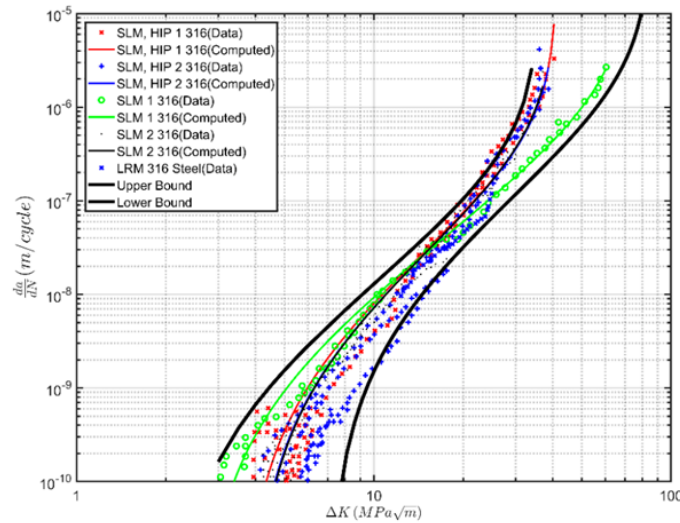
$$\Delta \kappa = \frac{(\Delta K - \Delta K_{thr})}{\sqrt{1 - K_{max}/A}} \quad (3.24)$$

where D and p are material constants, A the cyclic fracture toughness, and ΔK_{th} the fatigue crack growth threshold that is dependent on microstructure and the R ratio. For small

cracks, ΔK_{th} is termed as ΔK_{thr} in Jones' papers [41,111,154]. They proposed that the small crack growth behaviour can be represented from the long crack test data by setting the ΔK_{thr} to a very small value of around 0.1-0.3 $MPa\sqrt{m}$ [41,154].



(a)



(b)

Figure 3.9: (a) Plot of da/dN vs. $\Delta\kappa$ for determining material constants D and p of Ti64 by the fitting curve, (b) da/dN vs. ΔK experimental data and prediction [41].

To compute the small crack growth, D and p are obtained from the long crack growth data (Figure 3.9a). For a given R ratio, da/dN is plotted against $(\Delta K - \Delta K_{th}) / \sqrt{1 - K_{max}/A}$

in excel using *log-log* scales, as shown in Figure 3.9a. The value of A is initially chosen to be a typical value of Ti64. In the near-threshold region, the effect of any errors in the assumed A value in terms of K_{\max}/A in the denominator will be small.

The value of ΔK_{th} is then chosen such that the plot of da/dN vs. $(\Delta K - \Delta K_{th}) / \sqrt{1 - K_{\max}/A}$ appears to be a straight line. The value of A is then fine-tuned to improve the linearity of the plot in the high ΔK region. This process is repeated if the R ratio changes while keeping the A value constant. This process will generally result in da/dN vs. $(\Delta K - \Delta K_{th}) / \sqrt{1 - K_{\max}/A}$ plots that differ slightly in the high ΔK region. At this stage, the values of ΔK_{th} , for the given R ratio and the value of A is obtained. The values of D and p are then obtained from the linear fit to the data. These D , p , A and ΔK_{th} will then be used in the Hartman-Schijve equation to predict the small and long crack behaviour (Figure 3.9b). This method will be further discussed in the upcoming Chapter 4 to predict the small crack data using long crack data of WAAM Ti64.

3.4 Residual stress

Additive manufacturing processes are prone to a significant amount of induced residual stresses because of their large temperature gradients [155–158]. A typical temperature gradient in the case of beam-based additive manufactured Ti64 is approx. 5×10^4 K/cm. The magnitude of residual stresses increase with increased layer numbers, and the peak value occurs near the free surface of the product [157,159,160]. The residual stress profile comprises a large amount of tensile and compressive stresses with tensile stresses at the top region of the part. However, these tensile stresses convert to compressive stresses with new layers due to the alternate thermal cycles [160]. It was observed that the stresses are higher along the weld/scan direction due to larger thermal gradients and increase with scan length [155].

The inherent residual stresses affect the crack growth behaviour. Syed et al. [63] observed high values of residual stresses in an SLM vertical built Ti64 with 600 MPa tensile

residual stress near the top free surface of the component and -400 MPa compressive stresses in the middle of the part. Building flat samples decreased the residual stresses to almost negligible values. The residual stresses increased the crack growth rate in SLM Ti64, and it was recommended to perform stress relieving operations if “tall” parts are being built. Zhang et al. [161] studied the effect of residual stresses on fatigue crack growth of WAAM Ti64. They studied the crack propagation behaviour containing the interface between the wrought substrate and WAAM Ti64. The main difference between the crack propagation behaviour between the wrought interface and WAAM was attributed to the difference in microstructure with tortuous crack path associated with lamellar microstructure. Although considerable residual stresses were observed in WAAM Ti64, the retained residual stresses affected the crack propagation behaviour and depended on the direction of crack propagation. The presence of residual stresses increased the stress intensity factor, and consequently, greater crack propagation rates were observed.

3.5 Summary

The first step towards identifying a stress raiser's effect is quantifying the elastic stress concentration factor associated with the defect. Depending on the stress raiser's geometric complexity in the case of the as-deposited surface of AM Ti64 parts, which arise due to non-symmetric geometry and non-ideal boundary condition, finite element analysis is the most suitable technique. The as-deposited surface can be treated as a notch and a crack with an equivalent initial flaw size. Depending upon the failure mechanism, both notch-fatigue and linear elastic fracture mechanics can be applied to predict the fatigue life of as-deposited WAAM Ti64.

Small crack propagation is also discussed as it has become a considerable research area and can be applied to aerospace parts' design strategies. Subsequently, the Hartman-Schijve variant of the NASGRO equation was discussed and how it can predict small crack growth behaviour from long crack growth data. Micro-cracks and small cracks have been reported to grow faster than long cracks when subjected to cyclic loading at the same applied stress intensity factor range. The small crack grows even below the threshold

stress intensity range of long cracks. Hence, predicting fatigue life using the threshold of long cracks will overestimate life, which could be detrimental to aerospace parts' fatigue design.

The notch stress concept discussed in Chapter 3 has been used in Chapter 5 for surface analysis of as-deposited WAAM Ti64 surface and validation of prediction model proposed in Chapter 6. The small crack growth testing was performed and presented in Chapter 4, and the unified law discussed in Chapter 3 has been employed to predict the small crack growth rate for WAAM Ti64, which was further used in Chapter 6 for fatigue life prediction based on equivalent initial flaw size concept and linear elastic fracture mechanics. The outline of the workflow and Chapters is presented in Figure 3.8.

Chapter 4

The behaviour of small fatigue cracks in WAAM Ti64

4.1 Introduction

The mechanical behaviour and fitness-for-service of WAAM built materials for structural application require a thorough understanding of their performance under service loading conditions. The thermal history of WAAM parts results in anisotropic mechanical behaviour which is different from their wrought counterparts [162]. Hence, the durability of WAAM parts is usually influenced by resultant microstructure and the presence of defects produced during the manufacturing process [12,29,72]. The initial phase of fatigue damage, which consists of the formation of slip bands and microcracks [125], is bypassed due to the presence of these defects, which are in a sub-millimetre domain, and thus considered as small cracks. The fatigue properties of WAAM parts are also dependent on the surface roughness, which are typical features because of layer-by-layer deposition. Such surface roughness and internal defects decrease the fatigue properties of AM parts [163]. This surface appearance of as-built parts acts as stress concentration sites discussed later in Chapter 5 and can be treated as initial damage or equivalent initial flaw size (EIFS) [31]. Therefore, when adopting the fracture mechanics approach for durability analysis in the presence of these defects, there is a need for small crack growth data. Owing to the absence of a standardised approach for small crack growth test and the time and cost constraints in testing small cracks, designers for aerospace structures often do not test small crack propagation behaviour [37]. Hence, for durability analysis of conventional and AM materials, empirical models representing the small crack growth behaviour by testing only the long crack specimens have been proposed [32,38–40]. Nevertheless, these models need validation for WAAM Ti64. Therefore, this Chapter focuses on experimental methodology to characterise and compare the small and long

crack growth behaviour. It further explores how small crack growth data can be correlated to the long crack data of the same material.

The small crack samples were designed as guided by ASTM E647-15 [36]. FE modelling was performed to calculate the crack driving force, K and used to predict the crack growth life. The FE model was first verified with the benchmark solution by Newman-Raju [164]. Later in the Chapter, the Hartman-Schijve variant of the NASGRO equation is discussed and how it can predict small crack growth by using long crack data. Predicted small crack growth life was validated by the small crack test data. The verified predictive model was used to predict the fatigue life of another configuration: a beam specimen built by AM process and tested under three-point bending fatigue load and covered in Chapter 5 and Chapter 6.

4.2 Experimental procedures

The wire + arc additive manufactured (WAAM) Ti64 wall was deposited on a 12 mm thick forged Ti64 substrate using a grade-5 Ti64 wire of 1.2 mm diameter and plasma arc as an energy source. Argon gas of 99.99% purity was used as a shielding envelope (placed ahead of the torch and at the trailing end of the torch), directed precisely at the melt pool to avoid oxidation. A single bead deposition strategy was used to build a wall of 300 mm \times 150 mm \times 9 mm (thickness). The schematic of the wall is shown in Figure 1a.

For the long crack growth testing, two compact tension (C(T)) samples were extracted with a crack starter notch parallel to the weld direction. The geometry and dimension of the C(T) specimen are shown in Figure 4.1b. The test was performed according to the ASTM E647 standard [36] at a constant amplitude sinusoidal load form with a maximum applied load of 3 kN, cyclic load ratio of 0.1 and a loading frequency of 10 Hz. The crack length was measured using a travelling microscope with a 7 \times objective lens, having an accuracy of \pm 0.01 mm. After the test, the seven-point polynomial procedure recommended in ASTM E647 standard [36] was used to calculate the fatigue crack growth rate from the measured raw data of crack length versus load cycles [162].

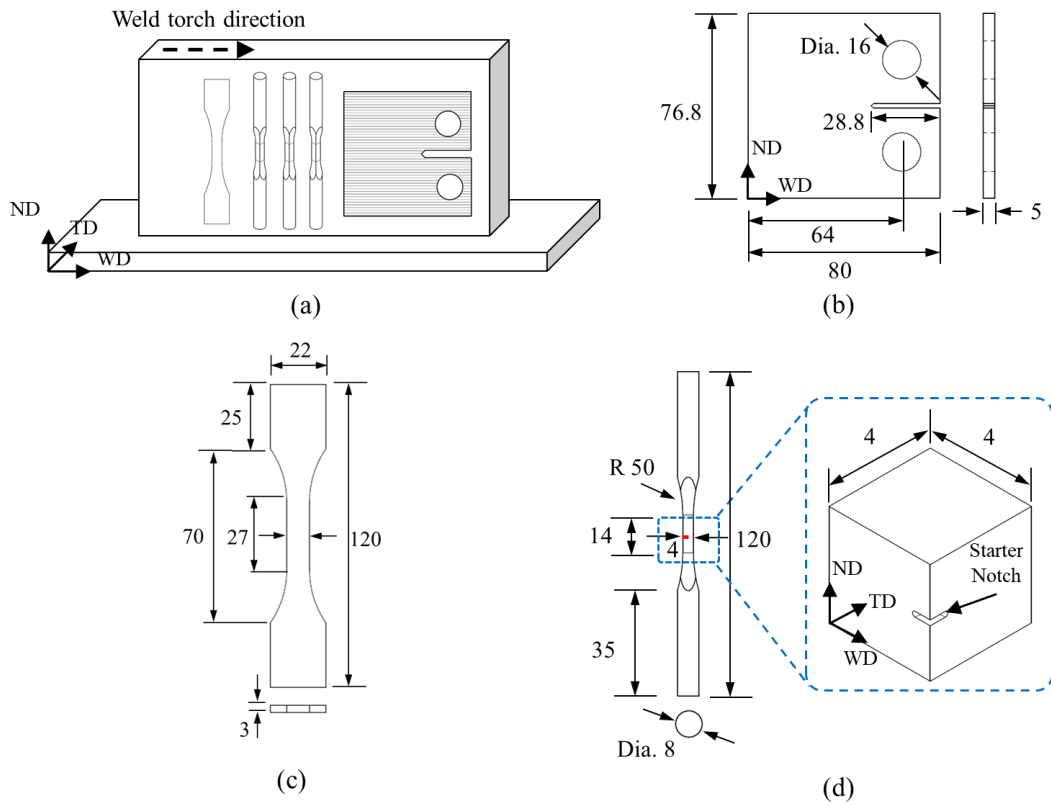


Figure 4.1: (a) Schematic of the WAAM Ti64 wall showing welding torch movement direction and sample extraction plan, (b) compact tension specimen for a long crack test, (c) geometry and dimensions of tensile sample (d) small crack sample and starter notch. [WD: welding torch movement direction, TD: transverse (thickness) direction, ND: normal direction. Unit: mm, not to scale.]

Tensile samples in the vertical direction as shown in Figure 4.1c. The tensile testing was carried out at room temperature with a displacement rate of 1mm/min using a 100 kN servo-hydraulic machine. The samples were design according to ASTM E8 standard [165]. Small crack samples were also extracted (Figure 1a, 1d) for measuring the crack growth rate in the sub-millimetre crack length range. The sample was designed according to ASTM E647 recommendations in Appendix X3 [36]. The following procedure was used to prepare the small crack samples for fatigue testing. First, the gauge section was polished using SiC paper up to 4000 grit size. A notch was then made using Electrical Discharge Machining (EDM) with a width and notch root diameter of 100 μm at the corner of the ND-WD and ND-TD planes (Figure 1d). The notch size was between 0.4 to 0.7 mm. The gauge section was subsequently polished to a mirror finish, followed by etching using Kroll's reagent to reveal the microstructure.

Fatigue test on the small crack samples was conducted under applied load range of 2 and 3.2 kN, respectively, for the two samples, at a cyclic load ratio 0.1 and test frequency of 20 Hz. The fatigue test was paused at regular intervals to measure the crack length in both crack fronts on the TD-ND and WD-ND planes using a replication method [166]. A cellulose acetate tape was used for replication method, where acetone was applied on the tape surface before placing the tape on the sample surface. An optical microscope was employed to measure the crack length from the replicas and observe the crack trajectory. For each sample, 40-50 replica measurements were taken. The reported crack length includes the initial notch size, and the final crack length recorded was in the range of 2-2.5 mm with an estimated precision of $\pm 5 \mu\text{m}$. After the fatigue test, the lead crack was identified from the replica at different cycle intervals, and the crack path was backtracked at specific cycle intervals. The secant method was then used to deduce the fatigue crack growth rate from the measured raw data of crack length vs. load cycles. Fracture surfaces were examined using scanning electron microscopy (SEM) to identify the crack propagation pattern and fracture mechanisms [162].

For microstructure analysis, scanning electron microscopy (SEM) was used. Primary β and the α lath width measurements were carried out on images taken from the centre of the cross-section samples extracted from WD-ND plane.

4.3 Results and discussion

4.3.1 Microstructural analysis

The macrostructural features of single-pass WAAM Ti64 are presented in Figure 4.2a. The layer-by-layer deposition process and local thermal history in the WAAM process resulted in white layer bands spaced equally along the build direction. These bands correspond to heat affected zones (HAZ) [167]. A detailed investigation of HAZ bands by [168] found that HAZ bands in WAAM Ti64 are caused by reheating the previously deposited layer where the temperature reaches just below the β transus temperature during the subsequent layer deposition, and such continuous thermal cycles resulted in both coarsening of the lamellar transformation structure within the HAZ bands and the

formation of a thin layer with a finer α lamellar single variant colony microstructure just below the β transus temperature [169]. Similar HAZ bands have also been reported in other wire feed [64], powder feed [169] and powder bed [170] AM processes. However, compared to the powder bed process, the HAZ bands are more pronounced in the wire and powder feed processes due to the higher heat input and higher deposition rates and greater layer height.

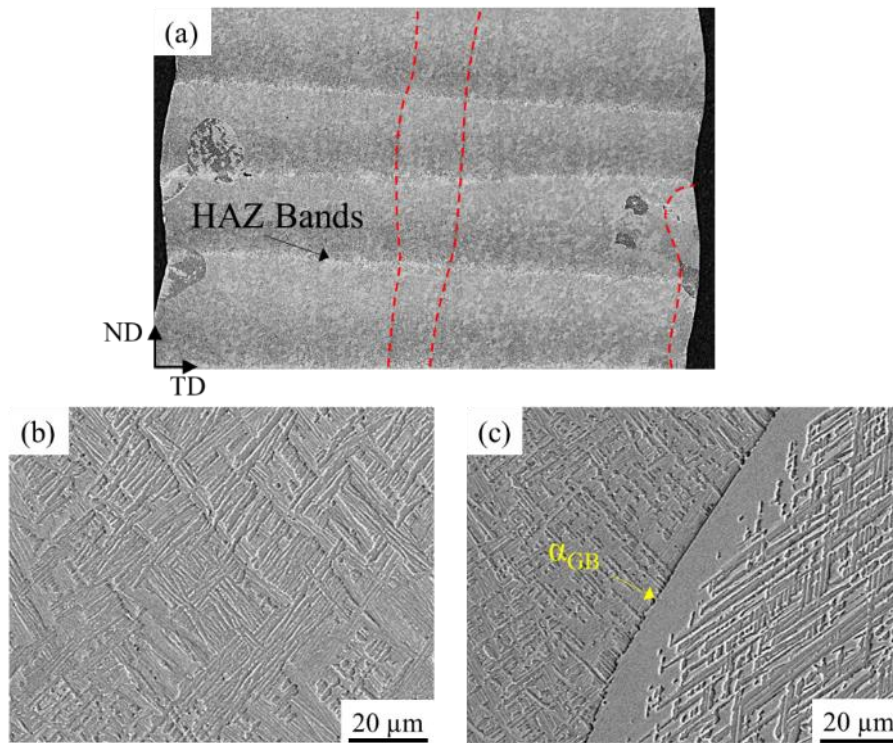


Figure 4.2: (a) Lower magnification optical micrographs of ND-TD plane for showing columnar primary β -grains and heat-affected zone (HAZ) bands, (b) SEM image of basketweave alpha microstructure found between two columnar primary β grains (c) SEM secondary electron (SE) high magnification images showing typical transformation microstructure.

Figure 4.2a also shows coarse columnar primary β grains growing along the deposited layers and aligning close to the build direction (ND), resulting from a steep thermal gradient at the solidification front in a heated melt pool [171–173]. During the deposition process, reheating of the previously deposited layers by the plasma arc causes reheating above the β transus and remelting, depending on the distance from the heat source. This

allows the residual β to re-form the primary β grain structure produced in the previous deposition track below the new fusion boundary. When combined with the low constitutional supercooling of Ti64, this results in solidification primarily by epitaxial growth from the grains that re-form at the fusion boundary and large columnar beta grains can then develop through multiple deposition layers [174]. Figure 4.2b and 4.2c show higher magnification SEM micrographs of the typical transformation microstructure between two HAZ bands. Classical $\alpha + \beta$ microstructures with both basketweave morphologies can be seen with an average α lath width approx. $0.9 \mu\text{m}$.

4.3.2 Tensile testing

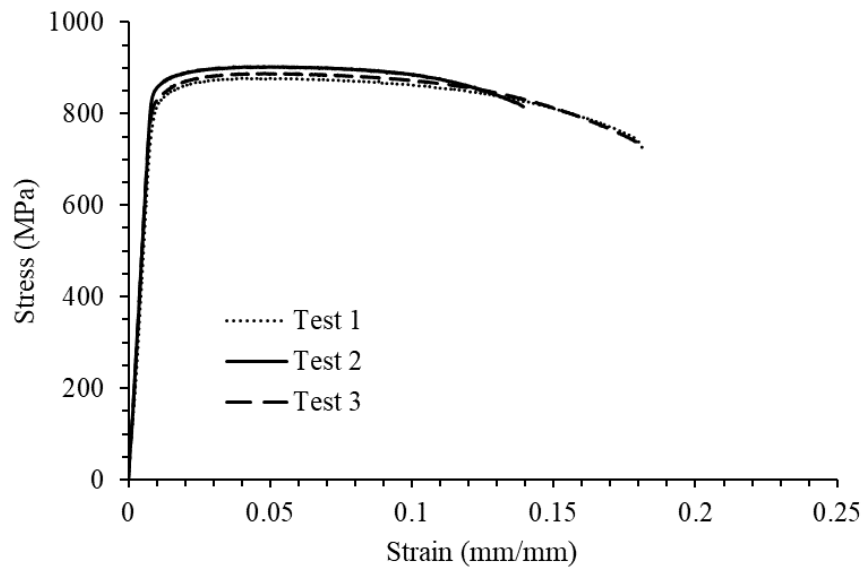


Figure 4.3: Tensile test curves of three vertical extracted samples

Figure 4.3 shows the stress-strain curves of three samples tested in vertical orientation. The average values of yield strength (YS), ultimate tensile strength (UTS) and elongation (%) are 872 ± 16 , 952 ± 9 and 17.5 ± 4 respectively. It was observed the tensile properties in parallel build WAAM Ti64 were better than oscillation build due to the smaller α lath size, similar to single pass WAAM Ti64 [175]. This smaller α lath delays onset of plastic deformation resulting in higher YS and UTS values.

4.3.3 Small crack growth behaviour

Evolution of the lead cracks in small crack samples noted as SC-Test 1 and SC-Test 2 in the ND-TD plane can be observed in Figure 4.4a and 4.4b, respectively. The crack branching and crack coalescence was captured for both tests. However, in SC-Test 1 (Figure 4.4a), the secondary crack was initiated after 1.2×10^6 cycles, which later joined the primary crack and continued until the sample's failure. On the other hand, the primary crack grows continuously in SC-Test 2 with slight crack deviation and branching, as seen in Figure 4.4b. The crack tortuosity is then calculated and presented in Figure 4.5.

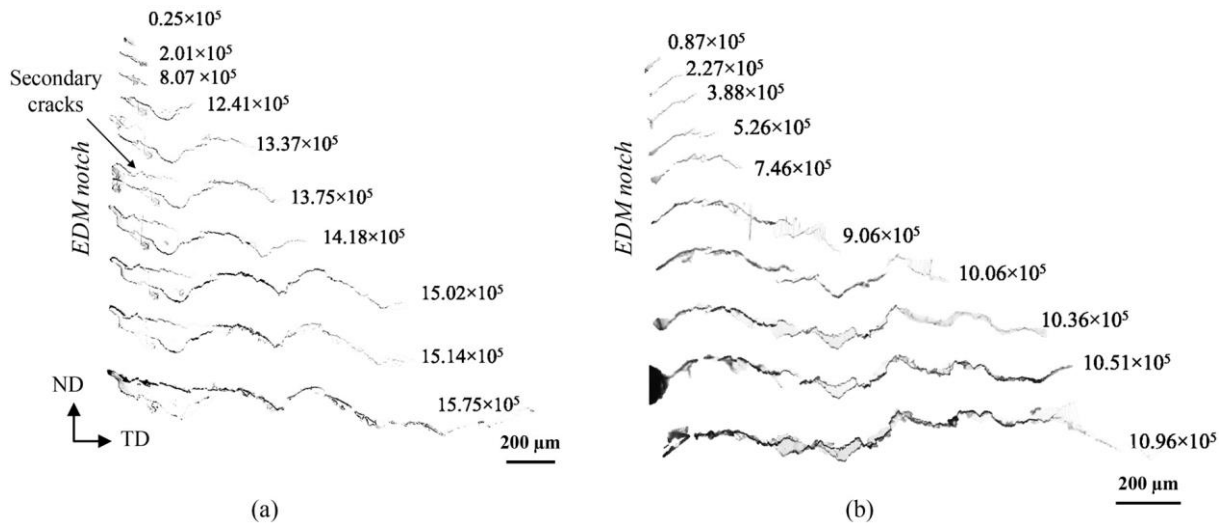
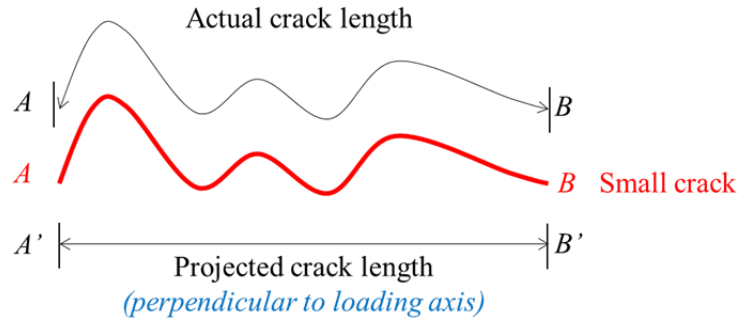


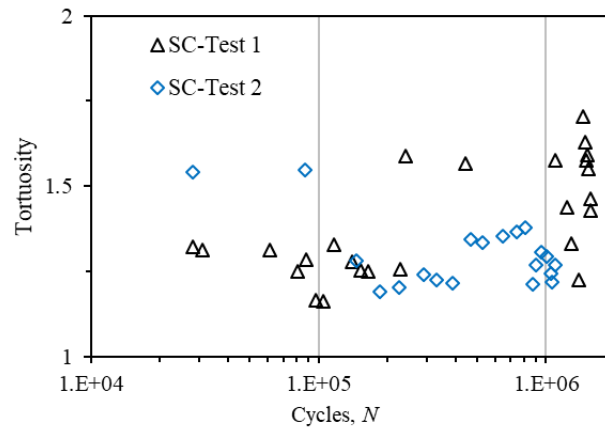
Figure 4.4: Evolution of the lead crack at different number of cycles in the interrupted test of small crack samples; (a) SC-Test-1, (b) SC-Test-2

Figure 4.5a shows the schematic of actual and projected crack length and the crack tortuosity of both samples. Crack tortuosity is defined by an actual crack length over the projected crack length and indicates the deviation of the crack from its path (in general, which is normal to the loading direction in this case). The crack tortuosity was generally higher for SC-Test 1 (Figure 4.5b). The tortuosity during small crack growth is due to the variation in the local microstructure and crystallographic orientation at the crack front [35,176]. It has been reported that small cracks grow faster in the coarse microstructure as compared to fine lamellar microstructure [42,125,177]. In the case of WAAM Ti64, a combination of Widmanstätten and colony microstructure is reported [167,171]. When

the crack approaches β grain boundaries or an α colony, a lower crack growth rate was observed in both samples [42]. This is because these boundaries provide resistance to small crack growth. Hence, a greater number of α laths provide more resistance to small crack propagation and crack retardation was observed.



(a)



(b)

Figure 4.5: (a) Schematic of actual and projected crack length (b) evolution of tortuosity (tortuosity = actual crack length/projected crack length) of a lead crack in each test. Note: actual crack length was measured using ImageJ

It was further observed that in the notch area the crack was deflected and bifurcated in both samples. Secondary cracks were also observed, and they later joined the primary crack (Figure 4.4a, near to the starter notch). The crack bifurcation and secondary crack formation reduced the crack growth rate in the early stage of crack growth. The crack growth rate increased rapidly as the crack grew longer after the crack length exceeded 0.75 mm. In general, small crack growth rate is affected by the variations in the

microstructure and crystallographic texture at the crack front [35,176,178]. If the small crack is encountered with different orientation of crystallographic texture along the crack front, it causes the crack to locally deviate from its path and grows in the favourable direction governed by local slip systems [176]. Hence it fulfils the first criteria stated by Suresh [133].

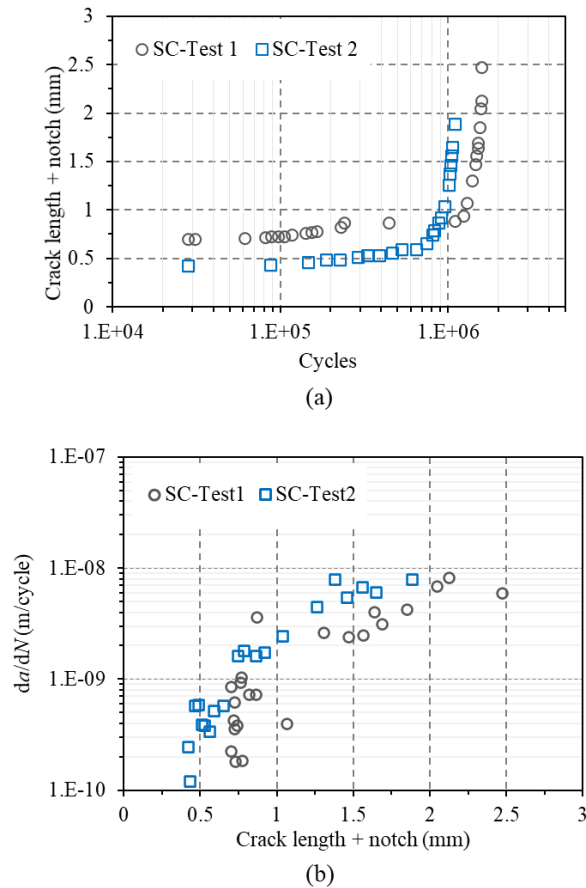


Figure 4.6: (a) Small crack test results: (a) a vs. N ; crack length was measured by replication of the lead crack, and the projected crack length was plotted, (b) da/dN vs. a . (Note: crack length includes the notch size).

To monitor the crack propagation behaviour and crack growth rate, projected crack lengths were then measured and plotted against the load cycle numbers in Figure 4.6a. Specimen SC-Test 2 had a higher applied stress range (185 MPa). Hence the sample failed earlier than SC-Test 1 (135 MPa). However, the crack growth rates of both samples are comparable, Figure 4.6b, as the stress intensity factor governs them. Coalescence of the

lead and secondary cracks did not cause noticeable changes in crack growth rate. However, considerable scatter found in both tests (Figure 4.6b) could be associated with the observed crack coalescence. It is further observed that the crack growth rate in both samples was considerably lower when the crack length was below 0.75 mm. As the crack grew longer and the crack length went beyond 0.75 mm, the crack growth rate increased rapidly.

For calculating the K values of the small crack test sample, the aspect ratio (a/c) of the corner crack was measured from the fracture surface shown in Figure 4.7a, which was 1.01 for sample SC-Test 1, and 1.35 for SC-Test 2. The crack grew in the shape of quarter-elliptical or near to quarter-circular (Figure 4.7a). Therefore, the K value was calculated by the Newman-Raju empirical model [164] shown here as eqs. (4.1)-(4.3).

$$K = S \sqrt{\frac{\pi a}{Q}} F_c \left(\frac{a}{c}, \frac{a}{t}, \phi \right) \quad (4.1)$$

$$F_c = \left[M_1 + M_2 \left(\frac{a}{t} \right)^2 + M_3 \left(\frac{a}{t} \right)^4 \right] g_1 g_2 f_\phi \quad (4.2)$$

$$Q = 1 + 1.464 \left(\frac{c}{a} \right)^{1.65}, \quad a/c > 1 \quad (4.3)$$

where Q is the shape factor, F_c the boundary correction factor S is the applied stress parallel to the ND, a and c are the crack lengths defined to be the projected lengths perpendicular to the loading direction. At the same time t represent the width and thickness of the sample and ϕ is the angular function. The detailed calculation of the procedure can be found in [164].

However, the Newman-Raju model for quarter-elliptical corner crack [164] can overestimate the K value for samples tested in this study due to the starter notch shape differences. Hence, the finite element (FE) modelling was also conducted in this study.

The FE model was firstly verified with the Newman-Raju model [164] for a quarter-elliptical notch before being applied for the notch shape of the test samples used in this study.

4.4 Calculation of the stress intensity factor

To evaluate the performance of the FE model in ABAQUS, the comparison of K values was made against the benchmark example for verification. The benchmark studied for this purpose was the quarter-elliptical corner crack, one of the recommended geometries by ASTM E647-15 [36].

The linear elastic fracture mechanics (LEFM) approach was then followed to calculate the K value using the displacement extrapolation method [130]. The displacement field around the crack tip under Mode I loading condition is given in Figure 4.8, and for linear elastic materials can be written as [130]:

$$v = \frac{K_I}{4\mu} \sqrt{\frac{r}{2\pi}} \left[(2\kappa+1) \sin \frac{\theta}{2} - \sin \frac{3\theta}{2} \right] \quad (4.4)$$

As shown in Figure 4.8, v is the displacements in the local Cartesian coordinate system, r and θ are the local cylindrical coordinates system at the crack tip, and K_I is the stress intensity factor under Mode I loading direction.

Material constants κ and μ are functions of the elastic properties; $\kappa = (3-\nu)/(1+\nu)$ (plane strain), $\kappa = 3-4\nu$ (plane stress), and shear modulus $\mu = E/2(1+\nu)$.

In this study, crack length refers to the crack size at the sample surface (crack length " a " in Figure 4.7b). Therefore, the plane stress condition was used for calculating the K values. For $\theta = 180^\circ$, eq. (4.4) is expressed as eq. (4.5)

$$K = \frac{E\nu}{4} \sqrt{\frac{2\pi}{r}} \quad (4.5)$$

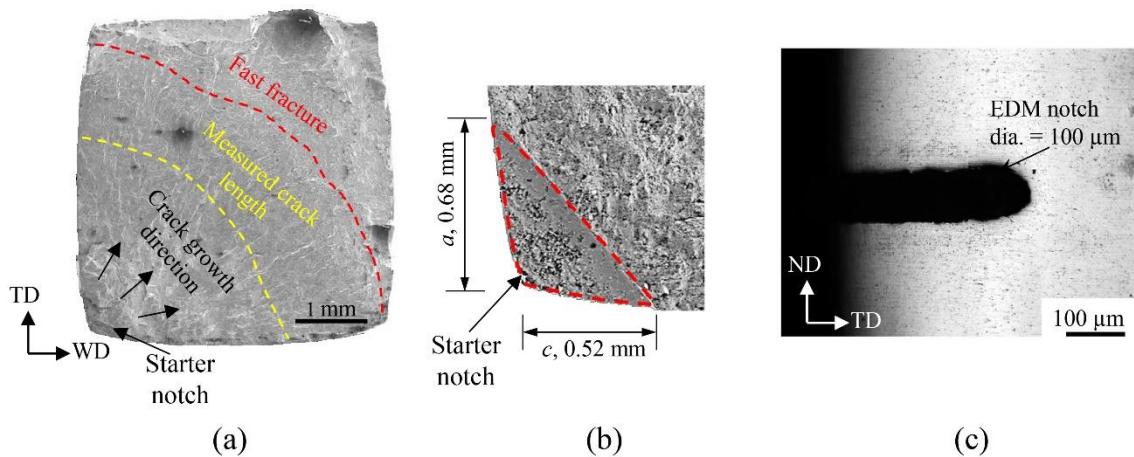


Figure 4.7: (a) Secondary electron SEM image of a typical fracture surface of the small crack sample showing the EDM starter notch, crack initiation location from the notch, crack propagation FE modelling benchmark direction, and fast fracture region, (b) Higher magnification image of the starter notch and dimensions, (c) optical microscopy image of the starter notch before the start of the test.

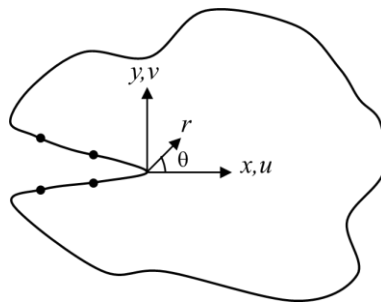


Figure 4.8: Schematic showing crack tip displacement adapted from [130].

To model the benchmark examples, an FE model was created from the gauge section of the small crack sample, as can be seen in Figure 4.9. The linear elastic properties were used to calculate the K values while the modelling was done in ABAQUS 6.14 software

package [179]. The small crack sample with $t = b = 4$ mm and crack length $a = 0.7$ mm and $c = 0.63$ mm was modelled, as shown in Figure 4.9. Symmetric boundary condition was applied on the TD-WD plane (highlighted in Figure 4.9a). A stress value of 150 MPa was applied parallel to the ND for this study. A 10-node tetrahedron element with an approximate size of 0.006 mm at the crack front was used and was selected after the mesh convergence study (Figure 4.9b and 4.9c). Contour maps of the stress component in the loading direction (noted as S33) are shown in Figure 4.10a. As shown in Figure 4.10b, the displacement field is obtained by selecting appropriate material points, and K was calculated using eq. (4.5) with the displacements v . The K values calculated using the displacement extrapolation method for four different crack lengths (CL-1, CL-2, CL-3 and CL-4) is shown in Figure 4.10c-4.10f.

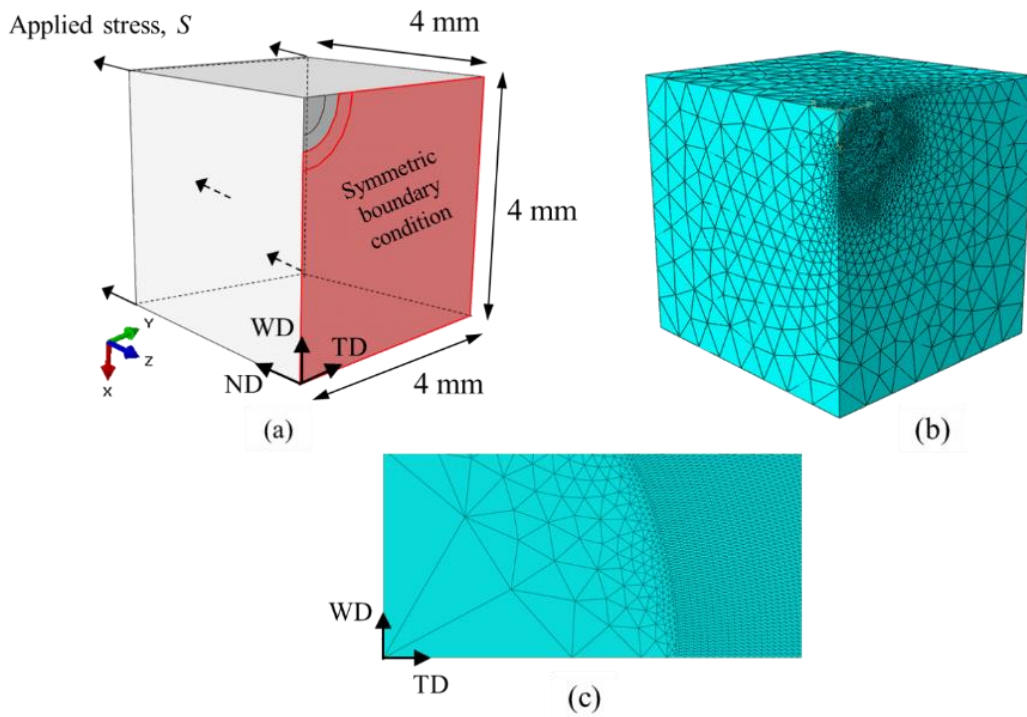


Figure 4.9: The half model of quarter elliptical corner crack sample showing (a) partition definition and boundary condition (b) meshing strategy and mesh refinement around the crack front (c) mesh distribution near the crack front.

To verify the FE model, stress intensity factors calculated by FE analysis for the four different crack lengths (CL-1, CL-2, CL-3 and CL-4) were compared with Newman-Raju

empirical solution of quarter-elliptical crack and are presented in Table 4.1. There is a difference of approx. 5% in stress intensity factors calculated by FE and Newman-Raju for all the selected crack lengths. Hence, a starter notch with different geometry was modelled to calculate K of the small cracks initiating from the EDM notch.

Table 4.1: Comparison of Newman-Raju and FEA results

Crack	a (mm)	c (mm)	K (N-R)	K (FEA)	%age difference
CL-1	0.7	0.63	4.41	4.65	5.27
CL-2	0.74	0.68	4.59	4.83	5.01
CL-3	0.78	0.74	4.8	5.06	5.02
CL-4	0.87	0.86	5.2	5.50	5.47

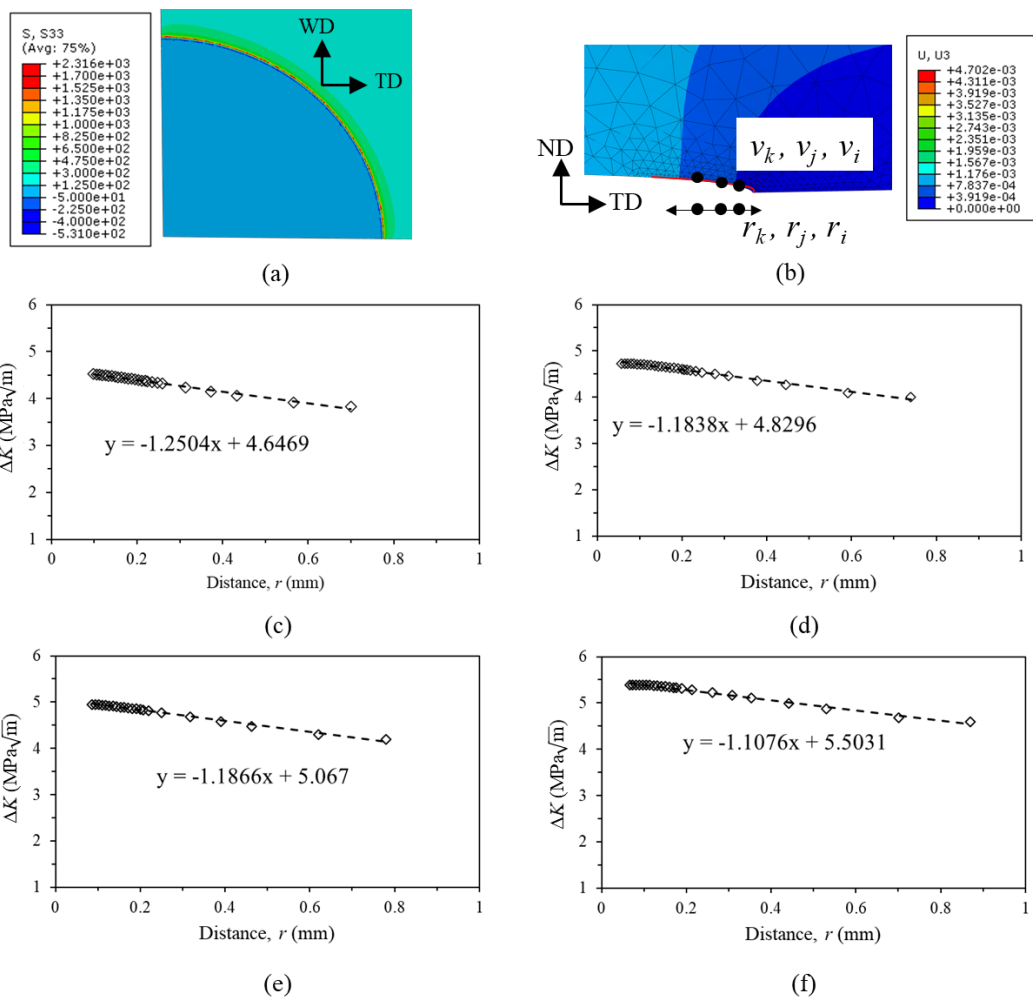


Figure 4.10: (a) S33 stress contour maps around quarter-elliptical corner crack (b) U3 displacement field in ND-TD plane, (c-f) K values calculated by displacement

extrapolation method for CL-1, CL-2, CL-3 and CL-4, respectively. Applied stress was 150 MPa for this illustration

4.4.1 FE modelling of EDM notch

To calculate the K of the crack growing from the starter notch, it was modelled along with the crack extension. The actual shape and size of the notch can be seen in Figure 4.7a-c. The FE model corresponds to model geometry, and the boundary condition is shown in Figure 4.11a and b. This approach also follows the linear elastic fracture mechanics to calculate the K of the small crack initiating from the notch. The FE mesh consists of quadric tetrahedron elements, and the mesh is refined ahead of the crack front curvature of the EDM notch to ensure convergence of K values.

FE calculated K from the EDM notch is presented in Figure 4.12 and compared with the Newman-Raju analytical solution. It shows that the K values for cracks extended from the triangular-shaped starter notch were about 22% lower than the Newman-Raju solution for cracks extended from a quarter-elliptical starter notch. The FE work also modelled the notch root curvature of a 0.1 mm diameter in the test samples (Figure 4.7c) that resulted from the wire-EDM cut. In contrast, the Newman-Raju analytical method assumes a sharp notch root, i.e. without a curvature front [164].

Using value 0.3 for the Poisson's ratio in eq. (4.4), the plane-stress K ratio (for a crack at the plate surface) over plane-strain K (crack length at the point of maximum crack penetration) is 0.91. This ratio factor was originally proposed by Jolles & Tortoriello with a value of 0.91 and was related to the crack closure differences at the two crack locations [180]. It is essentially the same argument based on the variation in the constraint along the crack border, from plane stress at the plate surface to that of plane strain at the point of maximum crack penetration. This ratio factor was proposed to improve life prediction accuracy based on early studies on crack growth predictions of semi-elliptical surface and quarter-elliptical corner cracks that demonstrated that the crack growth could not be predicted solely by stress intensity factor ranges [180,181]. To account for this difference, Jolles and Tortoriello [180] multiplied the stress intensity factor range at the free surface by a factor of 0.91, and Newman and Raju [181] used a factor of 0.9.

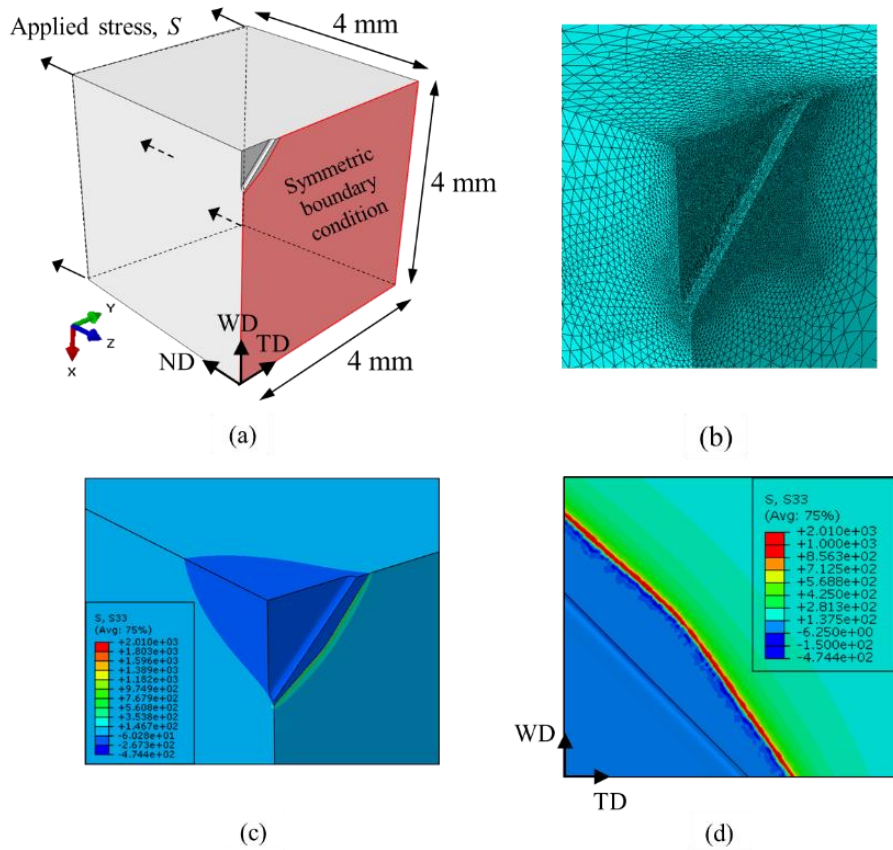


Figure 4.11: Finite element model of one-half of the test sample: (a) starter notch with a small crack extension of 0.1 mm, load and boundary conditions, (b) FE mesh, (c) and (d) contour maps of stress in load direction (S_{33}). Applied stress was 150 MPa for this illustration.

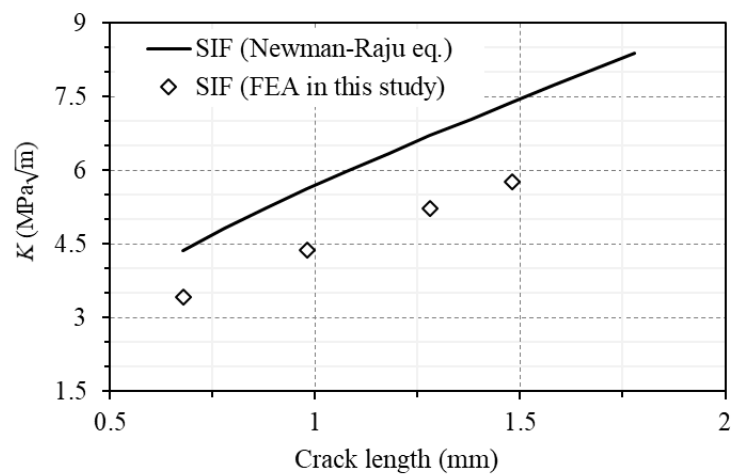


Figure 4.12: Calculated stress intensity factor for the small crack sample with initial notch being modelled as quarter-elliptical shape (Newman-Raju eq.) or triangular (FEA). Applied stress = 150 MPa, crack length includes notch size.

4.5 Predicting small crack growth behaviour

Calculated small and long crack growth rates are plotted together in Figure 4.13. It shows that small cracks had higher growth rates than the long cracks at the same applied ΔK . The difference in crack growth rates is associated with the difference in constraints imposed by the elastic material surrounding the crack, which may be different in small cracks [133]. The constraint exerted at small cracks initiating from or growing on a free surface of smooth samples is different from the through-thickness long crack in the same material [180]. Therefore, even when the loading condition and the crack size satisfy the requirement of LEFM, the physical smallness of the crack generates faster crack growth rates. Long cracks with longer plastic wake will slow down the crack growth rate further [133].

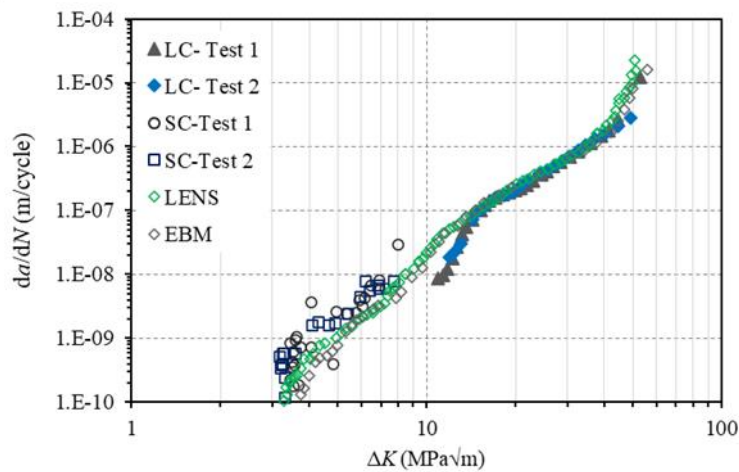


Figure 4.13: da/dN vs. ΔK for the long crack (LC) [119,162] and small crack (SC) samples tested in this study. The long crack data shows small cracks growing faster under the same applied ΔK .

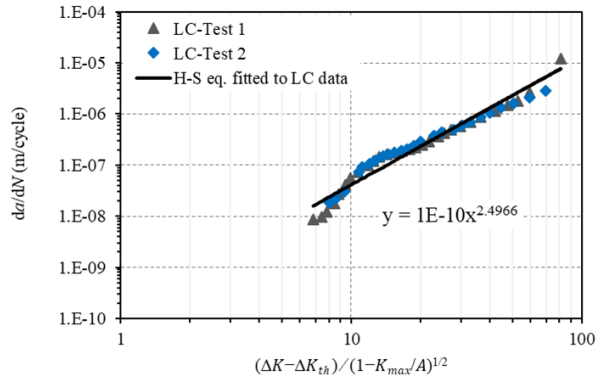
Moreover, the small cracks are comparable to the α colony size of WAAM Ti64 and are hence affected by the crystallographic orientation of the grains [14,42]. Consequently, local plastic zone sizes are different from the long fatigue cracks [133]. These microstructural and crystallographic orientations have a substantially diminished effect on the growth of long cracks [133,177]. In the case of long cracks, the crack tip interacts with a larger number of grains; hence the bulk material properties govern the fracture behaviour. Furthermore, small cracks do not have the crack closure effect, further increasing the crack growth rate under the same applied ΔK .

In this work, long crack test data da/dN with R ratio 0.1 obtained from [162] was plotted against $\Delta\kappa$ in a log-log graph in Figure 4.14a. The material constants were calculated as $D = 1 \times 10^{-10}$ and $p = 2.49$ in units of MPa and m through the linear fitting of the test data with an $R^2 = 0.96$. It can be seen that the modified Hartman-Schijve equation, eq. (3.22) well represent the crack growth rate of the long cracks with values $A = 90 \text{ MPa}\sqrt{\text{m}}$ [140] and long crack threshold $\Delta K_{\text{th}} = 4.5 \text{ MPa}\sqrt{\text{m}}$ [13].

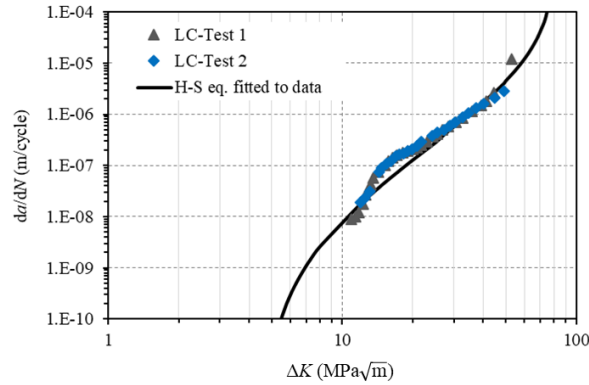
Using eq. (3.22), fitted da/dN vs. applied ΔK is presented in Figure 4.14b and compared with test measured long crack growth data. Moreover, eq. (3.22) also describes the asymptotic behaviour in the threshold and fast crack growth regions. Note, stress intensity factor threshold for long cracks ΔK_{th} used for this fitting is $4.5 \text{ MPa}\sqrt{\text{m}}$.

The small crack growth rate was then predicted using eq. (3.22), using material constants D and p obtained from long crack test data (Figure 4.14a) and a smaller ΔK_{th} value based on findings in [35,140,182,183], where the value of ΔK_{th} was set much smaller than the long crack threshold value in order to make small cracks grow. In Jones' papers [41,111,145,154], this small crack growth threshold was noted as ΔK_{thr} , and small crack da/dN vs. ΔK was approximated by setting the ΔK_{thr} to a very small value of $0.3 \text{ MPa}\sqrt{\text{m}}$. Values suggested by [41,111,145] may be suitable for microstructurally small cracks but may be impractical for small cracks initiated from defects found in WAAM Ti64 as work in [35,182,183] found higher ΔK_{thr} values for small cracks in Ti64 as $1.8\text{--}3.0 \text{ MPa}\sqrt{\text{m}}$. In

this study, $\Delta K_{thr} = 2 \text{ MPa}\sqrt{\text{m}}$ was used in eqs. (3.22)-(3.24) for predicting the small crack growth behaviour in the selected material.

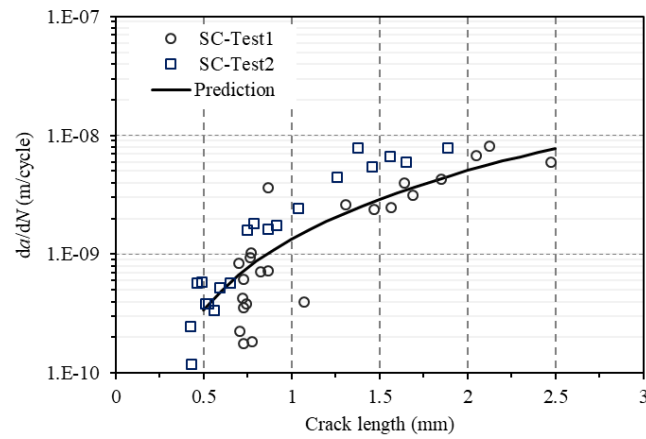


(a)

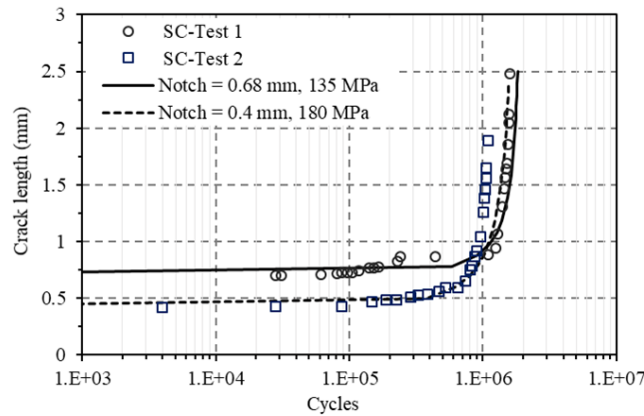


(b)

Figure 4.14: H-S equation fitted to long crack test data: (a) da/dN vs. $\Delta \kappa$ for determining material constants D and p by the fitting curve, (b) da/dN vs. ΔK . Material data used in eq. (3.21): $A = 90 \text{ MPa}\sqrt{\text{m}}$ and $\Delta K_{th} = 4.5 \text{ MPa}\sqrt{\text{m}}$.



(a)



(b)

Figure 4.15: Small crack behaviour and comparison of test results with prediction using eq. (3.21): (a) da/dN vs. a , (b) a vs. N (Note: crack length includes the notch size.)

Therefore, using the small crack ΔK_{thr} in the modified H-S equation can establish a unified equation for small and long crack growth regions. To demonstrate the capability of the equation, the fatigue life of the small crack samples was calculated by numerical integration of eq. (3.22) using material constants obtained from Figure 4.14a. Comparison of prediction with test measurement is shown in Figure 4.15. The da/dN vs. crack length data in Figure 4.15a had large scatters. Nevertheless, the prediction lies within the test data band. For the a vs. N prediction (Figure 4.15b), two different initial crack lengths were used; 0.68 mm and 0.4 mm for specimens tested at applied stress range 135 MPa and 180 MPa, respectively. Considering the scatters in the tests, the prediction is in good agreement with the experimental results.

Figure 4.16 shows good agreement between the predicted and test measured crack growth rates for the small crack specimens. It also shows a good comparison with the work performed by Jones et al. [111] on a Ti64 alloy made by selected laser melting (SLM) process, using $D = 2.79 \times 10^{-10}$ and $p = 2.12$ in eq. (3.21).

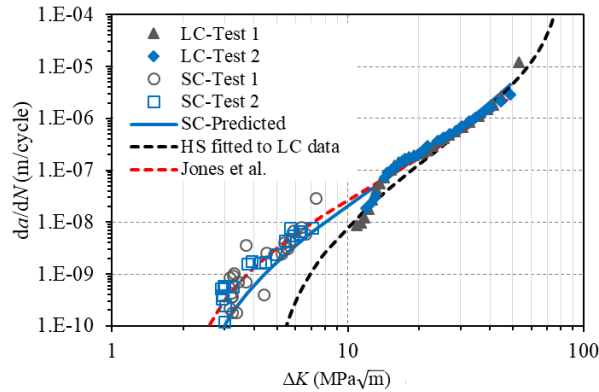


Figure 4.16: Prediction of small crack growth rate using long crack data fitted H-S equation with $\Delta K_{thr} = 2 \text{ MPa}\sqrt{\text{m}}$, and comparison with a prediction in the literature on SLM Ti64 [111].

4.6 Summary

Based on the studies in this Chapter, key points are summarised below:

The small crack growth behaviour shows deviation and branching from the main path (perpendicular to loading direction) and associated with local microstructure and crystallographic orientation. Suppose the small crack has encountered obstacles in the path, for instance, different crystallographic orientation along the crack front. In that case, it causes the crack to move locally out of the main propagation plane in the directions governed by slip systems.

The optical microscopic and fracture surface analysis of the small crack sample shows the EDM notch has curvature rather than a sharp crack. Hence, the assumption of Newman-Raju quarter-elliptical crack could overestimate the crack driving force, K , leading to overestimation of fatigue life. Hence, to identify the crack driving force

accurately, a finite element model was created. The models were initially verified through a benchmark analysis with the Newman-Raju empirical solution, which gave a constant difference of ~5% for four different crack lengths. The EDM notch was then modelled in ABAQUS, and K was calculated using the displacement extrapolation method. It was found that K values are approx. 16% lower than the empirical solution proposed by Newman-Raju.

It is proposed that small crack growth behaviour can be predicted using the Hartman-Schijve variant of the NASGRO equation. Using appropriate ΔK_{thr} for the small crack, the behaviour of small and long crack can be captured. It was further observed that using a very small ΔK_{thr} of $0.3 \text{ MPa}\sqrt{\text{m}}$, which is for naturally occurring microstructural cracks, the prediction is over-conservative. However, using $\Delta K_{thr} = 2 \text{ MPa}\sqrt{\text{m}}$, as suggested in the literature, a reasonable prediction was achieved. Prediction of small crack data based on long crack data can be verified for other deposition strategies and can save a significant amount of time for testing small crack samples. It was also observed that the Hartman-Schijve variant of the NASGRO equation captures the small and long crack growth behaviour and can be used as a unified approach to predict the fatigue life of WAAM components.

Chapter 5

Durability of as-deposited WAAM Ti-6Al-4V: Experimental investigation

5.1 Introduction

Only a few published works are available on the fatigue behaviour of WAAM Ti64. Wang et al. [12] tested it in machined and polished surface condition, under uniaxial tensile fatigue, but only tested at one maximum stress of 600 MPa at an R ratio of 0.1. Significantly better fatigue property was found than the conventionally manufactured samples except for a few samples where early crack initiation was reported due to the defects that degraded overall fatigue strength. Biswal et al. [13] performed fatigue testing of WAAM Ti64 by the oscillation built strategy, also in machined and polished surface condition, to study the material performance with and without defects. It was concluded that defects considerably reduced the fatigue life, and a large scatter in the fatigue life was recorded.

Apart from internal defects, like other AM processes, as-deposited surface roughness in WAAM built Ti64 is also a concern. The as-deposited surface of WAAM Ti64 has considerable surface waviness, which often requires machining. Nevertheless, it will result in material waste, increased buy-to-fly ratio, and lead time to deliver the parts. There are, however, some applications where machining may not be required, e.g., parts with shorter design life and/or subjected to lower applied stress. On the other hand, some parts and complex geometries are impossible for machining, e.g., lattice structures. Therefore, the work reported in this Chapter is aimed to provide a systematic investigation of the influence of the as-deposited surface on the fatigue life of WAAM Ti64. The outcomes from this investigation will help to address the durability concerns and could be a key to assure the reliability of WAAM parts for structural applications.

5.2 Materials and methods

5.2.1 Material manufacturing

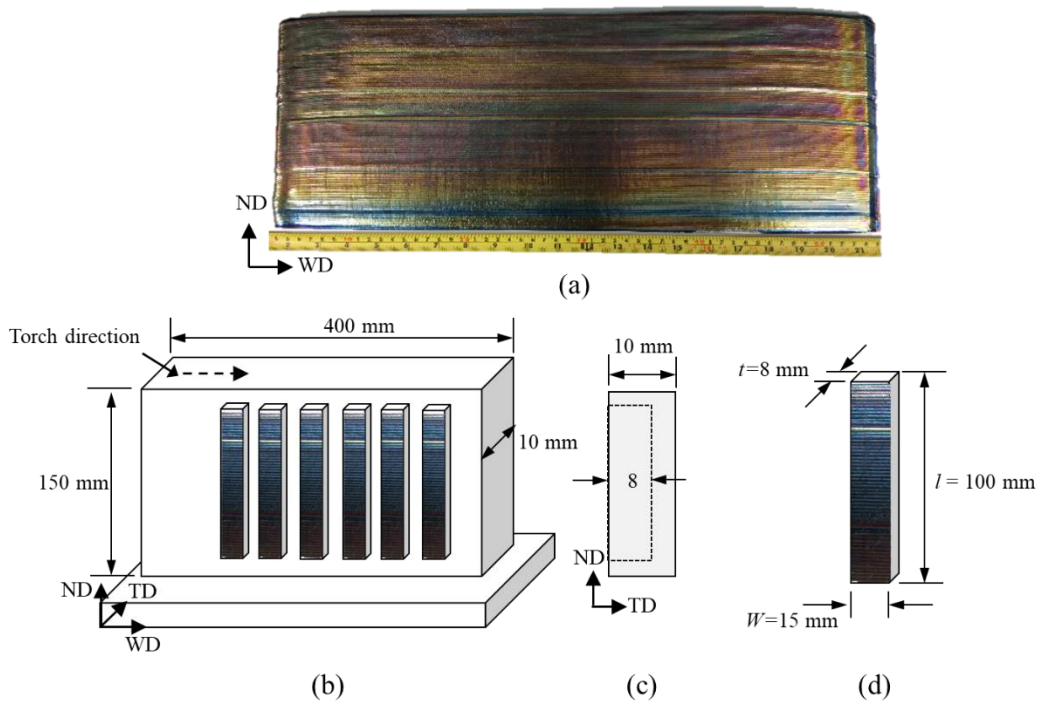


Figure 5.1: (a) Photo of an actual WAAM Ti64 wall built by single-pass deposition method (b) schematic of WAAM Ti64 wall and sample extraction plan (c) location of sample extraction along thickness direction (d) geometry and dimensions of a bending test sample (unit: mm), WD = welding torch movement direction, TD = transverse (thickness) direction, ND = normal direction.

The built strategy for the WAAM wall has been outlined in Chapter 4. Figure 5.1 shows the photograph and schematic of the deposited wall using the single-pass deposition method. After the deposition, the wall was cut off from the substrate plate and used for extracting fatigue testing samples of rectangular shape by electric discharge machining (EDM). The sample extraction plan and the dimensions of the fatigue samples are presented in Figure 5.1b-d, respectively. Two types of samples were extracted, i.e. 24 samples with the as-deposited surface (no machining) and 14 samples with a machined and polished surface. For samples with the machined surface, the sample was first cut from the wall, and the as-deposited surface was removed using high precision milling.

Subsequently, the machined surface was incrementally ground and polished to achieve an average surface roughness of $0.2\ \mu\text{m}$ as recommended by ASTM E466 [184]. In the following text, samples with “as-deposited” surface are called as-deposited samples, and samples with machined and polished surfaces are called machined samples. For the as-deposited samples, one side of the sample was machined to facilitate sample mounting on the bending test frame. In addition, selected as-deposited samples were ground and polished on the ND-TD plane (Figure 5.1b) using SiC paper and polished up to $0.06\ \mu\text{m}$ silica suspension and subsequently etched using Kroll’s reagent for approx. 45 seconds. This was to aid the imaging of the crack propagation path during fatigue testing. Measured crack length vs. load cycle relation was used to compare with predicted crack growth life and presented later in Chapter 6.

5.2.2 Surface roughness characterisation

The as-deposited surface of WAAM Ti64 was analysed using three different metrology techniques as described below.

5.2.2.1 Form tracer

It is a type of contact mode surface characterisation technique where the probe touches and scans the surface. To characterise the surface, the Mitutoyo FT SV-C3200/4500 series with an arm containing a diamond tip stylus of $4\ \mu\text{m}$ diameter was used. A load of 5 mN was applied to keep the stylus in contact with the sample surface. The data were recorded and analysed using SurfAnalysis software to calculate different surface roughness parameters [185].

5.2.2.2 White light interferometer

It is a non-contact optical measurement technique where a white light beam is used to measure the surface waviness. A detailed description of WLI is given in [186]. A Bruker WLI was used to characterise the surface roughness, with a total of 8 images being taken across 6 mm length with each image of $0.9\ \text{mm} \times 1.2\ \text{mm}$ and an overlap of 20%. All the

images were reconstructed using VISION64 software, and from the reconstructed images, surface roughness parameters were calculated using the same software.

5.2.2.3 Optical microscopy

Carl Zeiss optical microscope with AxioVision software was used to characterise the surface waviness of as-deposited samples. The surface waviness measurements were performed at 100× magnification, and a total of 8 images were stitched together to get the as-deposited surface profile.

The measurement data were analysed to calculate different surface roughness parameters, i.e. the arithmetical mean height, R_a , the maximum valley depth, R_y , and the average of five maximum heights and maximum valley depths, R_z [185,187]. These surface roughness parameters are shown schematically in Figure 5.2 and defined by eqs. (5.1)-(5.3).

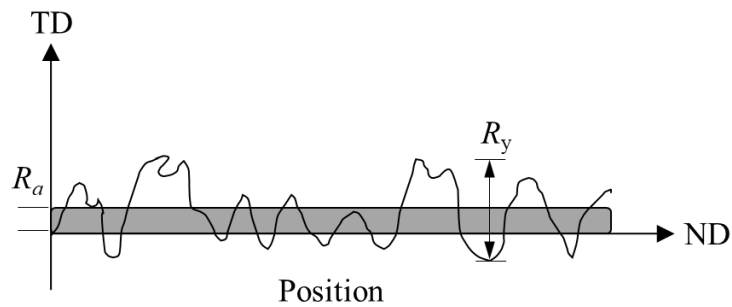


Figure 5.2: Schematic representation of surface roughness parameters: the arithmetical mean height, R_a , the maximum valley depth, R_y , while R_z is the average value of five R_y (eq. (5.3))

$$R_a = \frac{1}{n} \sum_{i=1}^n |y_i| \quad (5.1)$$

$$R_y = |y_{max} - y_{min}| \quad (5.2)$$

$$R_z = \frac{1}{5} \left[\sum_{i=1}^5 |y_i|_{max} + \sum_{j=1}^5 |y_j|_{min} \right] \quad (5.3)$$

5.2.3 Characterisation of a single notch

Using conventional surface roughness parameters to infer information regarding fatigue life is irrelevant to bending fatigue samples as the centre notch plays a much more dominant role than the average roughness parameter R_a . Therefore, in addition to the commonly used surface roughness parameters (R_a , R_y and R_z), a typical notch was further characterised to determine the notch depth (d), the notch mouth opening angle (θ) and radius of curvature at the notch base (r) (Figure 5.3a). For calculating r , a polynomial equation was generated (Figure 5.3b), which was used to compute the first and second derivative, $f'(z)$, $f''(z)$, used in eq. (5.4) [188].

$$r = \frac{(1 + [f'(z)]^2)^{3/2}}{f''(z)} \quad (5.4)$$

To compare the resolution of different metrology techniques r was calculated from the data generated from each technique. Since d and θ were approximately the same for the given techniques, they are not included in the comparison. From Table 5.1, it can be seen that the form tracer (FT) with 4 μm stylus diameter and optical microscope (OM) gave almost the same values of r . However, since OM is a destructive technique and requires sample preparation, FT was used to perform the characterisation of as-deposited samples (Figure 5.4a). For each sample, three-line scans were performed in a 60 mm span length (parallel to ND) with a measurement density of 1 μm and a distance of ~ 5 mm in WD

direction between each scan (Figure 5.4b), which has resulted in a total of 60,000 points over 60 mm measured distance for each scan.

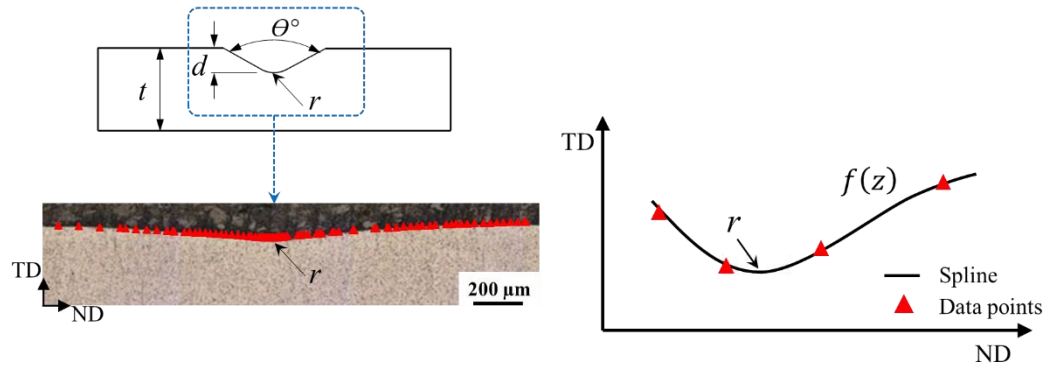


Figure 5.3: Procedures for measurement of notch configuration parameters, starting from identifying notch to optical microscope image of the notch along the TD-ND plane overlapped with metrology data taken from form tracer (FT) and spline created using metrology data to calculate r of the notch.

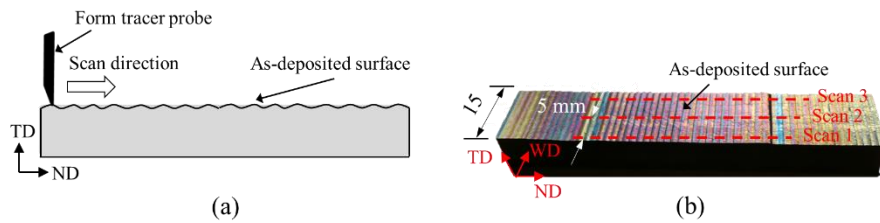


Figure 5.4: (a) Schematic showing surface characterisation of as-deposited WAAM Ti64 using a form tracer, (b) three-line scans on each sample at a distance of approx. 5 mm.

Table 5.1: Comparison of r calculated by eq. (5.4) and measured from OM.

Surface characterisation tool	radius ' r ' (mm)			
	Location 1	2	3	4
WLI	0.20	0.29	0.21	0.19
FT (4 μ m)	0.16	0.23	0.23	0.19
Optical microscopy	0.15	0.21	0.20	0.20

5.2.4 Fatigue testing

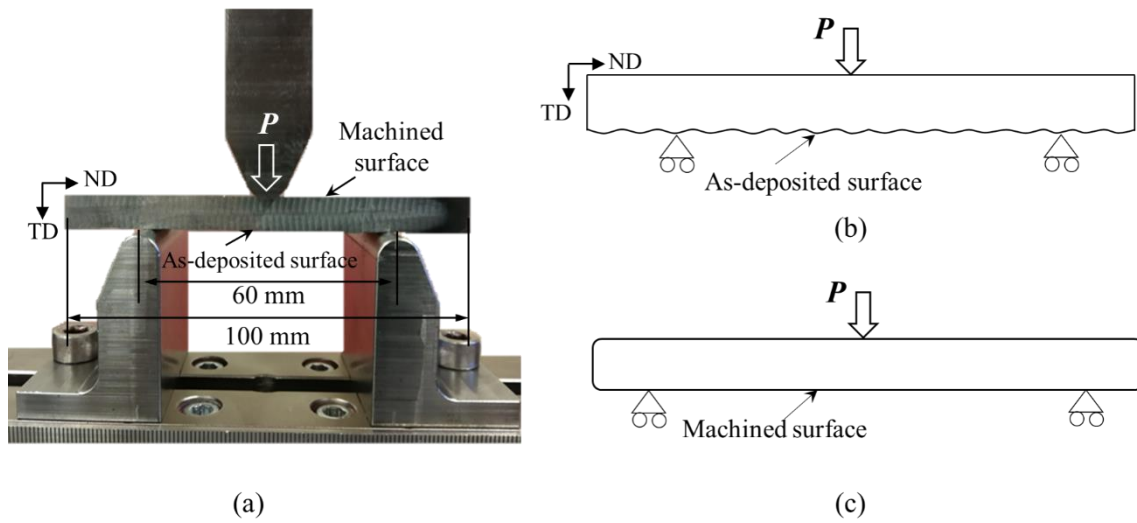


Figure 5.5: (a) 3PB fatigue test setup showing the position of the supporting rollers and plunger with the as-deposited surface facing downwards. Schematic of 3PB fatigue testing of (b) as-deposited sample, (c) machined sample.

Three-point bending (3PB) fatigue test was performed under the load-controlled condition on a 10 kN servo-hydraulic machine. Constant amplitude load with a cyclic load ratio of 0.1 was applied with a sinusoidal mode at a loading frequency of 10 Hz. The experimental setup and schematics of the as-deposited and machined sample are shown in Figure 5.5. The maximum applied tensile stress on the lower surface of the beam specimen was calculated using eq. (5.5) [127]. At least three samples were tested at each stress level for both the as-deposited and machined conditions.

$$S_{max} = \frac{3PL}{2Wt^2} \quad (5.5)$$

where S_{max} is the maximum applied tensile stress in the middle of the sample on the outer surface, P is the applied load, L is the distance between the supporting rollers (beam sample span length = 60 mm), W the width of the sample, and t the thickness of the sample.

To observe the crack growth behaviour, fatigue testing was paused after every 20,000 cycles to monitor the crack initiation using a travelling microscope until the crack had initiated. After that, the test was paused every 2000 cycles until the crack reached a length of ~1.6 mm. As mentioned earlier, crack propagation measurement was performed on a few selected samples. After sample failure, fracture surfaces were analysed using scanning electron microscopy (SEM) to identify the crack initiation location and fracture mechanisms.

5.3 Results and discussion

5.3.1 Effect of surface waviness on fatigue

The stress-life ($S-N$) data of both as-deposited and machined samples is presented in Figure 5.6. It is observed that the machined samples had considerably higher fatigue strength at a given life and achieved longer fatigue life at applied maximum stress of 600 MPa. One machined sample even lasted beyond 10^7 cycles. The as-deposited samples did not reach 10^7 cycles, even at much lower stress of 300 MPa. The reduced fatigue life of the as-deposited samples is due to the stress concentration effect arising from the surface waviness, which resulted in crack nucleation at the groove-like small notches (detailed discussion in Chapter 6). The R_a , R_y and R_z values measured for as-deposited surface were $26.8 \pm 2.8 \mu\text{m}$, $245 \pm 28.9 \mu\text{m}$ and $152 \pm 14.6 \mu\text{m}$, respectively.

It can be further observed from Figure 5.6 that the scatter in fatigue life is different at different applied stress levels in both the machined and as-deposited samples. In the machined samples, the fatigue life scatter is the smallest at 800 MPa applied stress as the stress level gets closer to the yield strength of the material. The fatigue life scatter increased as the applied stress decreased. This is because when testing the machined samples at higher stress, the surface condition is less likely to influence crack nucleation as micro-cracks are formed much earlier in the fatigue life, which is followed by crack growth [189]. As a result, variation in fatigue life is relatively small in all the samples tested at 800 MPa. While at lower applied stress, the surface condition becomes more relevant, and crack nucleation depends on small surface irregularities. These surface

conditions vary from sample to sample, hence the considerable variations for the machined samples tested at 600 MPa. However, for the as-deposited samples, the variation was less at 600 MPa than machined samples because the as-deposited samples were dominated by crack growth, whereas the machined samples' life was dominated by crack initiation.

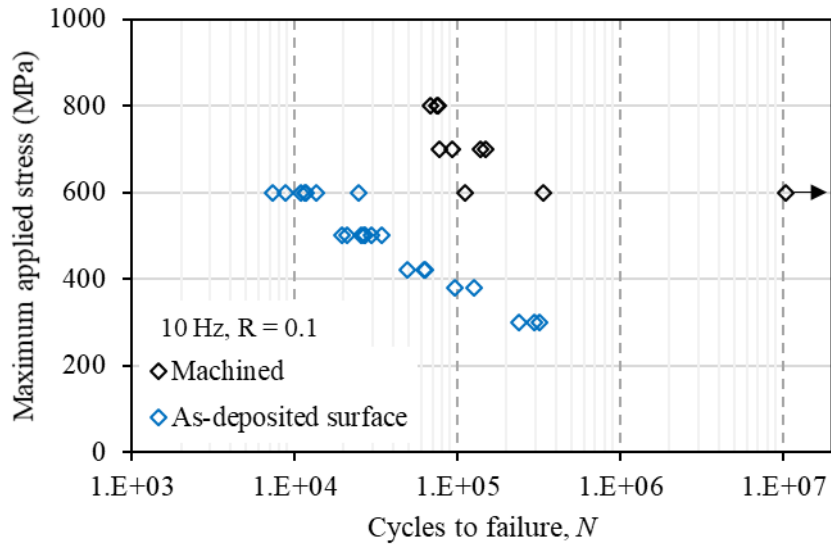


Figure 5.6: S - N data of three-point bending tests for machined and as-deposited WAAM Ti64 samples. Y-axis represents the maximum bending stress on the beam centre.

Several studies in the literature have suggested that reducing the surface roughness had increased the fatigue life of AM parts [17,106,190]. For example, a 60% increase in fatigue life was reported when the R_a value was reduced from 15 to 0.5 μm in the case of SLM Ti64 [26]. While reducing the surface roughness increases fatigue life, no correlation could be established between the R_a and fatigue life for SLM and EBM Ti64 in as-deposited surface condition even when tested in the axial fatigue testing [18].

Therefore, for the as-deposited surface condition, it is almost impossible to designate a reliable surface roughness parameter for fatigue life correlation even if the 'correct' values of the R_a , R_y and R_z are determined [17,20]. For that reason, the traditional surface roughness parameter will not identify the sites prone to crack initiation but instead gives

a universal representation of the sample surface [191]. Furthermore, it was observed that cracks always initiated from a single ‘notch-like’ feature that experienced the maximum tensile stress in the three-point bending test. Therefore, fatigue life is dictated by the geometric parameters of a single ‘notch-like’ feature rather than an average value of surface roughness parameter R_a . Hence, in the next Chapter, it is discussed how this single ‘notch’ was characterised and how its stress concentration factor was determined. In the following sections of this Chapter and Chapter 6, the single surface feature responsible for crack initiation is called ‘notch’.

5.3.2 Crack path in as-deposited 3PB samples

The resultant microstructure affects the crack propagation behaviour of WAAM Ti64, as described in Chapter 4. To study further, the crack propagation behaviour under three-point bend fatigue loading was studied, and for this purpose, three samples were selected out of 24 as-deposited samples for crack growth monitoring. The test setup is shown in Figure 5.7. Out of these three samples, the crack growth behaviour of the two samples is presented in Figures 5.8 and 5.9. It can be seen from Figure 5.8a that during the early stages of crack propagation, crack branching was observed in sample 3PB-Test 1. The crack initially got arrested as it approached the prior β grain boundary (Figure 5.8a, indicated by yellow arrow), where the crack then deviated from the previous crack path, and went to the direction approximately normal to the prior β grain and propagated in the same direction (red arrow) before approaching the prior β grain boundary and re-arrested. After accumulating almost 20,000 load cycles, the lead crack propagated to about 1 mm and arrested again (Figure 5.8b). The secondary crack then nucleated approx. 10 μm away from the primary crack, which continued to grow as a lead crack until the failure of the sample (Figure 5.8c).

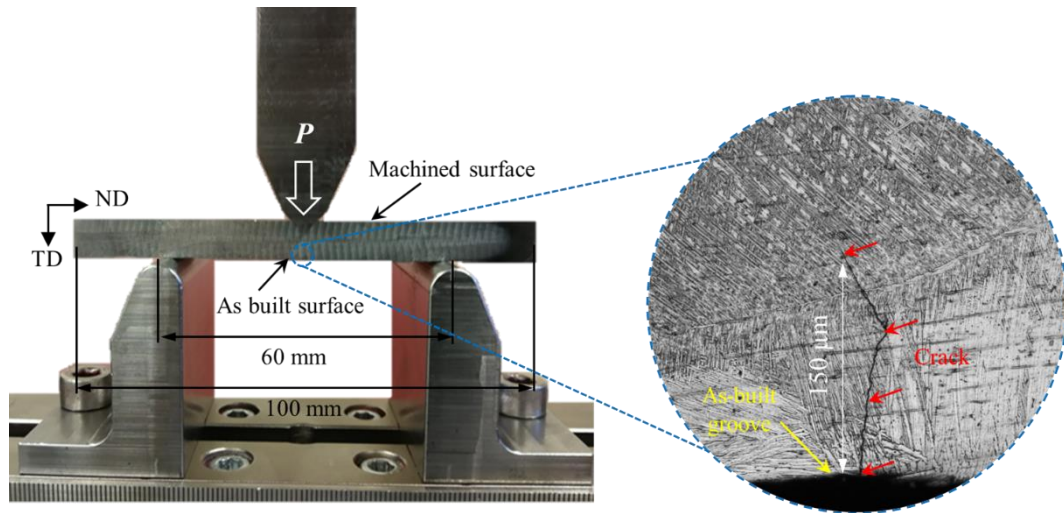


Figure 5.7: Three-point bending fatigue test setup showing monitoring of crack initiation and propagation from a centre “notch”, which was one of the “dents” caused by as-deposited surface waviness.

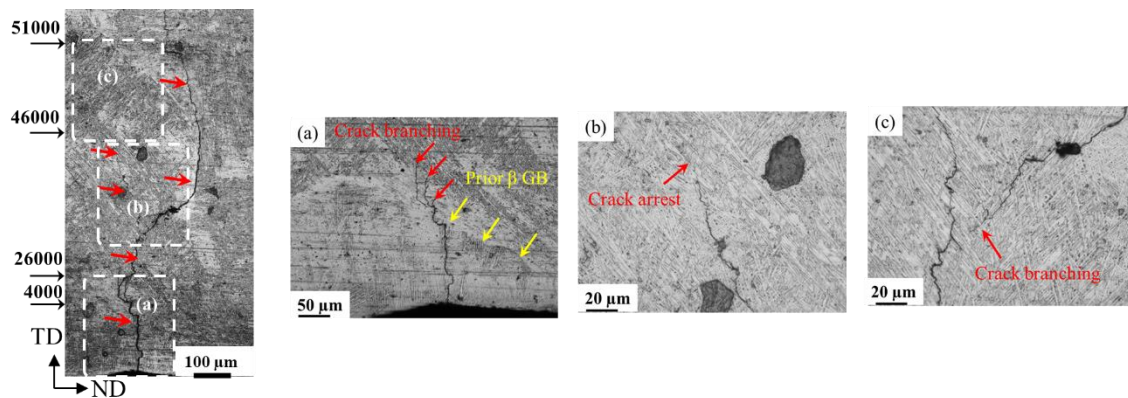


Figure 5.8: 3PB-Test 1 ($\sigma_{\max}=380$ MPa, $N_f=74,000$): Global macroscopic image showing the crack path and detailed zoom views: (a) crack branching near prior beta grain boundary, (b) primary crack arrest at $\sim 46,000$ cycles, (c) secondary crack initiation ~ 10 μm away from the primary crack.

Bantounas et al. [176] studied the crack arrest in rolled Ti64. They observed that the crack arrested at the grain boundary due to a reason that the next grain was favourably oriented for first-order pyramidal $\langle c+a \rangle$ slip with higher Schmid factor values (0.49) as compared to prismatic $\langle a \rangle$ slip system. In contrast, the last grain where the crack had grown, had a high Schmid factor of prismatic slip (0.44) which has a lower critical resolve shear stress

value. Further discussion on Schmid factor calculation and its effect on fatigue life can be found in Chapter 7.

On the other hand, in 3PB-Test 2 presented in Figure 5.9 shows that the primary crack continued to grow until failure with only slight crack branching and deviation. It was further observed that the branched cracks joined the primary crack and did not slow down the overall crack propagation rate.

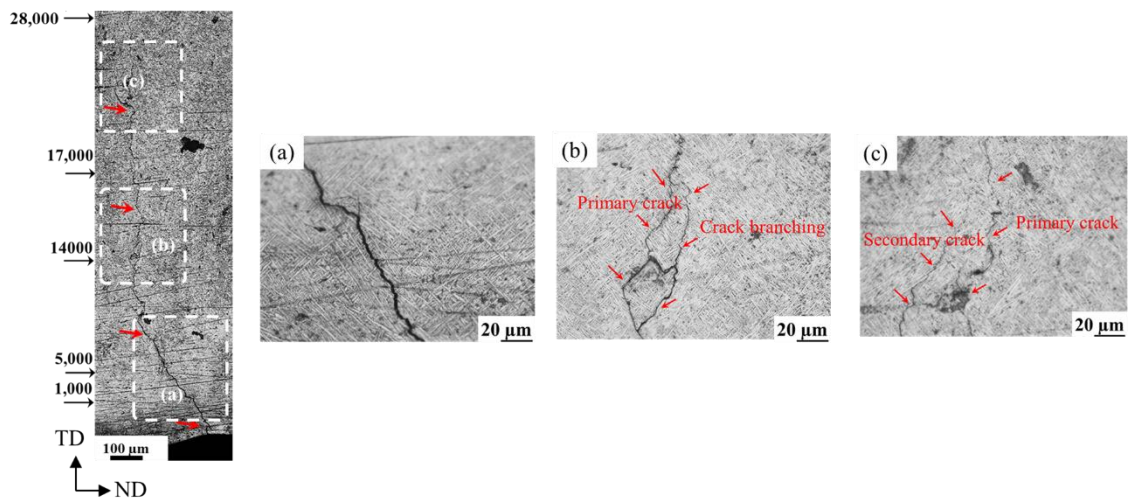


Figure 5.9: 3PB-Test 2 ($\sigma_{\max}=380$ MPa, $N_f= 33,000$): Global macroscopic image showing the crack path and detailed zoom views: (a) lead crack growing in a transgranular manner, (b) branching and coalescence of lead crack at $\sim 14,000$ cycles, (c) secondary crack branching and arrested at around $10 \mu\text{m}$ away from the lead crack.

Crack growth behaviour is plotted as a vs. N relation in Figure 5.10. It shows that the 3PB-Test 1 and 3PB-Test 2 (with maximum applied bending stress 380 MPa) failed marginally earlier than 3PB-Test 3 (bending stress 300 MPa), but the crack growth rate was the same as indicated by the identical slope of all tests in the a vs. N graph (Figure 5.10).

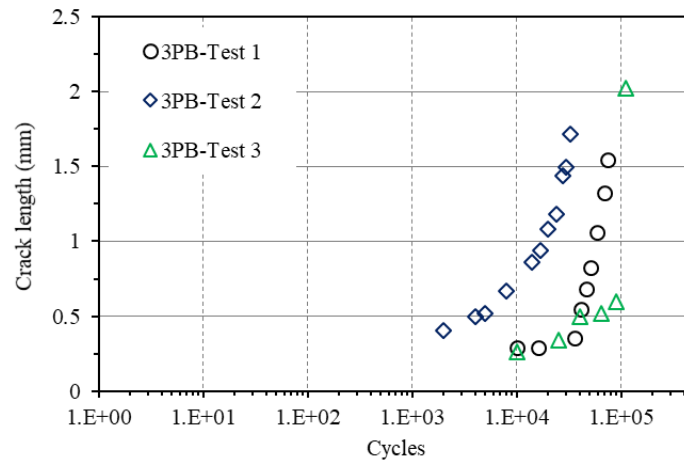


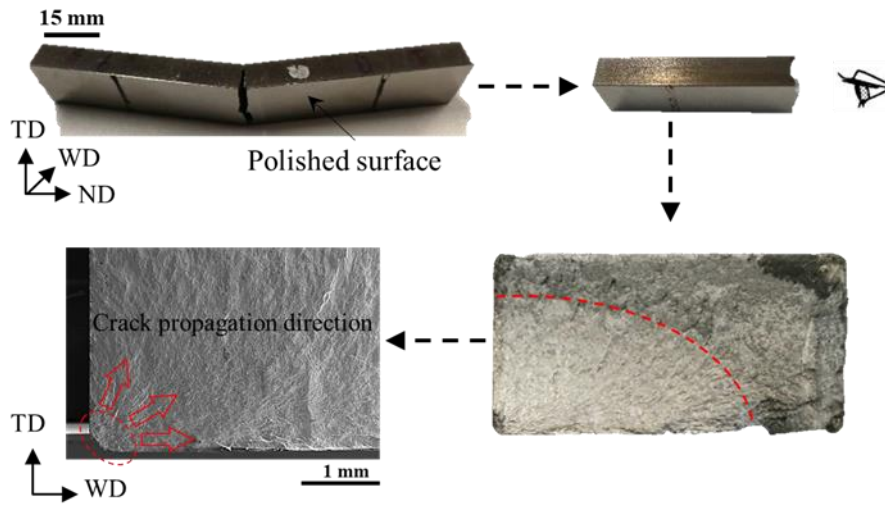
Figure 5.10: Crack growth history of the lead crack measured with the travelling microscope. 3PB-Test 1 ($\sigma_{\max}=380$ MPa, $N_f = 74,000$) 3PB-Test 2 ($\sigma_{\max}=380$ MPa, $N_f = 33,000$) and 3PB-Test 3 ($\sigma_{\max}=380$ MPa, $N_f = 110,000$)

5.3.3 Fracture mechanism

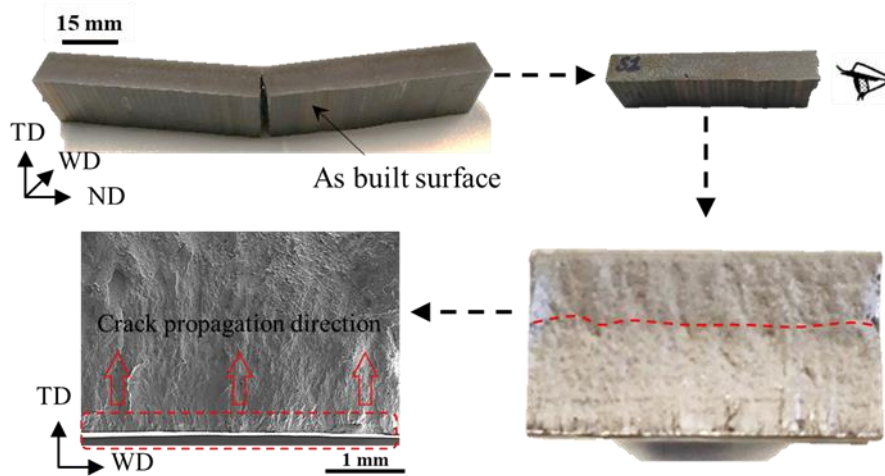
To understand the failure mechanism, fracture surface analysis was carried out and is presented in Figure 5.11. The fracture surface analysis was carried out on the TD-WD plane. Both sample sets had crack initiation from the surface; however, in all the machined samples, the crack initiated from a single point at the corner of the sample, which propagated in the form of a quarter-elliptical shape (Figure 5.11a).

In the as-deposited samples, crack initiated from a single “groove” at the centre of the beam specimen where the bending stress was the highest. Because the groove was extending through the sample’s width (Figure 5.1), the crack growth profile was like a rectangular shape (Figure 5.11b). For samples with as-deposited surface waviness, higher magnification SEM images are used to study the fracture mechanism, and one of these is presented in Figure 5.12. The fracture surfaces of an as-deposited sample can be divided into two distinct regions. Region I is the slower crack growth region showing the classic fracture facets that are formed due to the cyclic slip process of the α colonies. In Region II, dimples manifest the fast fracture process where crack grows as a mixed-mode (intergranular and transgranular) rather than transgranular mode. Identification of these

regions is important for predicting fatigue life based on fracture mechanics as it separates the slow and stable crack growth region from the final fast fracture region.



(a) Polished surface



(b) As-built surface

Figure 5.11: Fracture surfaces for (a) polished samples tested at 800 MPa with $N_f = 74,813$ (b) as-deposited surface, with arrows showing the crack growth direction tested at 500 MPa with $N_f = 25,575$

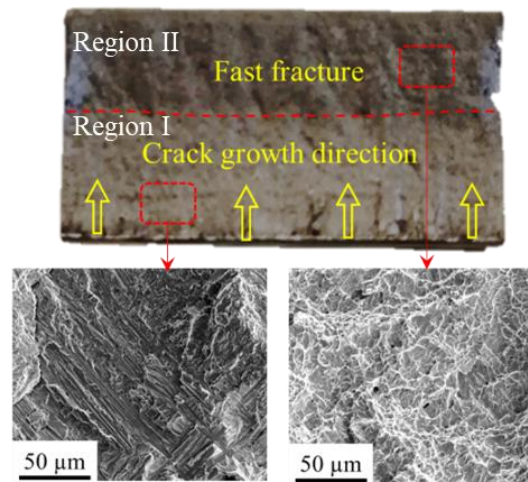


Figure 5.12: Fracture surfaces showing different fracture regions in as-deposited sample tested at 500 MPa with $N_f = 25,575$.

5.4 Summary

Two sets of test samples, i.e. machined and as-deposited surfaces, of wire+arc additive manufactured titanium alloy Ti-6Al-4V (WAAM Ti64) have been tested in a three-point bend fatigue load to evaluate the fatigue life reduction in the as-deposited condition. Key findings can be summarised as follows:

Values of commonly used parameters for surface roughness quantification, R_a , R_y and R_z , were measured for the as-deposited surface as $26.8 \pm 2.8 \mu\text{m}$, $245 \pm 28.9 \mu\text{m}$ and $152 \pm 14.6 \mu\text{m}$, respectively. The grooves were in sub-millimetre size extending through the width of the samples, unlike surface features of other AM processes such as SLM and EBM.

Fatigue strength measured from the $S-N$ data of bending tests has been reduced by a factor of approximately two comparing with samples with machined and polished surfaces.

Microstructural analysis has shown coarse columnar primary β grains growing along the layer build direction aligning in the material's build direction. This columnar growth was the result of a steep thermal gradient at the solidification front. Furthermore, classical α

+ β microstructures with basketweave morphologies have been observed with an average α lath width of 1.5 μm .

In the presence of prior β grain boundaries, the crack branching has been observed, which has slowed down the crack growth rate.

Fracture surface analysis has revealed that polished samples has crack initiation at a single point, at a corner, and propagated as a quarter-elliptical crack, whereas samples with the as-deposited surface the crack has initiated from a single groove at the centre of sample length span and the crack propagation profile was a “rectangular” shape with the length being the sample’s width. Further analysis of fracture surface has revealed that the faceted fracture feature during the early stage of crack growth which is a classic manifestation of slips in the α colonies with respect to their orientation to the loading direction and dimples in the region of final fast fracture.

Chapter 6

Durability of as-deposited WAAM Ti-6Al-4V: Modelling

6.1 Introduction

This is a follow-up Chapter to Chapter 5, where experimental results of the as-deposited samples have been reported. This Chapter summarizes the modelling side of the work on the same specimen configuration. While the arithmetic means value, R_a , is commonly used to present the magnitude of the surface roughness, for bending fatigue test, it is not a suitable parameter to describe the stress concentration at the crack initiation site, which is in the centre of the bending sample. Two approaches have been adopted to predict the fatigue life, i.e., the notch-stress approach and the fracture mechanics approach using the surface notch size as an equivalent initial flaw size (EIFS). FE models were used to calculate the local stress in the case of the notch-stress approach, while the stress intensity factor was calculated as the crack driving force in the fracture mechanics approach.

6.2 Notch-stress approach

6.2.1 Stress concentration factor of a typical notch in as-deposited surface

In bending fatigue tests, all the samples with as-deposited surface showed crack initiation at the centre of the sample as shown in Figure 5.7., where they experienced the maximum tensile stress. After sample failure, the crack initiation notch is identified and traced using the recorded surface roughness scans before testing. This has enabled the determination of the radius of curvature r , depth d and angle θ of the crack initiation notch in all the as-deposited samples (the complete data set of these values is given in Appendix). As

mentioned in [127], the three parameters r , d and θ of the notch dictate the stress concentration factor value for the notch in a three-point bend setup. So, these values were extracted for each sample, and further studies on the identification of stress concentration factors were performed. The notch depth, d varies between $50\ \mu\text{m}$ to $320\ \mu\text{m}$, the angle θ is between 167° to 175° and the radius of curvature, r ranges between $90\ \mu\text{m}$ to $200\ \mu\text{m}$.

However, it was further observed that if the ratio of r and t is less than 0.03 ($r/t < 0.03$), and $t/(t-d)$ is less than 1.05 ($t/(t-d) < 1.05$), the θ dominates the stress concentration factor, K_t , of the notch [127] (Appendix 1.2). A similar observation was made in this research where the increase in θ (keeping r/t and $t/(t-d)$ constant) decreased K_t until it reaches 180° , where it is equal to 1 (Figure 6.1).

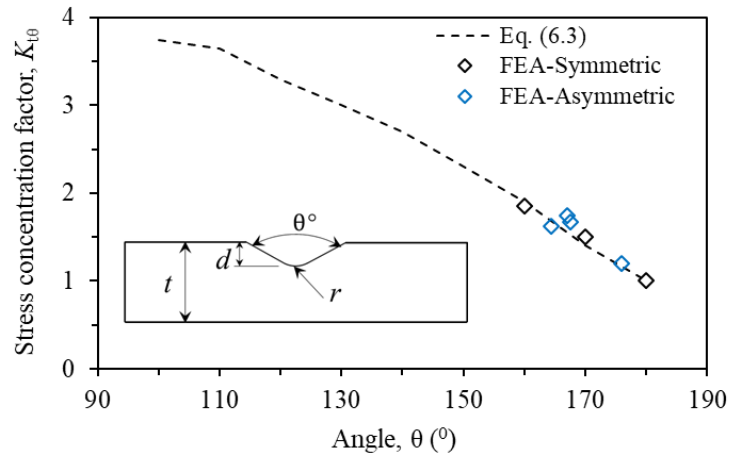


Figure 6.1: Effect of notch mouth angle on stress concentration factor keeping r and d constant.

The surface roughness measurement data was then used to determine the K_t values using the finite element analysis (FEA). The theoretical formula presented in [21] took into account the radius of curvature and depth of the profile. Hence, the values of r , d and θ obtained from FT were used to create a 2D model to identify the K_t .

First, the FE model was verified by the analytical solution of ideal V-shaped surface notches under bending load given in [127]. The K_t was calculated using eq. (6.1) [127].

$$K_t = \frac{\sigma_{\max}}{S_{\max}} \quad (6.1)$$

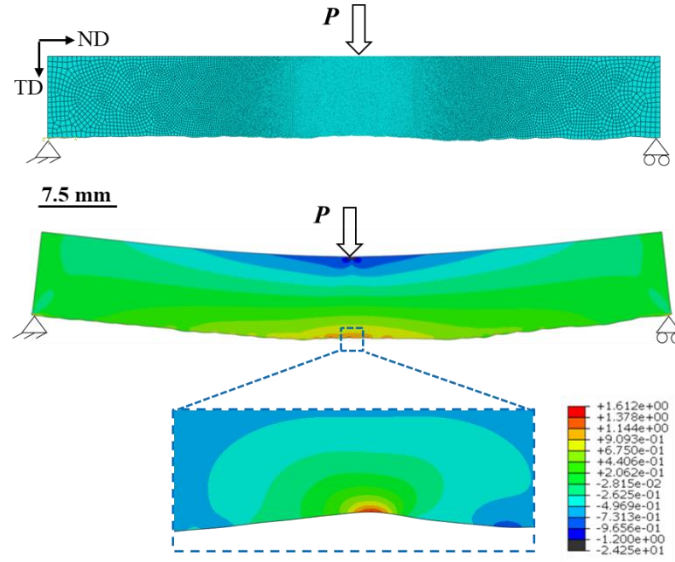
where σ_{\max} is the maximum stress at the V-shaped notch root and S_{\max} is maximum applied bending stress at the outer face of the beam sample. However, if the notch has an angle θ such that, $90^\circ < \theta \leq 180^\circ$, then the K_t will be defined as $K_{t\theta}$ and is calculated by eq. (6.2) [127].

$$K_{t\theta} = 1.11K_t \left[-0.0159 + 0.2243 \left(\frac{\theta}{150} \right) - 0.4293 \left(\frac{\theta}{150} \right)^2 + 0.3609 \left(\frac{\theta}{150} \right)^3 \right] K_t^2 \quad (6.2)$$

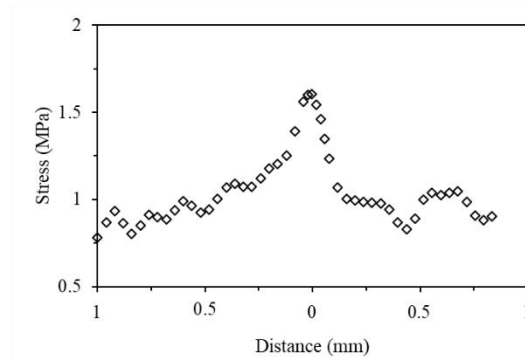
For each as-deposited sample, the $K_{t\theta}$ was calculated using the procedure stated above and found that the $K_{t\theta}$ for a typical notch in the as-deposited surface were between 1.2-1.75 (Figure 6.1).

Later, the as-deposited surface profile from metrology data was imported into ABAQUS using the data points from FT, and the value of $K_{t\theta}$ was identified. It was observed that due to the asymmetric nature of the notch, the difference between the ideal V-notch and actual notch was up to ~7%. Nevertheless, the $K_{t\theta}$ value is still dependent on the θ angle (Figure 6.1). To reduce the computational time, the 60,000 data points obtained from FT in a single scan were reduced to 6000 by removing intermediate points without affecting the $K_{t\theta}$ values. The data points were converted into splines which were then converted to 2D geometry models using the software package CATIA V5. The profile was then used as a surface model to generate the finite element geometry in ABAQUS. A linear elastic material model was considered with the plane strain condition. An element size of 0.02 mm was taken near the notch root, which gradually increased in size to 0.5 mm away from the notch. The element size was selected after mesh sensitivity analysis for solution convergence. The load and boundary conditions applied are shown in Figure 6.2a. The maximum notch root stress in the ND-direction was obtained and was divided by the

applied bending stress to give the $K_{t\theta}$ value at the centre of the specimen. From Figure 6.2b, it can be seen that the centre notch gave the highest value of $K_{t\theta}$.



(a)



(b)

Figure 6.2: (a) Finite element model for the sample tested in 3PB fatigue and zoom-in view of a single notch imported from FT data, (b) stress distribution along the notch area (where the notch is corresponding to “distance” =1 mm, applied bending stress = 1 MPa)

6.2.2 Fatigue life prediction

For fatigue life prediction of as-deposited WAAM Ti64, the following assumptions have been made:

- a) The as-deposited surface waviness can be considered a notch as they act as stress raisers, and these stress raisers control the fatigue life.
- b) The predicted life of as-deposited samples by the notch stress approach represents the crack initiation life. The subsequent crack propagation life is ignored for the small laboratory samples.

To predict the fatigue life, the applied stress, S_{\max} , was reduced by a factor of $K_{t\theta}$ of either its minimum value of 1.2 or maximum value of 1.75. The grey band in Figure 6.3 shows the predicted range of as-deposited WAAM samples considering the minimum and maximum values of $K_{t\theta}$. The fatigue life predicted by the model corresponds well with the experimental data, as shown in Figure 6.3. However, at lower stresses, i.e., below 400 MPa, the over-estimation can be observed and may be justified due to coarse α -lath microstructure, which would reduce the crack initiation life. The effect of microstructure and crystallographic orientation on fatigue data scatter is discussed in Chapter 7.

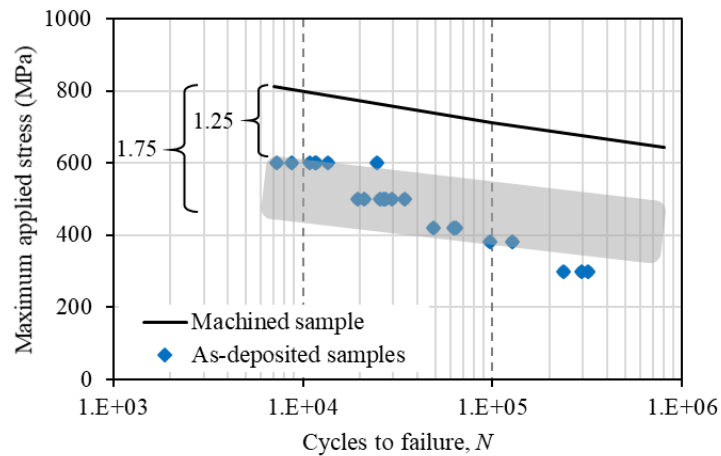


Figure 6.3: S - N relation of fatigue life prediction based on K_t and experimental data of as-deposited and polished WAAM Ti64.

Fatigue reduction by a factor of up to four has been reported in the literature [18] for SLM and EBM as-deposited condition due to the stress concentration factor at the notch root of the as-deposited samples. Persenot et al. [21] suggested that notch like defects can be

treated as elliptical notches, and K_t can be calculated using the depth of the profile and radius of the curvature of the notch.

However, it does not apply to WAAM as-deposited samples as it has been demonstrated that the opening angle θ of the notch is also relevant in calculating the stress concentration factor $K_{t\theta}$.

6.3 Fracture mechanics approach

Equations for calculating the stress intensity factor, K for a beam under three-point bending load, can be found in [192,193]. Solutions provided by these references are comparable with each other. Nevertheless, to see the effect of the as-deposited notch on K , the FE modelling was performed and compared. Furthermore, the fracture mechanics approach based on a unified crack growth law was applied for the durability analysis treating the notch depth as a crack, and the crack growth driving force, K was used as the governing parameter for fatigue life prediction

6.3.1 Calculation of stress intensity factor by FEM

Investigation of a single edge notch bending SEN(B) was done relative to the benchmark solution presented in [192,193]. The ABAQUS was used for FE analysis for both pre and post-processing in this section as well. The SEN(B) samples were modelled as two-dimensional beams. A schematic of the two-dimensional model is shown in Figure 6.4. The width of the sample was taken to be 8 mm. Fracture surface analysis of as-deposited samples show no significant variation of the crack front across the width of the sample (refer to Figure 5.12). Therefore, it is reasonable to assume a uniform crack front and analyse the crack propagation problem with 2D plane strain elements (CPE4R). The benchmark sample is considered symmetrical about the crack depth, so the symmetrical boundary condition was applied with half the geometry modelled having 30 mm span length (Figure 6.4). The applied load was $P/2$ and applied on the top surface as a point load. The applied stress was calculated to be 380 MPa at the outer surface of the beam using eq. (5.5). It was deemed unnecessary to model all the notches as it has been

demonstrated in the previous section that the middle notches were the only stress concentration areas, and almost all the samples failed in the middle of the sample. The actual profile was then modelled with an initial notch depth of $50\ \mu\text{m}$ and a crack length of $100\ \mu\text{m}$, as shown in Figure 6.4b. The element size at the crack front was $6\ \mu\text{m}$ which was progressively increased to $500\ \mu\text{m}$ for both models and was selected after mesh convergence study (with an accepted margin of error, $< 3\%$) (Figure 6.5). Linear elastic material properties were used for this analysis as well, and the displacement extrapolation method was adopted for calculating K ahead of the crack tip.

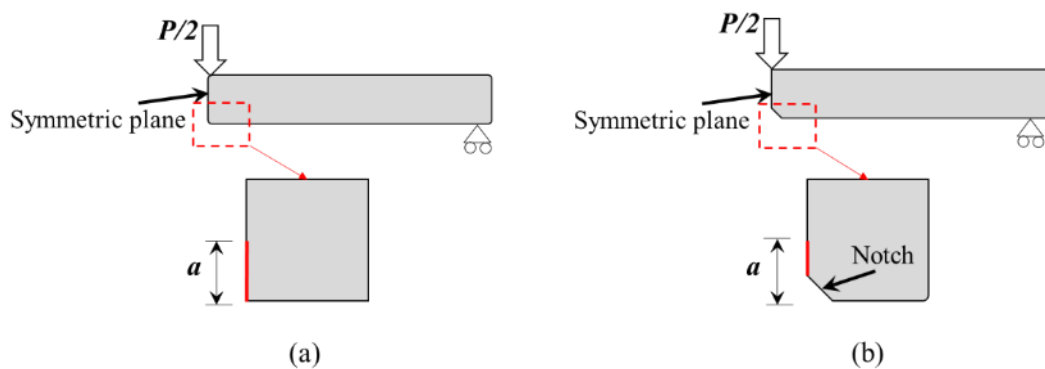


Figure 6.4: The FE model of an SEN(B) geometry: (a) a line crack as in standard SEN(B) geometry and in reference [192], (b) notch+crack (where the notch mimics the surface roughness “dent”), (c) FE mesh used to model notch+crack.

The modelling results show that the K values of the two models (crack only and notch+crack) are very close, with a difference of less than 2%, Figure 6.5. Hence, an assumption was made that the notch was treated as a part of the line crack.

Figure 6.5 shows that the difference between the K values calculated using the FE model and Figure 6.6 shows the comparison of FE model with calculated K at three different crack lengths. The difference between the analytical solutions and FE analysis was less than 3%. Therefore, eq. (6.3) from [192] was used further in this study.

$$K = \frac{PL}{Wt^{3/2}} \left[2.9 \left(\frac{a}{t}\right)^{1/2} - 4.6 \left(\frac{a}{t}\right)^{3/2} + 21.8 \left(\frac{a}{t}\right)^{5/2} - 37.6 \left(\frac{a}{t}\right)^{7/2} + 38.7 \left(\frac{a}{t}\right)^{9/2} \right] \quad (6.3)$$

where P is applied load, L the distance between the rollers, W the width of the sample, t the thickness of the sample, and a the crack length in TD direction.

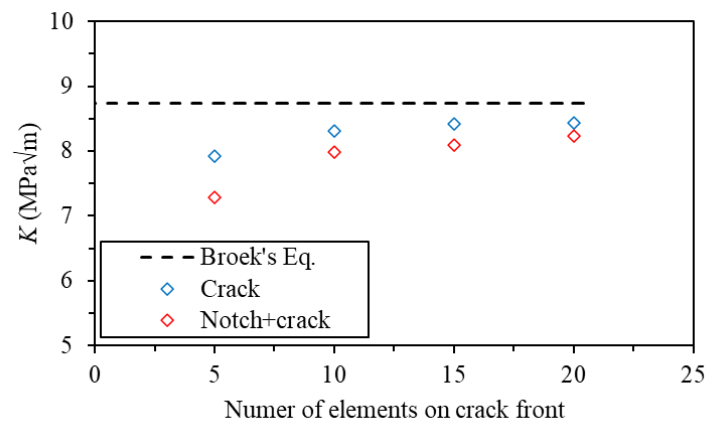


Figure 6.5: Stress intensity factor vs. crack length in 3PB sample, compared with [192].

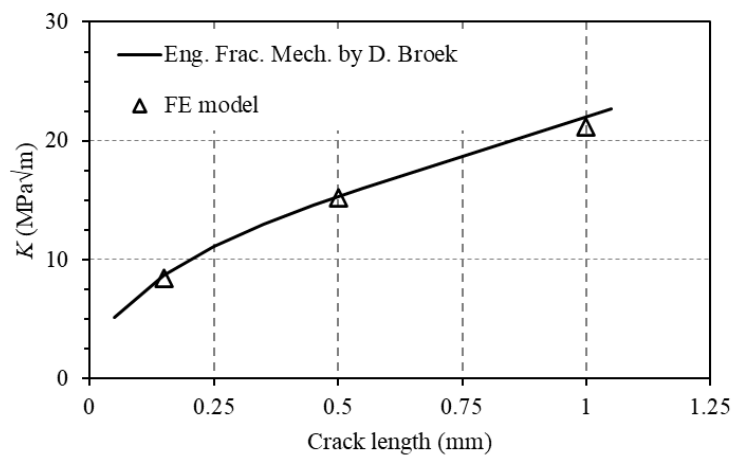


Figure 6.6: Calculated K as a function of crack length for 3PB samples

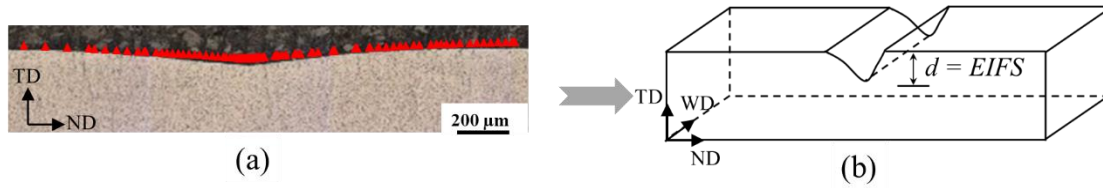


Figure 6.7: Schematic representation of as-deposited notch.

To predict the durability of the as-deposited surface, the depth of the profile, d , is considered equivalent initial flaw size (EIFS), as shown in Figure 6.7, and used as initial crack. Out of 24 samples tested in as-deposited condition, three cases for EIFS were considered, i.e., the deepest, shallowest and average and are equal to 0.32 mm, 0.05 mm, and 0.13 mm, respectively. To calculate the fatigue life, crack propagation can be artificially divided into many integration segments. When the integration segments are sufficiently small, the crack growth rate is assumed to be constant in those intervals. The fatigue life was calculated using the variant of the Hartman-Schijve equation (Chapter 3, eq. (3.22)), where material constants calculated in Chapter 4 for unified crack growth law were used. The material constant used for the calculation of fatigue life was $D = 1 \times 10^{-10}$ and $p = 2.5$. The fatigue life for a given crack length was then calculated by integration of crack growth rates. The prediction method followed an iterative scheme, starting from the initial crack size, the EIFS, up to the final critical crack length. The final critical crack length was identified from a fracture surface presented in Figure 5.12 and estimated to be 4 mm, which was approx. 50% of the sample thickness. The prediction results were then compared with experimental results for validation and are presented in the following section.

6.3.2 Fatigue life prediction

The fatigue life was calculated by numerical integration of eq. (3.22) using material constants given in Chapter 4. Figure 6.8 shows the comparison of prediction with test measurement. Two EIFS values were used as the initial crack length, 0.05 and 0.32 mm, for specimens tested at 380 MPa (3PB-Test 1, 3PB-Test 2) and EIFS = 0.13 mm for the third specimen tested at 300 MPa (3PB-Test 3). The experimental test result shows that specimen 3PB-Test 2 failed earlier than 3PB-Test 1 at the same applied stress. The

predicted fatigue life range based on the shallowest and deepest notch sizes (0.05 and 0.32 mm) covered the experimental test data range and can be regarded as a good prediction.

$$\frac{da}{dN} = D \left(\frac{\Delta K - \Delta K_{thr}}{\sqrt{1 - K_{max}/A}} \right)^P \quad (3.22)$$

Figure 6.9 shows the prediction of the *S-N* curve. Considering the experimental scatter, the prediction based on the deepest and shallowest notch falls close to the experimental results.

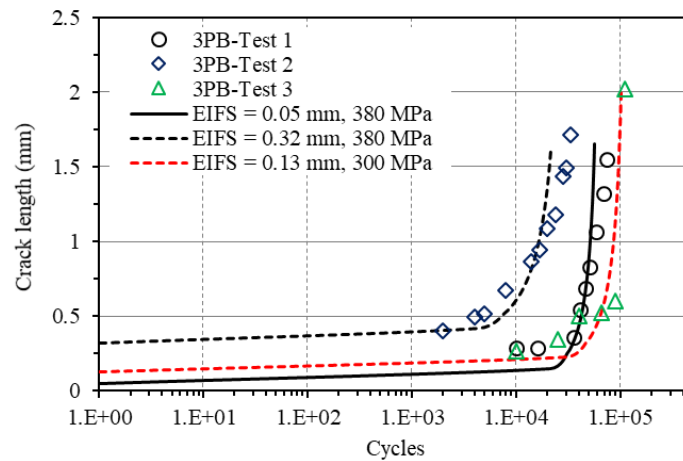


Figure 6.8: Predicted fatigue life for a WAAM Ti64 bending specimen in its as-deposited condition based on a small crack growth approach. 3PB-Test 1 ($\sigma_{max}=380$ MPa, $N_f = 74,000$) 3PB-Test 2 ($\sigma_{max}=380$ MPa, $N_f = 33,000$) and 3PB-Test 3 ($\sigma_{max}=380$ MPa, $N_f = 110,000$)

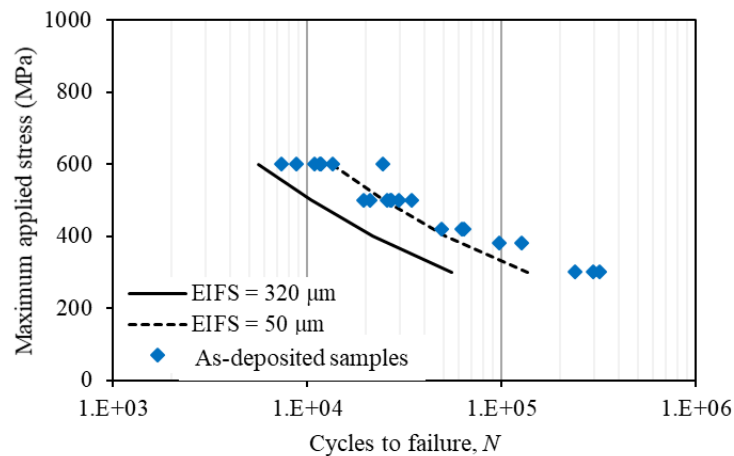


Figure 6.9: S - N curve showing experimental data of as-deposited WAAM Ti64 and durability prediction based on the modified Hartman-Schijve equation.

There are two different approaches for durability analysis of parts with defects: (i) Total life is based on crack initiation, (ii) based on LEFM; in the second approach, the initial flaw is considered a crack and durability analysis based on a unified crack growth law for both the small and long crack regions.

In this current study, both approaches seem to be working well for the as-deposited WAAM Ti64 laboratory samples. The reasonable fatigue life prediction based on notch-stress can be explained based on the fact that the sample thickness was small, about 8 mm, and there was no considerable crack growth stage after the crack had initiated, and the total life was dominated by the crack initiation life. The stress concentration factor of 1.2-1.75 was mild and local stresses at the notch hardly reached the material's yield strength (under the current testing of applied stress 600 MPa). Hence, the fatigue life reduction factor was approximately the same as the stress concentration factor. However, employing an advanced approach of LEFM coupled with EIFS, a reasonable good prediction was achieved with a slight conservative prediction at the lower applied stresses. This approach is more suitable for larger structures as it treats the defect as an initial crack, and crack growth life is predicted by the fracture mechanics approach.

6.4 Summary

In addition to the surface roughness parameters (R_a , R_y and R_z), as-deposited surface waviness is treated as small notches that are characterised by the notch depth (d), notch mouth angle (θ) and notch base curvature radius (r). To obtain realistic values of these parameters, resolution for different metrology techniques are compared. It has been observed that form tracer (FT) with 4 μm stylus diameter and optical microscopy (OM) has approximately the same resolution. However, due to the OM technique's destructive nature, FT is the most suitable technique to characterise WAAM as-deposited waviness.

The asymmetric nature of the notch created using metrology data affected the stress concentration factor slightly. Nevertheless, if the ratio of r and t is less than 0.03 ($r/t < 0.03$), and $t/(t-d)$ is less than 1.05 ($t/(t-d) < 1.05$), the θ dominates the stress concentration factor value. Hence, the analytical solution given by Peterson's can be used to calculate the stress concentration factor of as-deposited WAAM surface.

For fatigue life prediction based on the notch fatigue approach, the waviness is treated as a "notch", which acts as a stress raiser and controls the fatigue life. The crack propagation life was ignored, and fatigue life was estimated by a reduction factor of 1.25 to 1.75, which is the typical value range of the $K_{t\theta}$ for the WAAM Ti64 as-deposited surface waviness. The fatigue life based on the notch fatigue approach correlated well with the experimental data except at lower stresses where the fatigue life is over-estimated.

For the fracture mechanics approach, the notch depth is used as the equivalent initial flaw size (EIFS) or initial crack size, which are in the sub-millimetre length range. The durability of the specimens can be predicted using the modified Hartman-Schijve equation with EIFS as the initial crack length. The fracture mechanics approach is a preferred technique to predict fatigue life as it includes the crack length and can be used for larger structures.

Chapter 7

Effect of microstructure and crystallographic orientation on fatigue life scatter

7.1 Introduction

Fatigue performance of AM parts suffers from defects, process-dependent microstructure and strong crystallographic texture of grains [45]. The presence of defects in the as-deposited AM parts cause stress concentration, and as a result, early crack initiation may occur, resulting in poor fatigue performance [194,195]. Additionally, a large scatter of fatigue life values was reported both in WAAM Ti64 [12,13] and also in other AM processed Ti64 [194], which is the direct consequence of the presence of the defects in the as-deposited material.

During this PhD, some additional work was performed on the effect of internal defects on fatigue life of WAAM Ti64. In the project, multi-stage modelling was used to import the XCT data and geometry was created for ABAQUS to be used for K_t analysis of the actual defect found in WAAM Ti64. The findings of the research are presented in [72]. It was further observed that life prediction models based solely on the continuum mechanics could not explain the scatter found in the results presented in [13,29] and in the current study because the fatigue properties are controlled by defects and the microstructure [12,13,71–73,196]. Although this is a standalone Chapter where a different type of defect is being analysed, nevertheless, work in this Chapter relates to the understanding of the crack initiation from defects and early crack propagation with different surrounding microstructure and crystallographic texture and their contribution towards the scatter in $S-N$ data. Therefore this is a coherent part of this thesis, and the contents of this Chapter have been published in the literature [14].

7.2 Materials and experimental methods

The experimental material was produced by the previously optimised WAAM process [13] using a 1.2 mm diameter grade 5 Ti64 wire. An oscillation build strategy was used to build a 27 mm thick WAAM Ti64 wall. A schematic of the oscillation build strategy is presented in Figure 7.1a. A further detailed description of the build process, deposition parameters, and Ti64 wire composition can be found in [13]. X-ray computed tomography (X-ray CT) was used to measure the density and average porosity size of the fatigue test samples [72]. The measurements were performed at an accelerating voltage of 120 kV and a current of 58 μ A. The effective pixel size was 10 μ m that enabled detecting defects greater than 20 μ m per spatial dimension. A total of 1583 projections were recorded with an exposure time of 500 ms and at a rotation step size of 0.22°. The porosity measurement revealed that the samples had a density of 99.99%, with porosity size ranging between 40 - 220 μ m [72].

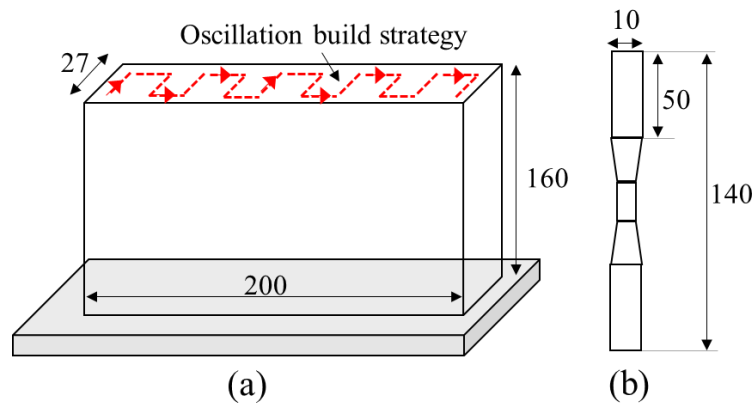


Figure 7.1: Schematic illustration of (a) WAAM Ti64 wall, (b) geometry and dimensions of a fatigue sample (unit: mm, not to scale). Build direction was along with the ND, and torch movement was oscillated along with the TD for each layer.

After the samples' failure, the fracture surfaces were analysed using Scanning Electron Microscopy (SEM) with an operating voltage of 10 kV. For the EBSD measurements, samples were extracted on the ND-WD plane. The crack initiating defect was identified from the fracture surface analysis, as presented in Figure 7.2a. One half of the

corresponding fractured sample was used to extract the sample for electron backscattered diffraction (EBSD) analysis; a schematic representation of the sample extraction plan is shown in Figure 7.2b. The sample was cut perpendicular to the TD-WD plane close to the crack initiation defect using a high precision cutting machine (Figure 7.2c). The cut section was then periodically ground, polished and observed under an optical microscope until the crack initiation site was exposed for the EBSD analysis, Figure 7.2c. Final polishing was carried out with 0.02 μm size colloidal silica. The area at and around the crack initiating defect was selected for EBSD measurements (highlighted in Figure 7.2c). The EBSD measurements were carried out using a step size of 0.5 μm and at an operating voltage of 20 kV. Oxford Instruments Aztec HKL and Channel 5 imaging and post-processing software suites were employed for EBSD data analysis. The Schmid factor distribution was calculated along with three different slip systems, i.e. the prismatic, basal and first-order pyramidal. The slip planes and slip directions active in Ti hexagonal crystal lattice are presented in Table 7.1. For the EBSD measurements, the sample was tilted at 70° , and the coordinate system was defined as $\phi = 0^\circ$, $\phi_1 = -90^\circ$ and $\phi_2 = 0^\circ$ in the HKL software. To calculate the Schmid factor along the build direction, the loading direction (parallel to *ND* in Figure 7.2c) was defined as a 'rolling direction'. The output was obtained in colour contour maps from where the frequency distribution of each plane was extracted and presented below. Based on the evidence from our previous [72] study, the presence of porosity defects did not cause non-uniform stress distribution. This is mainly due to the regular spherical shape of the porosity. Therefore, when considering the Schmid factor distribution within the stress field at the crack initiation area, we can broadly approximate the Schmid factor generated by HKL software similar to the tensile load of a smooth high cycle fatigue sample.

Table 7.1: Slip directions and slip planes in Ti64, used for Schmid factor calculation.

Slip systems	Slip plane	Slip direction
Prismatic<a>	$\{10\bar{1}0\}$	$\langle \bar{1}2\bar{1}0 \rangle$
Basal<a>	$\{0002\}$	$\langle 2\bar{1}\bar{1}0 \rangle$
1 st order	$\{1\bar{1}01\}$	$\langle 1\bar{2}1\bar{3} \rangle$
Pyramidal<c+a>		

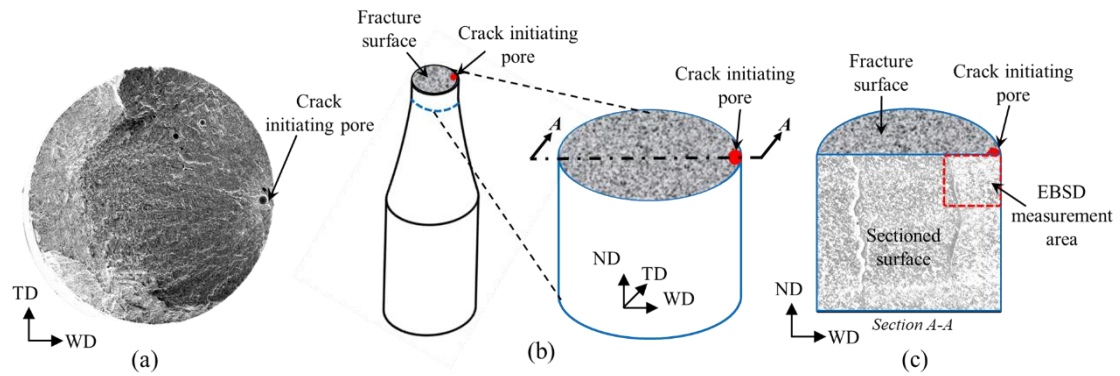
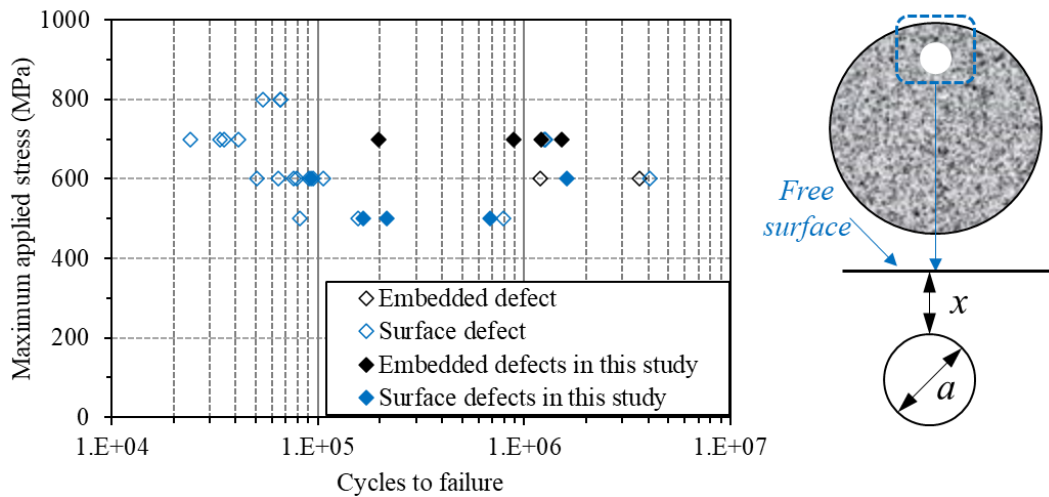


Figure 7.2: (a) Example of a fracture surface showing the crack initiating defect, (b) schematic of a fractured sample showing sample extraction for EBSD analysis, (c) sample for EBSD analysis showing sectioned micrograph on the TD-WD plane and location of EBSD measurement area around crack initiating defect.

7.3 Results and discussions

7.3.1 Fatigue life and fractography



of defect location and definition of distance to sample surface. Surface defects, if the $x/d < 0.8$ and embedded defects, $x/d > 0.8$.

Fatigue test results from [13] are presented in Figure 7.3a. A large scatter can be observed in samples tested at the same applied stress. To understand the fatigue life scatter, the geometrical characteristics of the internal defects, i.e., the size and location of crack initiating defects, were analysed through fracture surfaces analysis using SEM on all the selected samples at three stress levels. These selected samples are those with solid symbols in Figure 7.3a. Fracture surface study confirmed that the crack always initiated from a defect, and the crack initiating defect size varied between 47 μm to 230 μm . However, a poor correlation was found between fatigue life and the crack initiating defect size (Table 7.2). Crack initiation from defects and heterogeneous microstructure in WAAM Ti64 might have influenced the crack initiation life, thereby overall scatter in fatigue life. Therefore, along with the crack initiation geometrical characteristics, a detailed study on the crystallographic orientation of α and the average α lath width around the crack initiating defect was carried out for the selected samples in Figure 7.3a.

Table 7.2: Fatigue life of samples with the defect details that led to crack initiation

Maximum applied stress (MPa)	700				600		500		
Sample label	S1	S2	S3	S4	S5	S6	S7	S8	S9
Fatigue life ($\times 10^4$)	152	89	20	121	9	160	22	69	17
Defect diameter (μm)	47	59	106	229	91	100	125	126	192
Defect distance to the free surface (μm)	1900	600	670	500	Surface defect				

In the previous study [72], it has been demonstrated through finite element modelling that the location of defect influenced the stress concentration. When the ratio of defect distance from the free surface (x) to the defect diameter (d) was greater than 0.8, the interaction between the free surface and defect was negligible and had no influence on the stress concentration factor. Based on this study the defect sizes and their locations were categorised into two classes; (i) embedded defects - if the $x/d > 0.8$, and (ii) surface defects – if the $x/d < 0.8$, Figure 7.3. From the study of the fracture surfaces, it was found that the

cracks were initiated from embedded defects in all samples selected for study at 700 MPa, whereas cracks initiated from surface defects in samples tested at 600 MPa and 500 MPa. To provide a better presentation of the results, samples were labelled based on the size of the crack initiating defect (smallest to largest) at each stress level, i.e. at 700 MPa S1, S2, S3 and S4, at 600 MPa, S5 and S6 and at 500 MPa, S7, S8 and S9 respectively. The results are presented in Table 7.2, which shows the defect size, its distance from the free surface, and the corresponding fatigue life of the sample.

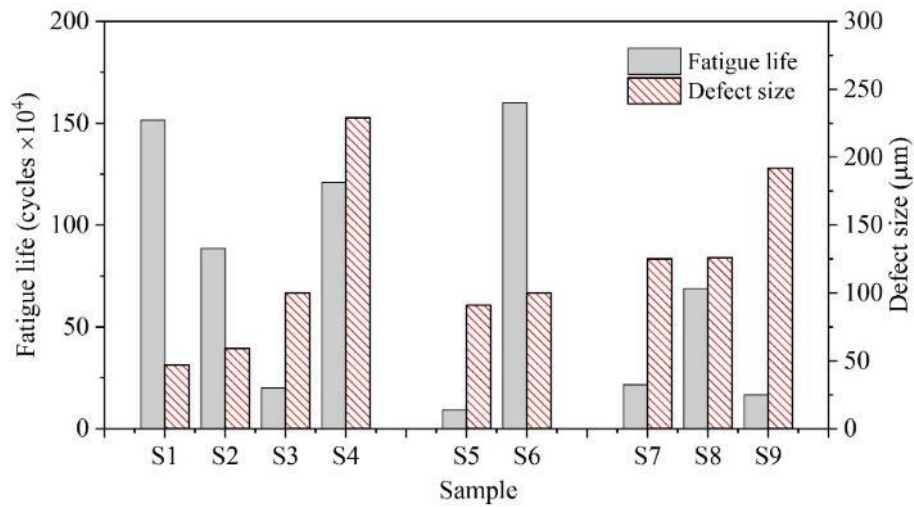


Figure 7.4: Fatigue life and crack initiating defect size for samples under maximum applied stress 700 MPa (S1-S4), 600 MPa (S5, S6) and 500 MPa (S7-S9).

7.3.2 Crack initiation from embedded defects

Figure 7.4 shows fatigue life vs. crack initiating defect size for the selected samples. Irrespective of the crack initiating defect location (i.e. either crack initiation from embedded or surface defect), data presented in Figure 7.4 did not show any correlation between the defect size and the fatigue life. At 700 MPa applied stress, cracks were initiated from an embedded defect of 47 μm , 60 μm , 106 μm and 229 μm diameter in samples S1, S2, S3 and S4, respectively. In the case of S1 and S2, the crack initiated from a similar defect size. However, the fatigue life of S2 is approximately half as compared to S1.

Similarly, the crack initiating defect size of S4 is approximately four times and two times larger than S2 and S3. However, the fatigue life of S4 was found to be approximately 1.5 times and six times longer than S2 and S3, respectively (refer to Figure 7.4). Moreover, the defect in S4 was closer to the free surface compared to S2 and S3. From this observation, it is evident that the defect size and location were not the only factors causing fatigue life scatter. On the other hand, Murakami and Endo [89,197] suggested a fracture mechanics approach where they have considered the projected area of the crack initiating defect to represent an effective crack size for embedded defects. The proposed stress intensity factor range (ΔK) used the \sqrt{area} of the defect instead of a simple crack length a as shown in Eq. (7.1) [89]

$$\Delta K = C \times \Delta\sigma \sqrt{\pi\sqrt{area}} \quad (7.1)$$

where ΔK is the stress intensity factor range, parameter C is 0.65 for surface defects or 0.5 for embedded defects, $\Delta\sigma$ the applied stress range, and \sqrt{area} the square root of the projected area of the defect. From eq. (7.1), it can be noticed that ΔK is directly proportional to the defect size.

Nevertheless, to understand the effect of microstructure (α lath width and α colony size) and the crystallographic orientation at and around the crack initiating defects on the fatigue life scatter, EBSD measurements were performed on all samples.

Fracture surfaces for samples at 700 MPa are presented in Figure 7.5, showing crack initiating defects. The crack initiating defects appeared to be spherical or near-spherical. The EBSD orientation maps for samples at 700 MPa are presented in Figure 7.6 and confirm considerable variations in the crystallographic orientation of α in S1, S2, S3 and S4 samples. Previous studies have demonstrated that crystallographic orientation variation influences slip activity and fatigue life [198,199]. The most common slip systems in Ti64 are basal $\langle a \rangle$, prismatic $\langle a \rangle$ and pyramidal $\langle c+a \rangle$ [34]. In theory, when

a polycrystalline material is plastically deformed under uniaxial loading, a slip will initiate in grains that are favourably orientated and result in micro yielding. Further increase in the deformation would lead to redistribution or transfer of the local stresses from softer grain families to the harder grain families who are not favourably oriented for slip [200].

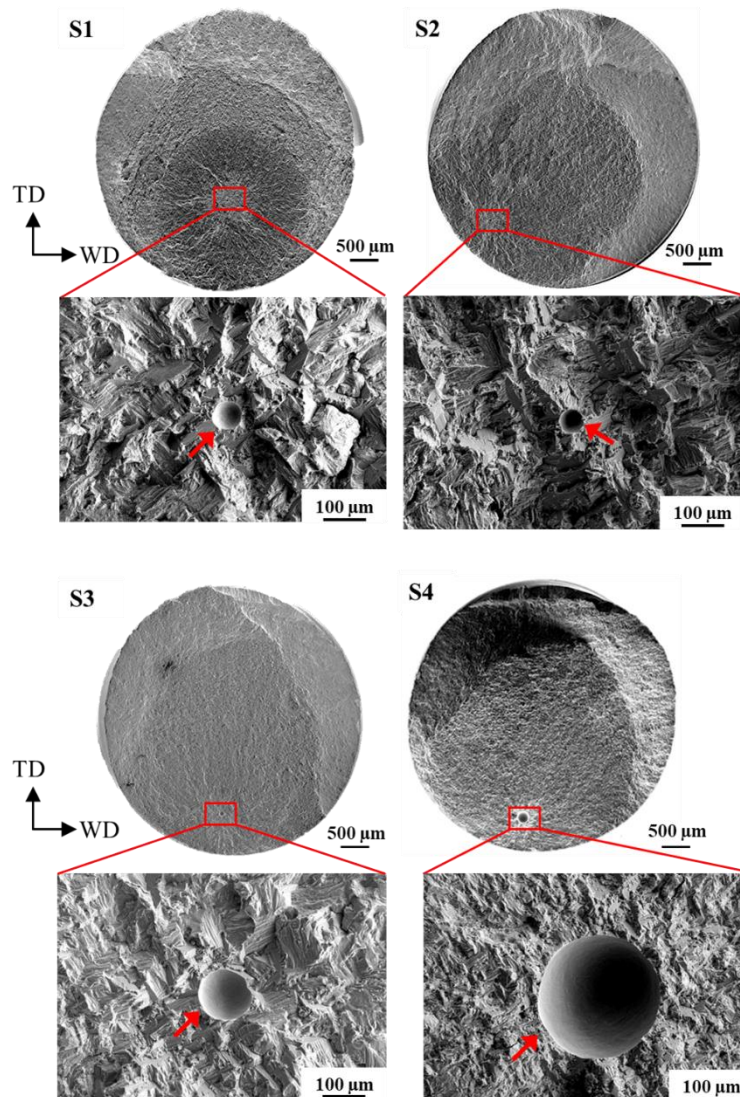


Figure 7.5: SEM images of fracture surfaces showing the embedded defect for the 700 MPa sample group. The crack initiating defect is indicated with an arrow.

To identify the active slip system as a function of grain orientation with respect to the loading direction and the c-axis of a given grain, distribution of the Schmid factor values

for three active slip systems, i.e. $\langle a \rangle$ basal, $\langle a \rangle$ prismatic and $\langle c+a \rangle$ pyramidal, obtained from EBSD analysis were mapped and are presented in Figure 7.6 for comparison. Schmid factor describes the slip plane and the slip direction in a material that can resolve the most shear stress, the higher the Schmid factor, the more likely the respective slip system will be activated [201]. In Figure 7.6, Schmid factor distribution analysis shows that S2 had the highest basal slip Schmid factor, whereas S4 had higher pyramidal slip Schmid factor distribution at the 0.45-0.5 value range. Under the fatigue loading, activation of slip mainly depends on the critical resolved shear stress (CRSS) and the Schmid factor, where CRSS is the shear stress component, resolved in the direction of slip and required for initiating slip. According to [202], CRSS required to initiate slip in Ti64 for the prismatic $\langle a \rangle$ $\langle \bar{1}2\bar{1}0 \rangle \{10\bar{1}0\}$, basal $\langle a \rangle$ $\langle 2\bar{1}\bar{1}0 \rangle \{0002\}$ and pyramidal $\langle c+a \rangle$ $\langle 1\bar{2}1\bar{3} \rangle \{1\bar{1}01\}$ slip systems is 370, 420 and 590 MPa, respectively. If the basal plane is parallel to the loading direction (perpendicular to the c-axis of the grain), prismatic slip system $\langle \bar{1}2\bar{1}0 \rangle \{10\bar{1}0\}$ is dominant, while pyramidal slip system $\langle 1\bar{2}1\bar{3} \rangle \{1\bar{1}01\}$ is dominant when the basal plane is perpendicular to the loading direction. On the other hand, basal slip system $\langle 2\bar{1}\bar{1}0 \rangle \{0002\}$ will become active if the misorientation angle between the loading direction and the basal plane $\langle a \rangle$ is between 10° to 66.7° [203]. Further increase in the misorientation angle from 66.7° to 90° will lead to the prismatic slip system [203].

Based on the above description, despite crack initiated from a smaller defect size, the lower CRSS associated with basal slip in S2 resulted in lower fatigue life than S4. However, when the fatigue results were compared between S2 and S1, a 20% decrease in the defect size in S1 resulted in a 100% increase in the fatigue life compared to S2. Moreover, when S3 was compared with S4, it was observed that the smaller defect has resulted in an approximately 80% decrease in fatigue life. Schmid factor analysis showed negligible pyramidal slip activity at Schmid factor distribution at 0.45-0.5 in S3, which would have initiated the crack early due to the lower CRSS associated with the prismatic slip resulting in lower fatigue life compared to S4. The higher values of the CRSS associated with the pyramidal slip system might have delayed the onset deformation and the crack initiation under cyclic loading. Therefore, higher fatigue life was found in S1 and S4 compared to S2. While in the case of S3, the lower value of the CRSS of the

prismatic slip system initiated an early crack resulting in reduced fatigue life, despite the smaller defect than S4.

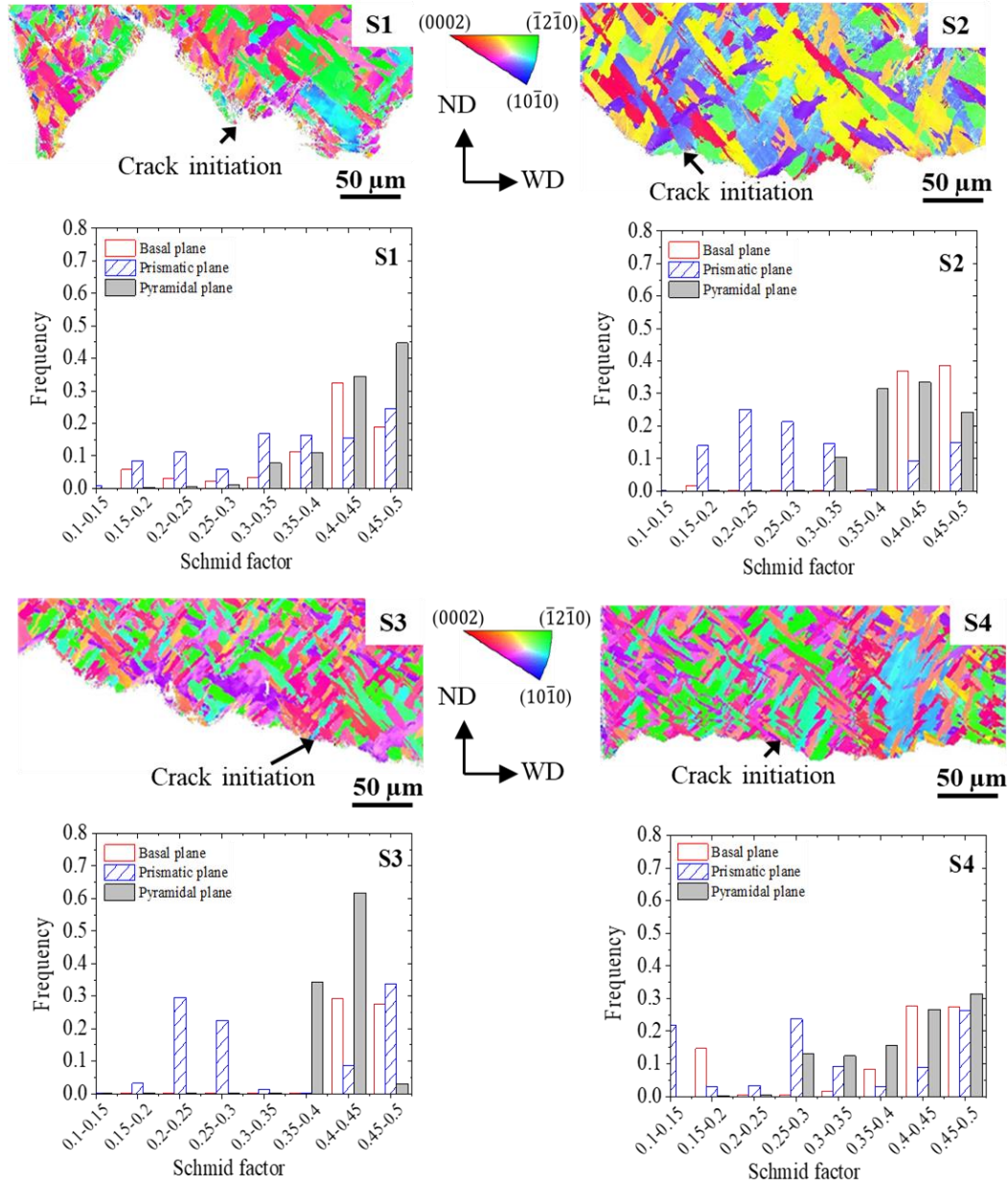


Figure 7.6: EBSD orientation maps of 700 MPa fractured samples showing crack initiation location and Schmid factor distribution analysis. The build and loading directions are parallel to TD. The number of cycles to failure for S1, S2, S3 and S4 are 152×10^4 , 89×10^4 , 20×10^4 and 121×10^4 respectively.

7.3.3 Crack initiation from surface defects

At 600 MPa, S5 and S6 showed crack initiation from similar size defect, but the fatigue life of S5 was only 6% of S6. Similarly, the crack was initiated from a similar defect size in S7, and S8 tested at 500 MPa. However, the fatigue life of S8 was three times higher than S7. On the other hand, despite the crack initiating defect being 1.5 times larger in S9 than S7, they both showed similar fatigue life. This confirms that there is no correlation between the crack initiating defect size and fatigue life.

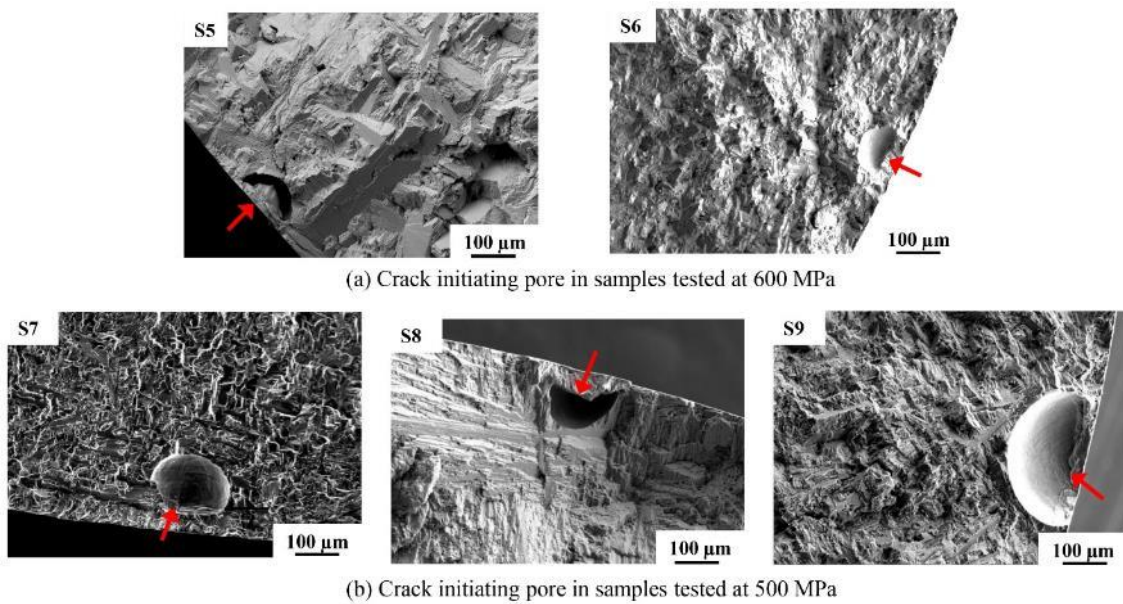


Figure 7.7: SEM images of fracture surfaces showing the crack initiating defect (indicated with an arrow) for samples tested at 600 and 500 MPa.

Figure 7.7 shows SEM images of fracture surfaces of 600 and 500 MPa samples showing crack initiating defects that appeared to be spherical or near-spherical. The EBSD measurements were carried out to investigate the role of crystallographic orientation and grain size distribution on the fatigue life scatter in 600 and 500 MPa samples.

EBSD analysis for S5 and S6 samples tested at 600 MPa are presented in Figure 7.8, along with the distribution of the Schmid factor values calculated for each slip system. Sample S6 showed higher pyramidal slip Schmid factor distribution, whereas S5 had a

higher basal slip Schmid factor distribution. The higher activity of the pyramidal slip system $\langle c+a \rangle \langle \bar{1}\bar{2}1\bar{3} \rangle$ along with the high Schmid factor distribution of the basal and prismatic systems in S6 might have influenced the crack initiation and has resulted in the fracture along different slip systems. In contrast, S5 has higher frequency of the basal $\langle a \rangle \langle 0002 \rangle$ slip system and lower distribution of the pyramidal slip system $\langle c+a \rangle \langle \bar{1}\bar{2}1\bar{3} \rangle$ with values of the Schmid factor between 0.45 – 0.5. Therefore, the crack might have initiated along with the basal slip in S5. Overall, the strong basal slip system active in S5 resulted in a lower fatigue life associated with the lower value of CRSS required to initiate slip. In contrast, higher distribution of pyramidal slip systems in S6 resulted in higher fatigue life than S5.

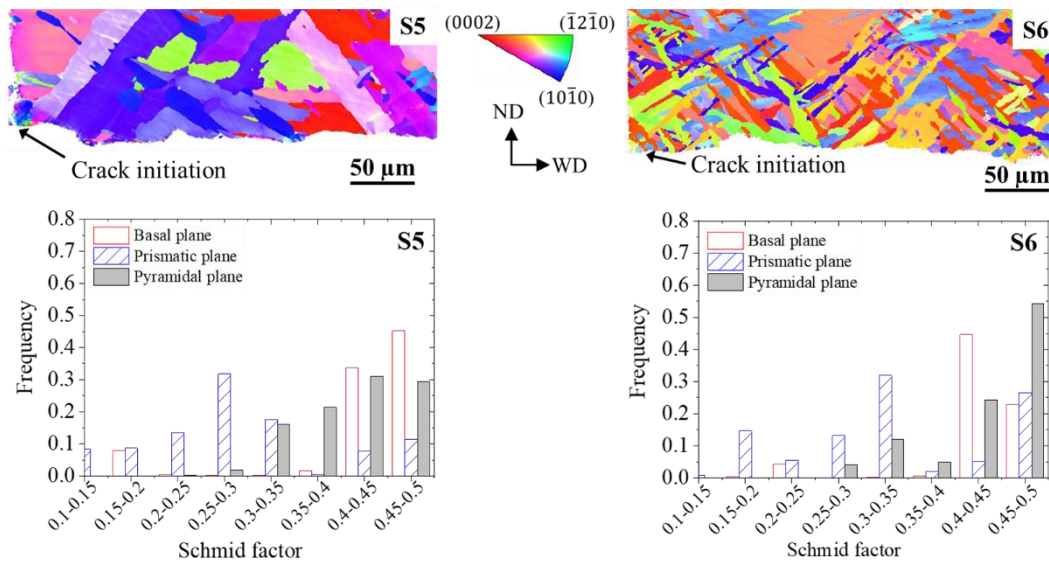


Figure 7.8: EBSD orientation maps of 600 MPa fractured samples showing crack initiation location and Schmid factor distribution analysis in S5 and S6. The build and loading direction is parallel to TD. The number of cycles to failure for S5 and S6 are 9×10^4 , and 160×10^4 respectively.

At 500 MPa, although S7 had higher pyramidal slip system distribution of Schmid factor values between 0.45-0.5 (Figure 7.9), its fatigue life was only 30% of S8. This indicates that the Schmid factor alone could not explain the scatter in the fatigue life of S7 and S8. Therefore, further microstructure analysis was carried out. From the microstructure presented in Chapter 5, it is evident that there was a variation in the local microstructure within the macro zone of the samples. The multiple thermal cycles (melting-

solidification) during WAAM processes directly resulted in complex microstructures varying spatially within the build. This was also confirmed by the EBSD micrographs presented in Figure 7.9.

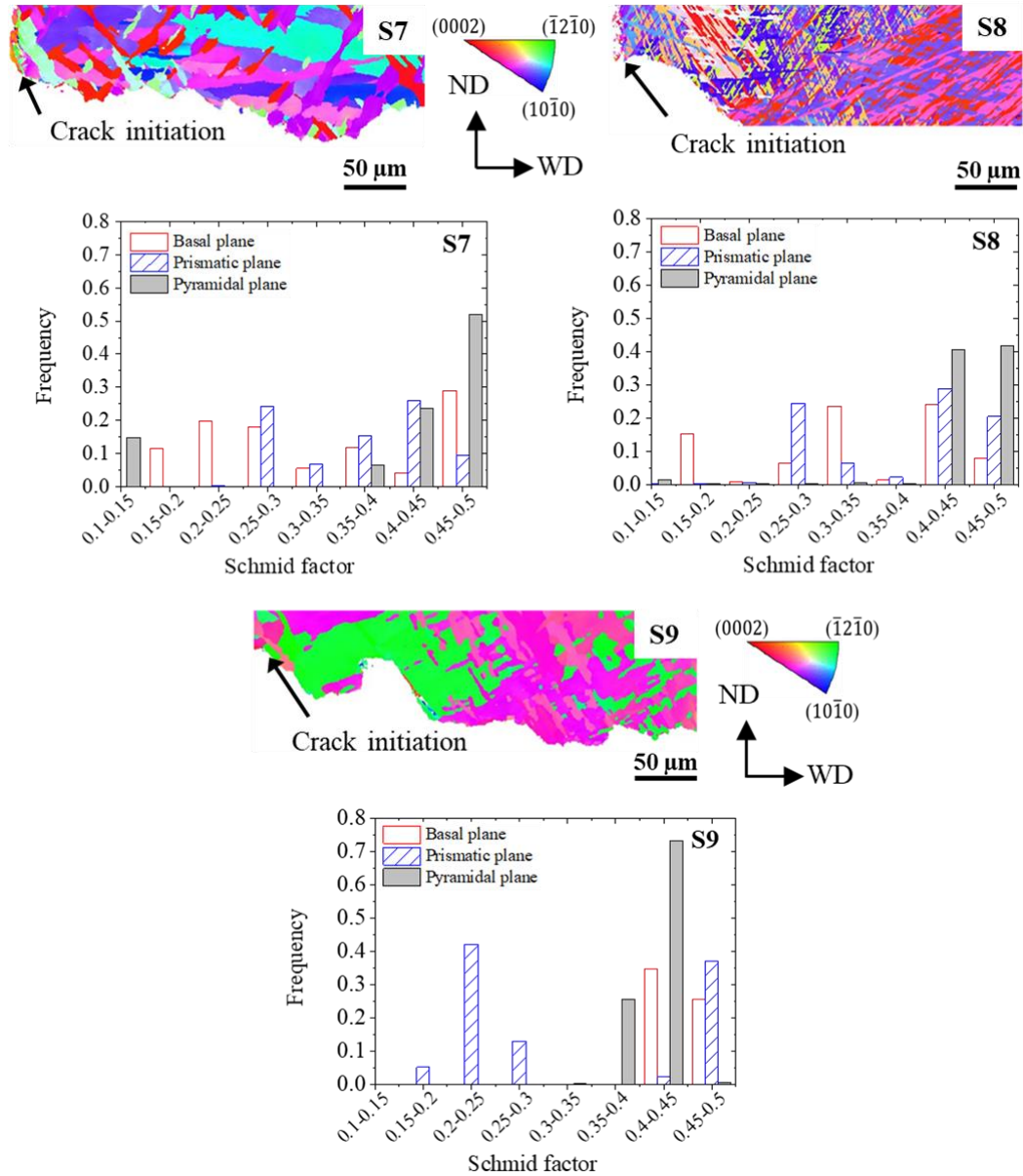


Figure 7.9: EBSD orientation maps of 500 MPa fractured samples showing crack initiation location and Schmid factor distribution analysis in S7, S8 and S9. The build and loading direction is parallel to TD. The number of cycles to failure for S7, S8 and S9 are 22×10^4 , 69×10^4 and 700×10^4 respectively.

Crack initiation, as well as the whole fatigue process, were controlled by cyclic plastic deformation. When the material was subjected to a large number of fatigue cycles, dislocation pileups occurred, and accumulation of pileups resulted in persistent slip bands (extrusions and intrusions), which were formed due to slip along the favourable slip plane. These extrusions and intrusions acted as micro notches or stress concentration locations and promoted additional slip that led to fatigue crack nucleation [125]. In Ti64, HCF strength, i.e. the resistance to crack initiation, depends primarily on the resistance to dislocation motion. Consequently, the slip length distance and the α colony size or α lath width dictates HCF strength [14,45]. When considering the influence of α lath width, it has been demonstrated that the increased α lath width would cause decreased fatigue life due to increased slip length. Similarly, when considering the colony size, the increased colony size would decrease fatigue life due to increased slip length [14]. Although both the α phase and β matrix will deform independently, slip can be easily transferred across the incoherent α/β interface resulting in the crack to initiate from the α phase [14].

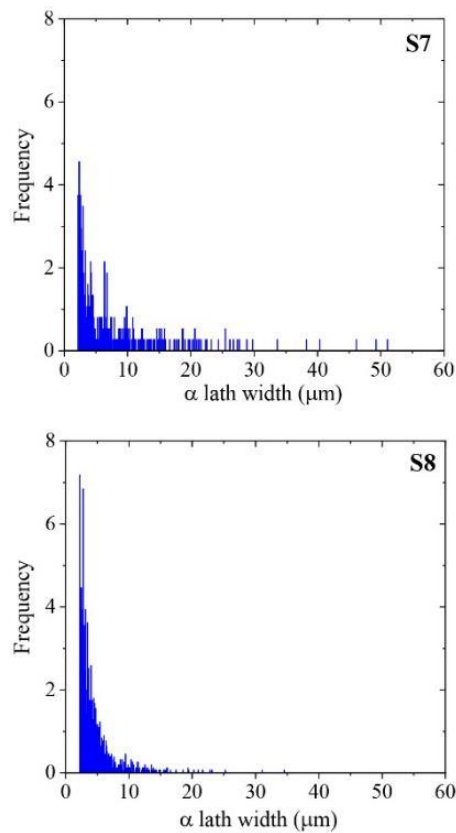


Figure 7.10: Distribution of α lath size obtained from EBSD analysis for tests S7 and S8

Therefore, a detailed analysis of the α lath width and the α colony size at the crack initiation location may provide further insights into the fatigue life scatter in S7 and S8. Although α lath width variation was observed for all samples in Figure 7.9a, a statistical distribution would provide further insights into the microstructure around the crack initiation site. The α lath width distribution was obtained from the EBSD. Analysis of S7 and S8 is presented in Figure 7.10. The graph of S7 presented in Figure 7.10 is skewed towards the right, showing that S7 has a considerably higher distribution of larger α laths, whereas S8 showed a large distribution of smaller α laths (skewed towards the left). Although S8 showed a lower frequency of pyramidal distribution, the presence of smaller α laths required higher stress/fatigue cycles to activate slip and to initiate a fatigue crack. The large α laths distribution has resulted in lower fatigue life in S7, confirming that both crystallographic orientations of α and α lath width distribution at and around the defect contribute to fatigue life. In contrast, larger defect size resulted in reduced fatigue life in S9.

7.4 Summary

The role of the microstructure and the crystallographic orientation has been investigated at and around the crack initiating defects, for both embedded and surface defects, by fracture surface analysis and the EBSD measurements. Based on the findings, the following conclusions are drawn:

The primary factors behind the fatigue life scatter due to the combined effect of the defect size, its location, and variations of the crystallographic orientation and microstructure at and around the crack initiation defect. The size of the defect alone cannot correlate with the fatigue life; hence the large scatter found in the S-N curves.

For the same defect size and at a similar location with the same applied stress, scatter in the fatigue life can be partially explained by the local variations on the crystallographic orientation of α . The samples with the higher distribution of Schmid factors for pyramidal slip systems had longer fatigue life due to the higher critical resolved shear stress required for the cyclic slip to occur.

Considering the microstructure influence, a large number of smaller α laths at and around the crack initiating defects contributed to longer fatigue life, and vice versa.

Suppose process-induced porosity defects cannot be eliminated in additive manufactured titanium alloys. In that case, the fatigue life could be improved by reducing the α lath width and creating a larger number of active pyramidal slip systems.

Chapter 8

Conclusions and future work

8.1 Conclusions

8.1.1 Small crack growth testing

For the fatigue life prediction based on fracture mechanics, it is proposed that small crack growth data should be used as the depth of surface waviness in the as-deposited WAAM Ti64 is in the sub-millimetre range. The small crack data of WAAM Ti64 is not available in the literature, so the experiment was designed to measure the small crack growth data as recommended by ASTM E647. It was observed that a small crack shows deviation and branching from the main path (perpendicular to the loading direction), which is associated with the variation in local microstructure and crystallographic texture. The optical microscope images of the notch root and the fracture surface analysis of the small crack sample showed the starter notch has a curvature with a diameter of 100 μm . Therefore, the Newman-Raju quarter-elliptical crack assumption could not be used to calculate the crack driving force, K . And so, to identify the K , an FE model has been developed for the current geometry and sample design. The K values were approx. 22% lower than the empirical solution proposed by Newman-Raju. Furthermore, the Hartman-Schijve variant of the NASGRO equation has been calibrating for WAAM Ti64, that allows using long crack data and a unified crack growth curve has been proposed to be used further for durability analysis of WAAM parts with inherent defects.

The modified Hartman-Schijve equation can be used as a unified crack growth rate law, and its material constants can be determined by long crack test data alone. The durability of the specimens can be predicted by the notch-fatigue approach and the fracture

mechanics approach using the modified Hartman-Schijve equation with EIFS as the initial crack length.

8.1.2 Fatigue behaviour of as-deposited WAAM Ti64

Among different metrology techniques, a form tracer is proposed to be the most suitable and robust technique to characterise the as-deposited WAAM surface. Three-point bending fatigue was performed to quantify the fatigue behaviour of as-deposited WAAM Ti64. The as-deposited surface was characterised by R_a , but due to the lack of correlation between R_a and the fatigue life noted in this study, the single “grove” has been characterised using the opening angle θ , depth of the notch d and radius of curvature r . The notch depth, d varies between 50 μm to 320 μm , the angle θ is between 167° to 175° and the radius of curvature, r ranges between 90 μm to 200 μm . It was further noted that if the ratio of r and t (thickness of the sample) is less than 0.03 ($r/t < 0.03$), and $t/(t-d)$ is less than 1.05 ($t/(t-d) < 1.05$), the θ dominates the stress concentration factor, K_t of the notch.

During the crack growth testing, the distribution of microstructure has influenced the crack propagation behaviour of as-deposited samples. The presence of prior β grain boundaries has affected the growth behaviour and has caused the lead crack to branch, which reduced the crack growth rate at the same applied stress intensity factor. Fracture surface analysis has revealed that the crack initiated at a single point in polished samples and propagated as a quarter-elliptical crack. In contrast, it is initiated from a single notch (experiencing maximum tensile load under three-point bending) and propagated as a ‘rectangular’ crack in the as-deposited samples. Further analysis of fracture surface has revealed the faceted fracture during the early stages of crack, a classic example of slip in α colonies with respect to the loading direction and dimples in the region of fast fracture.

The average surface roughness values (R_a) of as-deposited WAAM Ti64 is $26.8 \pm 2.8 \mu\text{m}$ and reduced the fatigue life by a factor of 1.2-1.7. However, no correlation could be made on individual samples based on R_a and fatigue life. So, the single notch was characterised using depth of the notch, d the opening angle θ and radius of curvature, r .

A good approximation of the surface waviness of as-deposited samples has been achieved from the finite element analysis. The notch depth, d varies between 50 μm to 320 μm , the angle θ is between 167° to 175° and the radius of curvature, r ranges between 90 μm to 200 μm however, if the ratio of r and t (thickness of the sample) is less than 0.03 ($r/t < 0.03$), and $t/(t-d)$ is less than 1.05 ($t/(t-d) < 1.05$), the θ seems dominates the stress concentration factor, K_t of the notch.

8.1.3 Fatigue life prediction methods

For fatigue life prediction, two modelling strategies, i.e., notch-fatigue and fracture mechanics, have been proposed and compared in this study. Both approaches follow a novel technique, i.e., in the case of notch-fatigue, metrology data has been directly used to create FE models. In contrast, for fracture mechanics, a unified curve has been proposed for WAAM Ti64 having sub-millimetre defects.

For the notch fatigue approach, a range of values representing the shallowest and deepest notches in the WAAM Ti64 build has been investigated, with K_t ranging between 1.25-1.75. The model has worked well for test samples under higher applied stresses while it over-estimated the fatigue life at lower applied stresses.

For the fracture mechanics approach, the centre notch can be treated as an initial crack and termed as EIFS. From the FE model, it has been noted that an empirical equation suggested in the literature can be used to calculate K . Since the crack length is in the sub-millimetre range, so the unified curve proposed from small crack testing has been used for fatigue life prediction, which has not been used in the literature for as-deposited WAAM Ti64. It has been noted that compared to other AM processes in literature, the Hartman-Schijve material constants are different for WAAM Ti64 due to the difference in the microstructure.

Both the notch fatigue and fracture mechanics models worked well for the current sample geometry. However, the fracture mechanics approach should be preferred over the notch-

stress approach despite being slightly conservative because the crack length is included in the model.

The surface waviness of as-deposited WAAM Ti64 can be characterised as an array of micro notches. The notch depth is used as the equivalent initial flaw size (EIFS) or initial crack size, which are in the sub-millimetre range.

8.1.4 Microstructure effect on fatigue test scatter

To further understand the scatter in fatigue life of WAAM Ti64, the microstructure and the crystallographic orientation at and around the crack initiating defects have been analysed. It has been concluded that the primary factors behind the fatigue life scatter is the combined effect of the defect size, its location, and variations of the crystallographic orientation and microstructure at and around the crack initiation defect.

The primary factors behind the fatigue life scatter due to the combined effect of the defect size, its location, and variations of the crystallographic orientation and microstructure at and around the crack initiation defect. The size of the defect alone cannot correlate with the fatigue life; hence the large scatter found in the *S-N* curves. For the same defect size and at a similar location with the same applied stress, scatter in the fatigue life can be partially explained by the local variations on the crystallographic orientation of α . The samples with the higher distribution of Schmid factors for pyramidal slip systems had longer fatigue life due to the higher critical resolved shear stress required for the cyclic slip to occur.

8.2 Future work

The research documented in this Thesis outlines the experimental and numerical modelling designed to identify the effect of process-induced defects and surface features on fatigue properties of WAAM Ti64. Nevertheless, there is still work that needs to be done to better understand the crack initiation and small crack propagation in AM Ti64. Some suggestions for further investigations based on the current findings are proposed below.

The proposed unified crack growth law for WAAM Ti64 could be used to analyse internal defects such as porosity and lack of fusion after identifying a suitable model to calculate the stress intensity factor in cylindrical samples. The modified Hartman-Schijve equation has been calibrated for one deposition strategy and validated by experimental data. The same calibration method can be used further for different deposition strategies, and a unified crack growth curve can be obtained.

The prediction models can be further calibrated and used to optimise the machining of as-deposited WAAM samples by guiding the depth of machining required to achieve the required fatigue life.

Although the current EBSD analysis of grains around the defect created the underlying understanding of crystallographic orientation on fatigue crack initiation, a detailed analysis of the role of microstructure on small crack propagation can be studied by in-situ mechanical testing with EBSD maps. It will give a better understanding of crack arrest and deviation. Furthermore, the crystal plasticity model can predict the fatigue crack initiation in the presence of defects and the role of microstructure and crystallographic texture at and around the defects.

References

- [1] Romano S, Brandão A, Gumpinger J, Gschweidl M, Beretta S, Fousová M, et al. Comparative study of fatigue properties of Ti-6Al-4V specimens built by electron beam melting (EBM) and selective laser melting (SLM). *Metall Mater Trans A* 2018;131:102638. <https://doi.org/10.1016/j.tafmec.2020.102638>.
- [2] Leuders S, Thöne M, Riemer A, Niendorf T, Tröster T, Richard HA, et al. On the mechanical behaviour of titanium alloy TiAl6V4 manufactured by selective laser melting: Fatigue resistance and crack growth performance. *Int J Fatigue* 2013;48:300–7. <https://doi.org/10.1016/j.ijfatigue.2012.11.011>.
- [3] Chastand V, Quaegebeur P, Maia W, Charkaluk E. Comparative study of fatigue properties of Ti-6Al-4V specimens built by electron beam melting (EBM) and selective laser melting (SLM). *Mater Charact* 2018;143:76–81. <https://doi.org/10.1016/j.matchar.2018.03.028>.
- [4] Fatemi A, Molaei R, Sharifimehr S, Phan N, Shamsaei N. Multiaxial fatigue behavior of wrought and additive manufactured Ti-6Al-4V including surface finish effect. *Int J Fatigue* 2017;100:347–66. <https://doi.org/10.1016/j.ijfatigue.2017.03.044>.
- [5] Greitemeier D, Palm F, Syassen F, Melz T. Fatigue performance of additive manufactured TiAl6V4 using electron and laser beam melting. *Int J Fatigue* 2017;94:211–7. <https://doi.org/10.1016/j.ijfatigue.2016.05.001>.
- [6] Ding D, Wu B, Pan Z, Qiu Z, Li H. Wire arc additive manufacturing of Ti6AL4V using active interpass cooling. *Mater Manuf Process* 2020;35:845–51. <https://doi.org/10.1080/10426914.2020.1732414>.
- [7] Williams SW, Martina F, Addison AC, Ding J, Pardal G, Colegrove P. Wire + Arc additive manufacturing. *Mater Sci Technol* 2016;32:641–7. <https://doi.org/10.1179/1743284715Y.0000000073>.
- [8] Yehorov Y, da Silva LJ, Scotti A. Balancing WAAM production costs and wall surface quality through parameter selection: A case study of an Al-Mg5 alloy multilayer-non-oscillated single pass wall. *J Manuf Mater Process* 2019;3. <https://doi.org/10.3390/jmmp3020032>.
- [9] Lockett H, Ding J, Williams S, Martina F. Design for Wire + Arc Additive Manufacture: design rules and build orientation selection. *J Eng Des* 2017;4828:1–31. <https://doi.org/10.1080/09544828.2017.1365826>.
- [10] Dirisu P, Supriyo G, Martina F, Xu X, Williams S. Wire plus arc additive manufactured functional steel surfaces enhanced by rolling. *Int J Fatigue* 2020;130:105237. <https://doi.org/10.1016/j.ijfatigue.2019.105237>.

- [11] Paskual A, Álvarez P, Suárez A. Study on arc welding processes for high deposition rate additive manufacturing. *Procedia CIRP* 2018;68:358–62. <https://doi.org/10.1016/j.procir.2017.12.095>.
- [12] Wang F, Williams S, Colegrove P, Antonysamy AA. Microstructure and mechanical properties of wire and arc additive manufactured Ti-6Al-4V. *Metall Mater Trans A Phys Metall Mater Sci* 2013;44:968–77. <https://doi.org/10.1007/s11661-012-1444-6>.
- [13] Biswal R, Zhang X, Syed AK, Awd M, Ding J, Walther F, et al. Criticality of porosity defects on the fatigue performance of wire + arc additive manufactured titanium alloy. *Int J Fatigue* 2019;122:208–17. <https://doi.org/10.1016/j.ijfatigue.2019.01.017>.
- [14] Shamir M, Syed AK, Janik V, Biswal R, Zhang X. The role of microstructure and local crystallographic orientation near porosity defects on the high cycle fatigue life of an additive manufactured Ti-6Al-4V. *Mater Charact* 2020;169:110576. <https://doi.org/10.1016/j.matchar.2020.110576>.
- [15] Strano G, Hao L, Everson RM, Evans KE. Surface roughness analysis, modelling and prediction in selective laser melting. *J Mater Process Tech* 2013;213:589–97. <https://doi.org/10.1016/j.jmatprotec.2012.11.011>.
- [16] Samadian K, Waele W De. Fatigue crack growth model incorporating surface waviness for wire + arc additively manufactured components. *Procedia Struct Integr* 2020;28:1846–55. <https://doi.org/10.1016/j.prostr.2020.11.008>.
- [17] Yadollahi A, Mahtabi MJ, Khalili A, Doude HR, Newman JC. Fatigue life prediction of additively manufactured material: Effects of surface roughness, defect size, and shape. *Fatigue Fract Eng Mater Struct* 2018:1–13. <https://doi.org/10.1111/ffe.12799>.
- [18] Zhang J, Fatemi A. Surface roughness effect on multiaxial fatigue behavior of additive manufactured metals and its modeling. *Theor Appl Fract Mech* 2019;103:102260. <https://doi.org/10.1016/j.tafmec.2019.102260>.
- [19] Guilherme AS, Pessanha Henriques GE, Zavanelli RA, Mesquita MF. Surface roughness and fatigue performance of commercially pure titanium and Ti-6Al-4V alloy after different polishing protocols. *J Prosthet Dent* 2005;93:378–85. <https://doi.org/10.1016/j.prosdent.2005.01.010>.
- [20] Chan KS, Koike M, Mason RL, Okabe T. Fatigue life of titanium alloys fabricated by additive layer manufacturing techniques for dental implants. *Metall Mater Trans A* 2013;44:1010–22. <https://doi.org/10.1007/s11661-012-1470-4>.
- [21] Persenot T, Burr A, Martin G, Buffiere JY, Dendievel R, Maire E. Effect of build orientation on the fatigue properties of as-built Electron Beam Melted Ti-6Al-4V alloy. *Int J Fatigue* 2019;118:65–76. <https://doi.org/10.1016/j.ijfatigue.2018.08.006>.
- [22] Tato W, Blunt L, Llavori I, Aginagalde A, Townsend A, Zabala A. Surface integrity of

- additive manufacturing parts: A comparison between optical topography measuring techniques. *Procedia CIRP* 2020;87:403–8. <https://doi.org/10.1016/j.procir.2020.02.082>.
- [23] Kahlin M, Ansell H, Basu D, Kerwin A, Newton L, Smith B, et al. Improved fatigue strength of additively manufactured Ti6Al4V by surface post processing. *Int J Fatigue* 2020;134:105497. <https://doi.org/10.1016/j.ijfatigue.2020.105497>.
- [24] Sanaei N, Fatemi A. Analysis of the effect of surface roughness on fatigue performance of powder bed fusion additive manufactured metals. *Theor Appl Fract Mech* 2020;108:102638. <https://doi.org/10.1016/j.tafmec.2020.102638>.
- [25] Elad N, Shneck R, Yeheskel O, Frage N. Materials Science & Engineering A Fatigue of AlSi10Mg specimens fabricated by additive manufacturing selective laser melting (AM-SLM). *Mater Sci Eng A* 2017;704:229–37. <https://doi.org/10.1016/j.msea.2017.08.027>.
- [26] Eric W, Claus E, Shafaqat S, Frank W. High cycle fatigue (HCF) performance of Ti-6Al-4V alloy processed by selective laser melting. *Adv Mater Res* 2013;816–817:134–9. <https://doi.org/10.4028/www.scientific.net/AMR.816-817.134>.
- [27] Edwards P, Ramulu M. Fatigue performance evaluation of selective laser melted Ti-6Al-4V. *Mater Sci Eng A* 2014;598:327–37. <https://doi.org/10.1016/j.msea.2014.01.041>.
- [28] Masuo H, Tanaka Y, Morokoshi S, Yagura H, Uchida T, Yamamoto Y, et al. Influence of defects, surface roughness and HIP on the fatigue strength of Ti-6Al-4V manufactured by additive manufacturing. *Int J Fatigue* 2018;117:163–79. <https://doi.org/10.1016/j.ijfatigue.2018.07.020>.
- [29] Biswal R, Syed AK, Zhang X. Assessment of the effect of isolated porosity defects on the fatigue performance of additive manufactured titanium alloy. *Addit Manuf* 2018;23:433–42. <https://doi.org/10.1016/j.addma.2018.08.024>.
- [30] Dinh TD, Vanwalleghem J, Xiang H, Erdelyi H, Craeghs T, Paepegem W Van. A unified approach to model the effect of porosity and high surface roughness on the fatigue properties of additively manufactured Ti6-Al4-V alloys. *Addit Manuf* 2020;33:101139. <https://doi.org/10.1016/j.addma.2020.101139>.
- [31] Greitemeier D, Dalle Donne C, Syassen F, Eufinger J, Melz T. Effect of surface roughness on fatigue performance of additive manufactured Ti-6Al-4V. *Mater Sci Technol* 2015;32:1743284715Y.000. <https://doi.org/10.1179/1743284715Y.0000000053>.
- [32] Jones R, Molaei R, Fatemi A, Peng D, Phan N. A note on computing the growth of small cracks in AM Ti-6Al-4V. *Procedia Struct Integr* 2020;28:364–9. <https://doi.org/10.1016/j.prostr.2020.10.043>.
- [33] Lincoln JW, Melliore RA. Economic life determination for a military aircraft. vol. 36. 1999. <https://doi.org/10.2514/2.2512>.

- [34] Zhai Y, Galarraga H, Lados DA. Microstructure, static properties, and fatigue crack growth mechanisms in Ti-6Al-4V fabricated by additive manufacturing: LENS and EBM. *Eng Fail Anal* 2016;69:3–14. <https://doi.org/10.1016/j.engfailanal.2016.05.036>.
- [35] Zhai Y, Lados DA, Brown EJ, Vigilante GN. Fatigue crack growth behavior and microstructural mechanisms in Ti-6Al-4V manufactured by laser engineered net shaping. *Int J Fatigue* 2016;93:51–63. <https://doi.org/10.1016/j.ijfatigue.2016.08.009>.
- [36] ASTM E647-15: Standard test method for measurement of fatigue crack growth rates 2015:1–49. <https://doi.org/10.1520/E0647-15E01.2>.
- [37] Main B, Jones M, Barter S. The practical need for short fatigue crack growth rate models. *Int J Fatigue* 2021;142:105980. <https://doi.org/10.1016/j.ijfatigue.2020.105980>.
- [38] Jones R, Molent L, Walker K. Fatigue crack growth in a diverse range of materials 2012;40:43–50. <https://doi.org/10.1016/j.ijfatigue.2012.01.004>.
- [39] Schra RJHW and L. Short cracks and durability analysis of the Fokker 100 wing, fuselage structure. *Short Fatigue Cracks* 1992;ESIS 13:1–27.
- [40] Papangelo A, Guarino R, Pugno N, Ciavarella M. On unified crack propagation laws. *Eng Fract Mech* 2019;207:269–76. <https://doi.org/10.1016/j.engfracmech.2018.12.023>.
- [41] Iliopoulos A, Jones R, Michopoulos J, Phan N, Singh Raman R. Crack growth in a range of additively Manufactured aerospace structural materials. *Aerospace* 2018;5:118. <https://doi.org/10.3390/aerospace5040118>.
- [42] Lutjering G. *Engineering Materials and Processes*. Second. Hamburg: Springer; 2007.
- [43] Titanium alloys for aeroengine and airframe applications 2002. <https://www.azom.com/article.aspx?ArticleID=1569>.
- [44] Campbell, Flake C J. *Manufacturing technology for aerospace structural materials*. First. Elsevier B.V; 2006.
- [45] Liu S, Shin YC. Additive manufacturing of Ti6Al4V alloy: A review. *Mater Des* 2019;164:107552. <https://doi.org/10.1016/J.MATDES.2018.107552>.
- [46] Allen J. An investigation into the comparative costs of additive manufacture vs. machine from solid for aero engine parts. vol. 17. 2006.
- [47] Huang R, Riddle M, Graziano D, Warren J, Das S, Nimbalkar S, et al. Energy and emissions saving potential of additive manufacturing : the case of lightweight aircraft components. *J Clean Prod* 2016;135:1559–70. <https://doi.org/10.1016/j.jclepro.2015.04.109>.

- [48] Keaveney S, Shmeliov A, Nicolosi V, Dowling DP. Investigation of process by-products during the Selective Laser Melting of Ti6Al4V powder. *Addit Manuf* 2020;36:101514. <https://doi.org/10.1016/j.addma.2020.101514>.
- [49] Galarraga H, Warren RJ, Lados DA, Dehoff RR, Kirka MM, Nandwana P. Effects of heat treatments on microstructure and properties of Ti-6Al-4V ELI alloy fabricated by electron beam melting (EBM). *Mater Sci Eng A* 2017;685:417–28. <https://doi.org/10.1016/j.msea.2017.01.019>.
- [50] Sampson B. Finland flies 3D-printed engine parts for the first time 2018. <https://www.aerospacemanufacturinganddesign.com/article/bae-systems-3d-printed-metal-parts-flown-011014/>.
- [51] GKN aerospace announces new £32M global technology centre in Bristol. Press Release 2021. <https://www.gknaerospace.com/en/newsroom/news-releases/2018/gkn-aerospace-announces-new-32m-global-technology-centre-in-bristol/>.
- [52] Hanna Rose Mendoza. Marines embrace 3D printing for production of replacement parts 2018. <https://3dprint.com/210788/marines-3dp-replacement-parts/>.
- [53] ASTM International. F2792-12a - Standard Terminology for Additive Manufacturing Technologies. *Rapid Manuf Assoc* 2013;10–2. <https://doi.org/10.1520/F2792-12A.2>.
- [54] Gong X, Anderson T, Chou K. Review on powder - based electron beam additive manufacturing technology. *Manuf Rev* 2014;1:1–9. <https://doi.org/10.1051/mfreview/2014001>.
- [55] Herzog D, Seyda V, Wycisk E, Emmelmann C. Additive manufacturing of metals. *Acta Mater* 2016;117:371–92. <https://doi.org/10.1016/j.actamat.2016.07.019>.
- [56] Frazier WE. Metal Additive Manufacturing: A Review. *J Mater Eng Perform* 2014;23:1917–28. <https://doi.org/10.1007/s11665-014-0958-z>.
- [57] DebRoy T, Wei HL, Zuback JS, Mukherjee T, Elmer JW, Milewski JO, et al. Additive manufacturing of metallic components – Process, structure and properties. *Prog Mater Sci* 2018;92:112–224. <https://doi.org/10.1016/j.pmatsci.2017.10.001>.
- [58] Venturini G, Montevecchi F, Scippa A, Campatelli G. Optimization of WAAM deposition patterns for T-crossing features. *Procedia CIRP* 2016;55:95–100. <https://doi.org/10.1016/j.procir.2016.08.043>.
- [59] Busachi A, Erkoyuncu J, Colegrove P, Martina F, Ding J. “ Designing a WAAM based manufacturing system for defence applications .” *Procedia CIRP* 2015;37:48–53. <https://doi.org/10.1016/j.procir.2015.08.085>.
- [60] Lütjering G, Williams JC, Gysler A. Microstructure and mechanical properties of titanium

- alloys. *Microstruct. Prop. Mater.*, vol. 2, 2000, p. 1–74. https://doi.org/10.1142/9789812793959_0001.
- [61] Knobbe H, Köster P, Christ HJ, Fritzen CP, Riedler M. Initiation and propagation of short fatigue cracks in forged Ti6Al4V. *Procedia Eng* 2010;2:931–40. <https://doi.org/10.1016/j.proeng.2010.03.101>.
- [62] Åkerfeldt P, Colliander MH, Pederson R, Antti ML, Hörnqvist M, Pederson R, et al. Electron backscatter diffraction characterization of fatigue crack growth in laser metal wire deposited Ti-6Al-4V. *Mater Charact* 2018;135:245–56. <https://doi.org/10.1016/j.matchar.2017.11.041>.
- [63] Khadar A, Ahmad B, Guo H, Machry T, Eatock D, Meyer J, et al. An experimental study of residual stress and direction-dependence of fatigue crack growth behaviour in as-built and stress-relieved selective-laser-melted Ti6Al4V. *Mater Sci Eng A* 2019;755:246–57. <https://doi.org/10.1016/j.msea.2019.04.023>.
- [64] Baufeld B, Brandl E, Van Der Biest O. Wire based additive layer manufacturing: Comparison of microstructure and mechanical properties of Ti-6Al-4V components fabricated by laser-beam deposition and shaped metal deposition. *J Mater Process Technol* 2011;211:1146–58. <https://doi.org/10.1016/j.jmatprotec.2011.01.018>.
- [65] Szost BA, Terzi S, Martina F, Boisselier D, Prytuliak A, Pirling T, et al. A comparative study of additive manufacturing techniques: Residual stress and microstructural analysis of CLAD and WAAM printed Ti-6Al-4V components. *Mater Des* 2016;89:559–67. <https://doi.org/10.1016/j.matdes.2015.09.115>.
- [66] Callister W. *Materials Science and Engineering*. 8th ed. Wiley; 2010.
- [67] Åkerfeldt P, Pederson R, Antti ML. A fractographic study exploring the relationship between the low cycle fatigue and metallurgical properties of laser metal wire deposited Ti-6Al-4V. *Int J Fatigue* 2016;87:245–56. <https://doi.org/10.1016/j.ijfatigue.2016.02.011>.
- [68] Kasperovich G, Hausmann J. Improvement of fatigue resistance and ductility of TiAl6V4 processed by selective laser melting. *J Mater Process Technol* 2015;220:202–14. <https://doi.org/10.1016/j.jmatprotec.2015.01.025>.
- [69] Jafari D, Vaneker THJ, Gibson I. Wire and arc additive manufacturing: Opportunities and challenges to control the quality and accuracy of manufactured parts. *Mater Des* 2021;202:109471. <https://doi.org/10.1016/j.matdes.2021.109471>.
- [70] Khairallah SA, Anderson AT, Rubenchik A, King WE. Laser powder-bed fusion additive manufacturing: Physics of complex melt flow and formation mechanisms of pores, spatter, and denudation zones. *Acta Mater* 2016;108:36–45. <https://doi.org/10.1016/j.actamat.2016.02.014>.
- [71] Galarraga H, Lados DA, Dehoff RR, Kirka MM, Nandwana P. Effects of the

- microstructure and porosity on properties of Ti-6Al-4V ELI alloy fabricated by electron beam melting (EBM). *Addit Manuf* 2016;10:47–57. <https://doi.org/10.1016/j.addma.2016.02.003>.
- [72] Biswal R, Zhang X, Shamir M, Al Mamun A, Awd M, Walther F, et al. Interrupted fatigue testing with periodic tomography to monitor porosity defects in wire + arc additive manufactured Ti-6Al-4V. *Addit Manuf* 2019;28:517–27. <https://doi.org/10.1016/j.addma.2019.04.026>.
- [73] Gunther J, Krewerth D, Lippmann T, Leuders S, Troster T, Weidner A, et al. Fatigue life of additively manufactured Ti-6Al-4V in the very high cycle fatigue regime. *Int J Fatigue* 2017;94:236–45. <https://doi.org/10.1016/j.ijfatigue.2016.05.018>.
- [74] Tamas-Williams S, Withers PJ, Todd I, Prangnell PB. The influence of porosity on fatigue crack initiation in additively manufactured titanium components. *Sci Rep* 2017;7:7308. <https://doi.org/10.1038/s41598-017-06504-5>.
- [75] Åkerfeldt P. Additive Manufacturing of Ti-6Al-4V: Relationship between Microstructure, Defects and Mechanical Properties. Lulea University of Technology, 2016.
- [76] Rye Y, Sun SD, Liu Q, Brandt M, Qian M. Influence of deposition strategy on the microstructure and fatigue properties of laser metal deposited Ti-6Al-4V powder on Ti-6Al-4V substrate. *Int J Fatigue* 2020;130:105236. <https://doi.org/10.1016/j.ijfatigue.2019.105236>.
- [77] Bauereiß A, Scharowsky T, Körner C. Defect generation and propagation mechanism during additive manufacturing by selective beam melting. *J Mater Process Technol* 2014;214:2497–504. <https://doi.org/10.1016/j.jmatprotec.2014.05.002>.
- [78] Kasperovich G, Haubrich J, Gussone J, Requena G. Correlation between porosity and processing parameters in TiAl6V4 produced by selective laser melting. *JMADE* 2016;105:160–70. <https://doi.org/10.1016/j.matdes.2016.05.070>.
- [79] Dilip JJS, Zhang S, Pal D, Stucker B. Influence of processing parameters on the evolution of melt pool, porosity, and microstructures in Ti-6Al-4V alloy parts fabricated by selective laser melting. *Prog Addit Manuf* 2017;2:157–67. <https://doi.org/10.1007/s40964-017-0030-2>.
- [80] Bagehorn S, Wehr J, Maier HJ. Application of mechanical surface finishing processes for roughness reduction and fatigue improvement of additively manufactured Ti-6Al-4V parts. *Int J Fatigue* 2017;102:135–42. <https://doi.org/10.1016/j.ijfatigue.2017.05.008>.
- [81] Walker KF, Liu Q, Brandt M. Evaluation of fatigue crack propagation behaviour in Ti-6Al-4V manufactured by selective laser melting. *Int J Fatigue* 2017;104:302–8. <https://doi.org/10.1016/j.ijfatigue.2017.07.014>.
- [82] Tamas-Williams S, Zhao H, Léonard F, Derguti F, Todd I, Prangnell PB. XCT analysis

- of the influence of melt strategies on defect population in Ti-6Al-4V components manufactured by Selective Electron Beam Melting. *Mater Charact* 2015;102:47–61. <https://doi.org/10.1016/j.matchar.2015.02.008>.
- [83] Elsayed M, Ghazy M, Youssef Y, Essa K. Optimization of SLM process parameters for Ti6Al4V medical implants. *Rapid Prototyp J* 2019;25:433–47.
- [84] Gong H, Rafi K, Starr T, Stucker B. The effects of processing parameters on defect regularity in Ti-6Al-4V parts fabricated by selective laser melting and electron beam melting. *Proc. Solid Free. Fabr. Symp.*, 2013.
- [85] Gockel J, Sheridan L, Koerper B, Whip B. The influence of additive manufacturing processing parameters on surface roughness and fatigue life. *Int J Fatigue* 2019;124:380–8. <https://doi.org/10.1016/j.ijfatigue.2019.03.025>.
- [86] Xiong J, Li Y, Li R, Yin Z. Influences of process parameters on surface roughness of multi-layer single-pass thin-walled parts in GMAW-based additive manufacturing. *J Mater Process Technol* 2018;252:128–36. <https://doi.org/10.1016/j.jmatprotec.2017.09.020>.
- [87] Yu W, Leong S, Kai C, Tian X. Influence of re-melting on surface roughness and porosity of AlSi10Mg parts fabricated by selective laser melting. *J Alloys Compd* 2019;792:574–81. <https://doi.org/10.1016/j.jallcom.2019.04.017>.
- [88] Han Q, Jiao Y. Effect of heat treatment and laser surface remelting on AlSi10Mg alloy fabricated by selective laser melting. *Int J Adv Manufaturing Technol* 2019;102:3315–24.
- [89] Murakami Y. Stress concentration. *Met Fatigue* 2019;3:13–27. <https://doi.org/10.1016/b978-0-12-813876-2.00002-9>.
- [90] Chastand V, Tezenas A, Cadoret Y, Quaegebeur P, Maia W, Charkaluk E. Fatigue characterization of titanium Ti-6Al-4V samples produced by additive manufacturing. *Procedia Struct Integr* 2016;2:3168–76. <https://doi.org/10.1016/j.prostr.2016.06.395>.
- [91] Seifi M, Gorelik M, Waller J, Hrabe N, Shamsaei N, Daniewicz S, et al. Progress towards metal additive manufacturing standardization to support qualification and certification. *Jom* 2017;69:439–55. <https://doi.org/10.1007/s11837-017-2265-2>.
- [92] Wadell H. Volume, shape, roundness of quartz particles. *J Geol* 1935;43:250–80.
- [93] Seifi M, Salem A, Satko D, Shaffer J, Lewandowski JJ. Defect distribution and microstructure heterogeneity effects on fracture resistance and fatigue behavior of EBM Ti-6Al-4V. *Int J Fatigue* 2017;94:263–87. <https://doi.org/10.1016/j.ijfatigue.2016.06.001>.
- [94] G. Z, E. C, P. S, J. K. Application of X-ray CT method for discontinuity and porosity

detection in 316L stainless steel parts produced with SLM technology. *Arch Civ Mech Eng* 2014;14:608–14.

- [95] Sanaei N, Fatemi A, Phan N. Defect characteristics and analysis of their variability in metal L-PBF additive manufacturing. *Mater Des* 2019;182:108091. <https://doi.org/10.1016/j.matdes.2019.108091>.
- [96] Kabir MR, Richter H. Modeling of processing-induced pore morphology in an additively-manufactured Ti-6Al-4V alloy. *Materials (Basel)* 2017;10:1–15. <https://doi.org/10.3390/ma10020145>.
- [97] Townsend A, Senin N, Blunt L, Leach RK, Taylor JS. Surface texture metrology for metal additive manufacturing: a review. *Precis Eng* 2016;46:34–47. <https://doi.org/10.1016/j.precisioneng.2016.06.001>.
- [98] Wycisk E, Solbach A, Siddique S, Herzog D, Walther F. Effects of defects in laser additive manufactured Ti-6Al-4V on fatigue properties. *Phys Procedia* 2014;56:371–8. <https://doi.org/10.1016/j.phpro.2014.08.120>.
- [99] Dinda GP, Song L, Mazumder J. Fabrication of Ti-6Al-4V scaffolds by direct metal deposition. *Metall Mater Trans A* 2008;39A:2914–22. <https://doi.org/10.1007/s11661-008-9634-y>.
- [100] Keist JS, Palmer TA. Role of geometry on properties of additively manufactured Ti-6Al-4V structures fabricated using laser based directed energy deposition. *JMADE* 2016;106:482–94. <https://doi.org/10.1016/j.matdes.2016.05.045>.
- [101] Palanivel S, Dutt AK, Faierson EJ, Mishra RS. A spatially dependent properties in a laser additive manufactured Ti-6Al-6V component. *Mater Sci Eng A* 2016;654:39–52. <https://doi.org/10.1016/j.msea.2015.12.021>.
- [102] Simonelli M, Tse YY, Tuck C. Effect of the build orientation on the mechanical properties and fracture modes of SLM Ti-6Al-4V. *Mater Sci Eng A* 2014;616:1–11. <https://doi.org/10.1016/j.msea.2014.07.086>.
- [103] Zhao X, Li S, Zhang M, Liu Y, Sercombe TB, Wang S, et al. Comparison of the microstructures and mechanical properties of Ti – 6Al – 4V fabricated by selective laser melting and electron beam melting. *JMADE* 2016;95:21–31. <https://doi.org/10.1016/j.matdes.2015.12.135>.
- [104] Vayssette B, Saintier N, Brugger C, May MEI. Surface roughness effect of SLM and EBM Ti-6Al-4V on multiaxial high cycle fatigue. *Theor Appl Fract Mech* 2020;108:102581. <https://doi.org/10.1016/j.tafmec.2020.102581>.
- [105] Aydinöz ME, Brenne F, Schaper M, Schaak C, Tillmann W, Nellesen J. On the microstructural and mechanical properties of post-treated additively manufactured Inconel 718 superalloy under quasi-static and cyclic loading. *Mater Sci Eng A* 2016;669:246–58.

<https://doi.org/10.1016/j.msea.2016.05.089>.

- [106] Nicoletto G, Konečná R, Frkáň M, Riva E. Surface roughness and directional fatigue behavior of as-built EBM and DMLS Ti6Al4V. *Int J Fatigue* 2018;116:140–8. <https://doi.org/10.1016/j.ijfatigue.2018.06.011>.
- [107] Fatemi A, Molaei R, Sharifimehr S, Shamsaei N, Phan N. Torsional fatigue behavior of wrought and additive manufactured Ti-6Al-4V by powder bed fusion including surface finish effect. *Int J Fatigue* 2017;99:187–201. <https://doi.org/10.1016/j.ijfatigue.2017.03.002>.
- [108] Kahlin M, Ansell H, Moverare JJ. Fatigue behaviour of additive manufactured Ti6Al4V, with as-built surfaces, exposed to variable amplitude loading. *Int J Fatigue* 2017;103:353–62. <https://doi.org/10.1016/j.ijfatigue.2017.06.023>.
- [109] C. Rice R, Jackson JL, Bakuckas J, Thompson S. *Metallic materials properties development and standardization*. 2008.
- [110] Dinh TD, Han S, Yaghoubi V, Xiang H, Erdelyi H, Craeghs T, et al. Modeling detrimental effects of high surface roughness on the fatigue behavior of additively manufactured Ti-6Al-4V alloys. *Int J Fatigue* 2021;144:106034. <https://doi.org/10.1016/j.ijfatigue.2020.106034>.
- [111] Jones R, Raman RKS, Iliopoulos AP, Michopoulos JG, Phan N, Peng D. Additively manufactured Ti-6Al-4V replacement parts for military aircraft. *Int J Fatigue* 2019;124:227–35. <https://doi.org/10.1016/j.ijfatigue.2019.02.041>.
- [112] Hooreweder B VAN, Boonen R, Moens D, Kruth J. On the determination of fatigue properties of Ti6Al4V produced by selective on the determination of fatigue properties of Ti6Al4V produced by selective laser melting 2012. <https://doi.org/10.2514/6.2012-1733>.
- [113] Benedetti M, Santus C. Notch fatigue and crack growth resistance of Ti-6Al-4V ELI additively manufactured via selective laser melting : A critical distance approach to defect sensitivity. *Int J Fatigue* 2019;121:281–92. <https://doi.org/10.1016/j.ijfatigue.2018.12.020>.
- [114] Pegues JW, Shamsaei N, Roach MD, Williamson RS. Fatigue life estimation of additive manufactured parts in the as-built surface condition. *Mater Des Process Commun* 2019;1:e36. <https://doi.org/10.1002/mdp2.36>.
- [115] Vayssette B, Saintier N, Brugger C, El May M, Pessard E. Numerical modelling of surface roughness effect on the fatigue behavior of Ti-6Al-4V obtained by additive manufacturing. *Int J Fatigue* 2019;123:180–95. <https://doi.org/10.1016/j.ijfatigue.2019.02.014>.
- [116] Nakatani M, Masuo H, Tanaka Y, Murakami Y. Effect of Surface Roughness on Fatigue Strength of Ti-6Al-4V Alloy Manufactured by Additive Manufacturing. *Procedia Struct Integr* 2019;19:294–301. <https://doi.org/10.1016/j.prostr.2019.12.032>.

- [117] Yamashita Y, Murakami T, Mihara R, Okada M, Murakami Y. Defect analysis and fatigue design basis for Ni-based superalloy 718 manufactured by selective laser melting. *Int J Fatigue* 2018;117:485–95. <https://doi.org/10.1016/j.ijfatigue.2018.08.002>.
- [118] Romano S, Brückner-foit A, Brandão A, Gumpinger J, Ghidini T, Beretta S. Fatigue properties of AlSi10Mg obtained by additive manufacturing : Defect-based modelling and prediction of fatigue strength. *Eng Fract Mech* 2018;187:165–89. <https://doi.org/10.1016/j.engfracmech.2017.11.002>.
- [119] Jones R, Michopoulos JG, Iliopoulos AP, Singh Raman RK, Phan N, Nguyen T. Representing crack growth in additively manufactured Ti-6Al-4V. *Int J Fatigue* 2018;116:610–22. <https://doi.org/10.1016/j.ijfatigue.2018.07.019>.
- [120] Sanaei N, Fatemi A. Defect-based fatigue life prediction of L-PBF additive manufactured metals. *Eng Fract Mech* 2021;244:107541. <https://doi.org/10.1016/j.engfracmech.2021.107541>.
- [121] Romano S, Patriarca L, Foletti S, Beretta S. LCF behaviour and a comprehensive life prediction model for AlSi10Mg obtained by SLM. *Int J Fatigue* 2018;117:47–62. <https://doi.org/10.1016/j.ijfatigue.2018.07.030>.
- [122] Schijve J. Four lectures on fatigue crack growth. I. Fatigue crack growth and fracture mechanics. *Eng Fract Mech* 1979;11:169–81.
- [123] ASTM-E466. Standard practice for conducting force controlled constant amplitude axial fatigue tests of metallic materials 2018;i:1–6. <https://doi.org/10.1520/E0466-15.2>.
- [124] ASTM-E606. Standard test method for strain controlled fatigue testing 2017;92:1–16. <https://doi.org/10.1520/E0606-04E01>. Copyright.
- [125] Suresh S. *Fatigue of materials*. Second. Cambridge: Cambridge University Press; 1998.
- [126] Hertzberg RW. Chapter 12: Cyclic stress and strain fatigue. *Deform. Fract. Mech. Eng. Mater*. Fourth, John Wiley & Sons; 1996.
- [127] Pilkey WD, Pilkey DF. *Peterson’s Stress Concentration Factors*. Third. 2008.
- [128] Timoshenko S, Goodier JN. *Theory of Elasticity*. First. York: McGraw-Hill; 1951.
- [129] Kahlin M, Ansell H, Moverare JJ. Fatigue behaviour of notched additive manufactured Ti6Al4V with as-built surfaces. *Int J Fatigue* 2017;101:51–60. <https://doi.org/10.1016/j.ijfatigue.2017.04.009>.
- [130] Anderson T. Chapter 2: Linear elastic fracture mechanics. *Fract. Mech. Fundam. Appl*. Third, Boca Raton: Taylor & Francis Group; 2005.

- [131] Paris P, Erdogan F. A critical analysis of crack propagation laws. *J Basic Eng* 1963;85:528–524.
- [132] Newman Jr. JC. The merging of fatigue and fracture mechanics concepts : A historical perspective. *Prog Aerosp Sci* 1998;34:347–90.
- [133] Suresh S. Chapter 15: Small fatigue cracks. *Fatigue Mater. Second*, New York: Cambridge University Press; 1998.
- [134] Kitagawa H, Takahashi S. Applicability of fracture mechanics to very small cracks or the cracks in early stage. *Proc. Second Int. Conf. Mech. Behav. Mater.*, 1976, p. 627–31.
- [135] Wang K, Wang F, Cui W, Hayat T, Ahmad B. Prediction of short fatigue crack growth of Ti-6Al-4V. *Fatigue Fract Eng Mater Struct* 2014;37:1075–86. <https://doi.org/10.1111/ffe.12177>.
- [136] Taylor D, Knott JF. Fatigue crack propagation of short cracks: the effect of microstructure. *Fatigue Eng Mater Struct* 1981;4:147–55.
- [137] Tanaka K, Nakai Y, Yamashita M. Fatigue growth threshold of small cracks. *International J Fract* 1981;17:519–33.
- [138] Xie Y, Gong M, Zhou Q, Li Q, Wang F, Zeng X, et al. Effect of microstructure on fatigue crack growth of wire arc additive manufactured Ti-6Al-4V. *Mater Sci Eng A* 2021;826:141942. <https://doi.org/10.1016/j.msea.2021.141942>.
- [139] Sandgren HR, Zhai Y, Lados DA, Shade PA, Schuren JC, Groeber MA, et al. Characterization of fatigue crack growth behavior in LENS fabricated Ti-6Al-4V using high-energy synchrotron x-ray microtomography. *Addit Manuf* 2016;12:132–41. <https://doi.org/10.1016/j.addma.2016.09.002>.
- [140] Zhang X, Martina F, Ding J, Wang X, Williams SW. Fracture toughness and fatigue crack growth rate properties in wire + arc additive manufactured Ti-6Al-4V. *Fatigue Fract Eng Mater Struct* 2017;40:790–803. <https://doi.org/10.1111/ffe.12547>.
- [141] Syed AK, Zhang X, Davis AE, Kennedy JR, Martina F, Ding J, et al. Effect of deposition strategies on fatigue crack growth behaviour of wire + arc additive manufactured titanium alloy Ti-6Al-4V. *Mater Sci Eng A* 2021;814:141194. <https://doi.org/10.1016/j.msea.2021.141194>.
- [142] Xie Y, Gao M, Wang F, Zhang C, Hao K, Wang H, et al. Anisotropy of fatigue crack growth in wire arc additive manufactured Ti-6Al-4V. *Mater Sci Eng A* 2018;709:265–9. <https://doi.org/10.1016/j.msea.2017.10.064>.
- [143] Liu F, He C, Chen Y, Zhang H, Wang Q, Liu Y. Effects of defects on tensile and fatigue behaviors of selective laser melted titanium alloy in very high cycle regime. *Int J Fatigue*

2020;140:105795. <https://doi.org/10.1016/j.ijfatigue.2020.105795>.

- [144] Sanaei N, Fatemi A. Defect-based multiaxial fatigue life prediction of L-PBF additive manufactured metals. *Fatigue Fract Eng Mater Struct* 2021;1897–915. <https://doi.org/10.1111/ffe.13449>.
- [145] Iliopoulos AP, Jones R, Michopoulos JG, Phan N, Rans C. Further studies into crack growth in additively manufactured materials. *Materials (Basel)* 2020;13:5–10. <https://doi.org/10.3390/ma13102223>.
- [146] Waddell M, Walker K, Bandyopadhyay R, Kapoor K, Mallory A, Xiao X, et al. Small fatigue crack growth behavior of Ti-6Al-4V produced via selective laser melting: In situ characterization of a 3D crack tip interactions with defects. *Int J Fatigue* 2020;137:105638. <https://doi.org/10.1016/j.ijfatigue.2020.105638>.
- [147] Qian G, Jian Z, Pan X, Berto F. In-situ investigation on fatigue behaviors of Ti-6Al-4V manufactured by selective laser melting. *Int J Fatigue* 2020;133:105424. <https://doi.org/10.1016/j.ijfatigue.2019.105424>.
- [148] Zhu L, Hu X, Jiang R, Song Y, Qu S. An investigation of small fatigue crack behavior in titanium alloy TC4 under different stress levels. *Proc Inst Mech Eng Part G J Aerosp Eng* 2019;0:1–12. <https://doi.org/10.1177/0954410019852867>.
- [149] Forman R, Keary V, Engle R. Numerical analysis of crack propagation in cyclic-loaded structures. *J Basic Eng* 1967;89:459–64.
- [150] Hartman A, Schijve J. The effects of environment and load frequency on the crack propagation law for macro fatigue crack growth in aluminium alloys. *Eng Fract Mech* 1970;1:615–31. [https://doi.org/10.1016/0013-7944\(70\)90003-2](https://doi.org/10.1016/0013-7944(70)90003-2).
- [151] Priddle E. High cycle fatigue crack propagation under random and constant amplitude loadings. *Int J Press Vessel Pip* 1976;4:89–117.
- [152] Molent L, Jones R. The influence of cyclic stress intensity threshold on fatigue life scatter. *Int J Fatigue* 2016;82:748–56. <https://doi.org/10.1016/j.ijfatigue.2015.10.006>.
- [153] Schwalbe KH. On the beauty of analytical models for fatigue crack propagation and fracture - A personal historical review. *J ASTM Int* 2010;7:4–73. <https://doi.org/10.1520/JAI102713>.
- [154] Ali K, Peng D, Jones R, Singh RRR, Zhao XL, McMillan AJ, et al. Crack growth in a naturally corroded bridge steel. *Fatigue Fract Eng Mater Struct* 2017;40:1117–27. <https://doi.org/10.1111/ffe.12568>.
- [155] Parry L, Ashcroft IA, Wildman RD. Understanding the effect of laser scan strategy on residual stress in selective laser melting through thermo-mechanical simulation. *Addit*

- Manuf 2016;12:1–15. <https://doi.org/10.1016/j.addma.2016.05.014>.
- [156] Vastola G, Zhang G, Pei QX, Zhang YW. Controlling of residual stress in additive manufacturing of Ti6Al4V by finite element modeling. *Addit Manuf* 2016;12:231–9. <https://doi.org/10.1016/j.addma.2016.05.010>.
- [157] Bailey NS, Tan W, Shin YC. Predictive modeling and experimental results for residual stresses in laser hardening of AISI 4140 steel by a high power diode laser. *Surf Coatings Technol* 2009;203:2003–12. <https://doi.org/10.1016/j.surfcoat.2009.01.039>.
- [158] Bailey NS, Katinas C, Shin YC. Laser direct deposition of AISI H13 tool steel powder with numerical modeling of solid phase transformation, hardness, and residual stresses. *J Mater Process Technol* 2017;247:223–33. <https://doi.org/10.1016/j.jmatprotec.2017.04.020>.
- [159] Edwards P, Ramulu M. Materials Science & Engineering A Fatigue performance evaluation of selective laser melted Ti – 6Al – 4V. *Mater Sci Eng A* 2014;598:327–37.
- [160] Liu S, Shin YC. Additive manufacturing of Ti6Al4V alloy: A review. *Mater Des* 2019;164:107552. <https://doi.org/10.1016/j.matdes.2018.107552>.
- [161] Zhang J, Wang X, Paddea S, Zhang X. Fatigue crack propagation behaviour in wire+arc additive manufactured Ti-6Al-4V: Effects of microstructure and residual stress. *Mater Des* 2016;90:551–61. <https://doi.org/10.1016/j.matdes.2015.10.141>.
- [162] Zhang X, Syed AK, Biswal R, Martina F, Ding J, Williams S. High cycle fatigue and fatigue crack growth rate in additive manufactured titanium alloys. *Int Comm Aeronaut Fatigue* 2019:31–42.
- [163] Beretta S, Romano S. A comparison of fatigue strength sensitivity to defects for materials manufactured by AM or traditional processes. *Int J Fatigue* 2017;94:178–91. <https://doi.org/10.1016/j.ijfatigue.2016.06.020>.
- [164] Newman Jr. JC, Raju IS. Stress-intensity factor equations for cracks in three-dimensional finite bodies. *ASTM Spec Tech Publ* 1983;1:238–65. <https://doi.org/10.1520/stp37074s>.
- [165] ASTM E8/E8M standard test methods for tension testing of metallic materials 1. *Annu B ASTM Stand* 4 2010:1–27. <https://doi.org/10.1520/E0008>.
- [166] Qin CH, Zhang XC, Ye S, Tu ST. Grain size effect on multi-scale fatigue crack growth mechanism of Nickel-based alloy GH4169. *Eng Fract Mech* 2015;142:140–53. <https://doi.org/10.1016/j.engfracmech.2015.06.003>.
- [167] Ho A, Zhao H, Fellowes JW, Martina F, Davis AE, Prangnell PB. On the origin of microstructural banding in Ti-6Al4V wire-arc based high deposition rate additive manufacturing. *Acta Mater* 2019;166:306–23.

<https://doi.org/10.1016/j.actamat.2018.12.038>.

- [168] Kobryn P., Semiatin S. Microstructure and texture evolution during solidification processing of Ti-6Al-4V. *J Mater Process Technol* 2003;135:330–9. [https://doi.org/10.1016/S0924-0136\(02\)00865-8](https://doi.org/10.1016/S0924-0136(02)00865-8).
- [169] Kelly SM, Kampe SL. Microstructural evolution in laser-deposited multilayer Ti-6Al-4V builds: Part I. Microstructural characterization. *Metall Mater Trans A* 2004;35:1861–7. <https://doi.org/10.1007/s11661-004-0094-8>.
- [170] Al-Bermani SS, Blackmore ML, Zhang W, Todd I. The origin of microstructural diversity, texture, and mechanical properties in electron beam melted Ti-6Al-4V 2010;41:3422–34. <https://doi.org/10.1007/s11661-010-0397-x>.
- [171] Donoghue J, Antonysamy AA, Martina F, Colegrove PA, Williams SW, Prangnell PB. The effectiveness of combining rolling deformation with wire-arc additive manufacture on β -grain refinement and texture modification in Ti-6Al-4V. *Mater Charact* 2016;114:103–14. <https://doi.org/10.1016/j.matchar.2016.02.001>.
- [172] Martina F, Colegrove PA, Williams SW, Meyer J. Microstructure of interpass rolled wire + arc additive manufacturing Ti-6Al-4V components. *Metall Mater Trans A Phys Metall Mater Sci* 2015;46:6103–18. <https://doi.org/10.1007/s11661-015-3172-1>.
- [173] Antonysamy AA, Meyer J, Prangnell PB. Effect of build geometry on the β -grain structure and texture in additive manufacture of Ti6Al4V by selective electron beam melting. *Mater Charact* 2013;84:153–68. <https://doi.org/10.1016/j.matchar.2013.07.012>.
- [174] Colegrove PA, Donoghue J, Martina F, Gu J, Prangnell P, Hönnige J. Application of bulk deformation methods for microstructural and material property improvement and residual stress and distortion control in additively manufactured components. *Scr Mater* 2016;2. <https://doi.org/10.1016/j.scriptamat.2016.10.031>.
- [175] Syed AK, Zhang X, Caballero A, Shamir M, Williams S. Influence of deposition strategies on tensile and fatigue properties in a wire + arc additive manufactured Ti-6Al-4V. *Int J Fatigue* 2021;149:106268. <https://doi.org/10.1016/j.ijfatigue.2021.106268>.
- [176] Bantounas I, Lindley TC, Rugg D, Dye D. Effect of microtexture on fatigue cracking in Ti-6Al-4V. *Acta Mater* 2007;55:5655–65. <https://doi.org/10.1016/j.actamat.2007.06.034>.
- [177] Suresh S, Ritchie RO. Propagation of short fatigue cracks. *Int Met Rev* 1984;29:445–75. <https://doi.org/10.1179/imtr.1984.29.1.445>.
- [178] Xie Y, Gong M, Luo Z, Li Q, Gao M, Wang F, et al. Effect of microstructure on short fatigue crack growth of wire arc additive manufactured Ti-6Al-4V. *Mater Charact* 2021:104743. <https://doi.org/10.1016/j.matchar.2021.111183>.

- [179] ABAQUS, Analysis user's manual. Version 6.14, Dassault Systemes Simulia, Inc. 2014.
- [180] Jolles M, Tortoriello V. Geometry variations during fatigue growth of surface flaws. *ASTM STP 791 Fract Mech* 1983:297–307.
- [181] Newman Jr. J, Raju I. Prediction of fatigue crack-growth pattern and lives in three-dimensional cracked bodies. *International Congress on Fracture (ICF)*; 1984. <https://doi.org/10.1016/B978-1-4832-8440-8.50151-4>.
- [182] Ritchie RO, Boyce BL, Campbell JP, Roder O, Thompson AW, Milligan WW. Thresholds for high-cycle fatigue in a turbine engine Ti-6Al-4V alloy. *Int J Fatigue* 1999;21:653–62. [https://doi.org/10.1016/S0142-1123\(99\)00024-9](https://doi.org/10.1016/S0142-1123(99)00024-9).
- [183] Caton MJ, John R, Porter WJ, Burba ME. Stress ratio effects on small fatigue crack growth in Ti-6Al-4V. *Int J Fatigue* 2012;38:36–45. <https://doi.org/10.1016/j.ijfatigue.2011.11.004>.
- [184] ASTM. Standard Practice for Conducting Force Controlled Constant Amplitude Axial Fatigue Tests of Metallic Materials. *Test* 2002;03:4–8. <https://doi.org/10.1520/E0466-07.2>.
- [185] Formtracer SV-C3200 / 4500 Series Hybrid Measuring Instrument for Surface. n.d.
- [186] An introduction to non-contact surface metrology. 2013.
- [187] ASTM B946. (2016). Standard Test Method for Surface Finish of Powder Metallurgy (PM) Products. ASTM International, n.d. <https://doi.org/10.1520/B0946-11R16.2>.
- [188] Kline M. *Calculus: An intuitive and Physical Approach*. Second. Courier Corporation; 1998.
- [189] Schijve J, editor. *Fatigue and Scatter*. *Fatigue Struct. Mater.*, Dordrecht: Springer Netherlands; 2009, p. 373–94. https://doi.org/10.1007/978-1-4020-6808-9_12.
- [190] Chern AH, Nandwana P, McDaniels R, Dehoff RR, Liaw PK, Tryon R, et al. Build orientation, surface roughness, and scan path influence on the microstructure, mechanical properties, and flexural fatigue behavior of Ti-6Al-4V fabricated by electron beam melting. *Mater Sci Eng A* 2020;772:138740. <https://doi.org/10.1016/j.msea.2019.138740>.
- [191] Pegues J, Roach M, Scott Williamson R, Shamsaei N. Surface roughness effects on the fatigue strength of additively manufactured Ti-6Al-4V. *Int J Fatigue* 2018;116:543–52. <https://doi.org/10.1016/j.ijfatigue.2018.07.013>.
- [192] Broek D, Rice JR. Chapter 3: The elastic crack-tip stress field. *Elem. Eng. Fract. Mech*. Third, Hague: Martinus Nijhoff; 1982. <https://doi.org/10.1115/1.3423697>.

- [193] ASTM E1820: Standard Test Method for Measurement of Fracture Toughness 1 2019:1–65. <https://doi.org/10.1520/E1820-18AE01>.
- [194] Li P, Warner DH, Fatemi A, Phan N. Critical assessment of the fatigue performance of additively manufactured Ti-6Al-4V and perspective for future research. *Int J Fatigue* 2016;85:130–43. <https://doi.org/10.1016/j.ijfatigue.2015.12.003>.
- [195] Fatemi A, Molaei R, Simsiriwong J, Sanaei N, Pegues J, Torries B, et al. Fatigue behaviour of additive manufactured materials : An overview of some recent experimental studies on Ti - 6Al - 4V considering various processing and loading direction effects 2019:1–19. <https://doi.org/10.1111/ffe.13000>.
- [196] de Formanoir C, Michotte S, Rigo O, Germain L, Godet S. Electron beam melted Ti-6Al-4V: Microstructure, texture and mechanical behavior of the as-built and heat-treated material. *Mater Sci Eng A* 2016;652:105–19. <https://doi.org/10.1016/j.msea.2015.11.052>.
- [197] Murakami Y, Endo M. Effects of hardness and crack geometry on ΔK_{th} of small cracks. *Mater Sci* 1986:275–93.
- [198] Pilchak AL, Williams REA, Williams JC. Crystallography of fatigue crack initiation and growth in fully lamellar Ti-6Al-4V. *Metall Mater Trans A Phys Metall Mater Sci* 2010;41:106–24. <https://doi.org/10.1007/s11661-009-0064-2>.
- [199] Sinha V, Mills MJ, Williams JC. Crystallography of fracture facets in a near-alpha titanium alloy. *Metall Mater Trans A* 2006;37:2015–26. <https://doi.org/10.1007/s11661-006-0144-5>.
- [200] Warwick JLWLW, Coakley J, Raghunathan SLL, Talling RJJ, Dye D. Effect of texture on load partitioning in Ti-6Al-4V. *Acta Mater* 2012;60:4117–27. <https://doi.org/10.1016/j.actamat.2012.03.039>.
- [201] Bantounas I, Dye D, Lindley TC. The Effect of Grain Orientation on Fracture Morphology during the High Cycle Fatigue of Ti-6Al-4V. *Acta Mater* 2009;57:3951–62. <https://doi.org/10.1016/j.actamat.2009.04.018>.
- [202] Bridier F, McDowell DL, Villechaise P, Mendez J. Crystal plasticity modeling of slip activity in Ti-6Al-4V under high cycle fatigue loading. *Int J Plast* 2009;25:1066–82. <https://doi.org/10.1016/j.ijplas.2008.08.004>.
- [203] Hémerly S, Nizou P, Villechaise P. In situ SEM investigation of slip transfer in Ti-6Al-4V: Effect of applied stress. *Mater Sci Eng A* 2018;709:277–84. <https://doi.org/10.1016/j.msea.2017.10.058>.

Appendix

A1.1

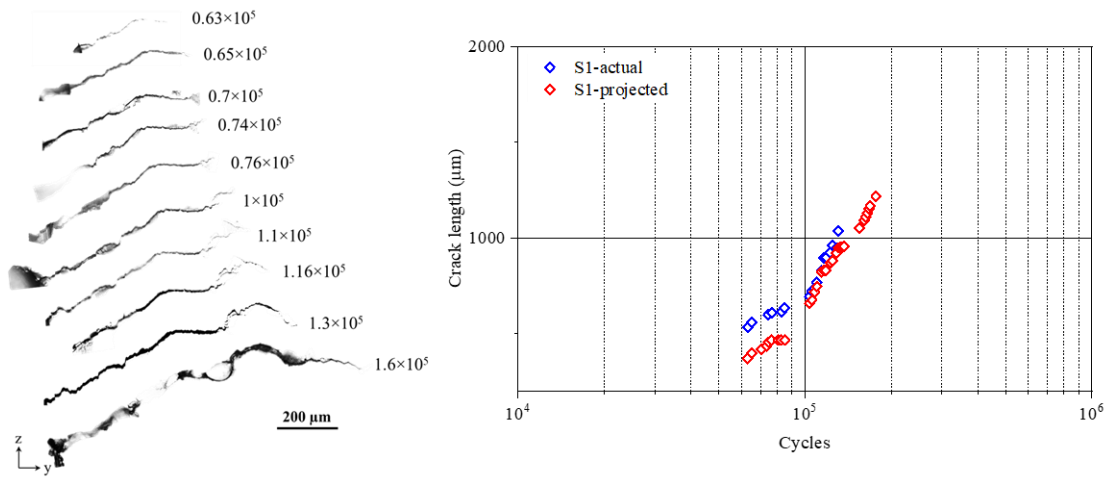


Figure A1.1: Schematic of small crack evolution of S1 with a vs. N data of actual and projected crack lengths. [Notch length is not included in a vs. N graph]

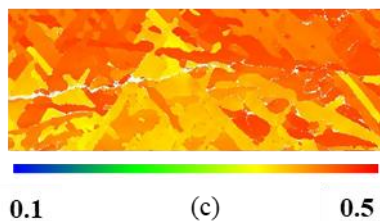
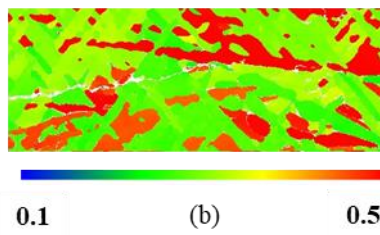
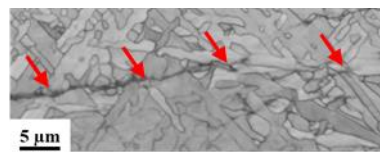


Figure A1.2: (a) High-resolution image showing small crack arrest (b) Prismatic slip distribution around the crack showing less prismatic planes activity (c) pyramidal slip distribution around the crack, showing more pyramidal slip planes activity.

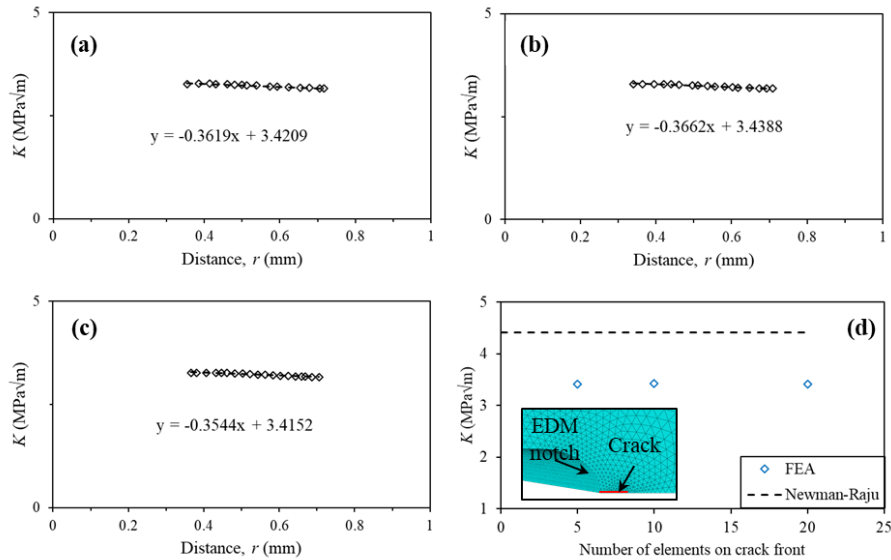


Figure A1.3: Figure A1: Stress intensity factor calculation of crack length 1 (CL-1) using displacement extrapolation with a different number of elements around the notch and crack front; (a) 5 elements, (b) 10 elements, (c) 20 elements, (d) mesh sensitivity analysis showing mesh convergence from FEA model and the difference between Newman-Raju solution and FEA model.

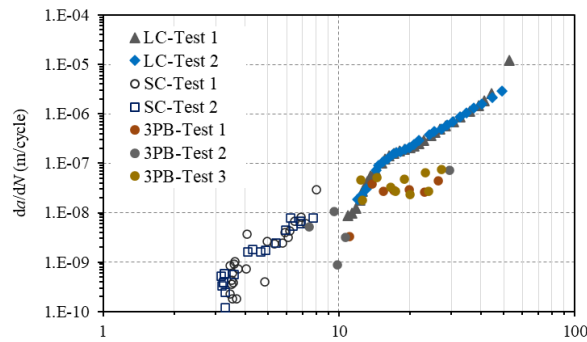
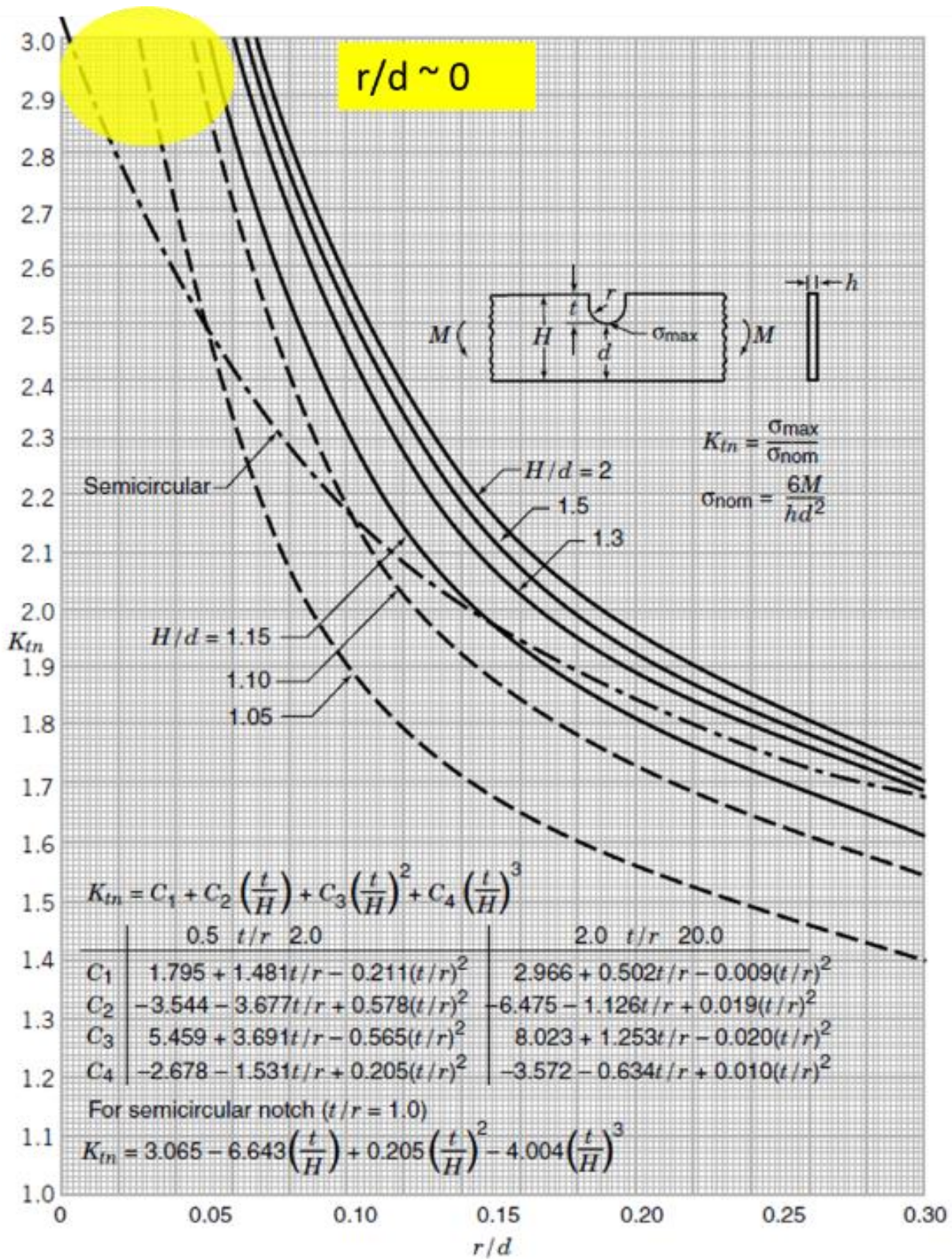


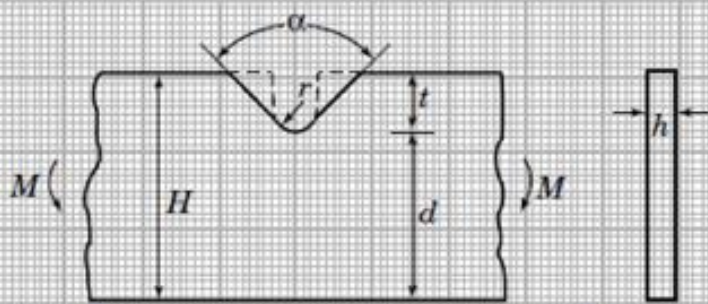
Figure A1.4: da/dN vs. ΔK of 3PB samples together with long crack and small crack (standard test) data.

Table A1: Detailed data of each sample tested in as-built surface condition.

Sr. no.	Sample tag	Applied nominal stress (MPa)	Cycles to failure	$2c$ (mm)	r (mm)	notch depth, a (mm)	Surface roughness, R_a (μm)	α (degrees)	K_t
1	S1-B1	300	296000	1.99	0.20	0.08	34.60	170.70	1.21
2	S2-B1	300	238000	2.54	0.01	0.10	38.69	171.28	1.60
3	S3-B1	300	318179	2.82	0.12	0.12	26.16	170.12	1.43
4	S5-B1	380	126737	1.28	0.12	0.05	58.29	171.09	1.62
5	S6-B1	420	63794	1.78	0.11	0.09	46.42	168.47	1.43
6	S7-B1	380	96875	1.61	0.07	0.07	34.80	170.70	1.60
7	S3-B2	600	11564	1.76	0.38	0.12	21.50	164.48	1.62
8	S4-B2	600	11730	2.17	0.29	0.12	26.30	167.60	1.67
9	S5-B2	600	24472	3.27	0.93	0.06	22.50	175.96	1.20
10	S6-B2	420	62606	1.69	0.32	0.07	28.60	170.27	1.60
11	S7-B2	420	48853	1.92	0.33	0.14	25.30	163.25	1.67
12	S1-B3	600	10882	1.40	0.05	0.06	24.00	169.75	1.72
13	S2-B3	600	13510	3.30	0.05	0.19	27.60	167.05	1.75
14	S3-B3	500	20893	1.75	0.14	0.14	23.60	162.07	1.93
15	S4-B3	500	27136	1.67	0.13	0.09	25.58	167.69	1.66
16	S1-B4	500	25575	3.02	0.15	0.06	26.00	175.75	1.19
17	S2-B4	500	26709	2.09	0.27	0.20	24.70	157.90	1.86
18	S4-B4	600	7313	3.10	0.40	0.29	26.50	158.81	1.83
19	S5-B4	600	8755	2.70	0.29	0.32	23.50	152.95	2.01
20	S6-B4	500	19567	3.10	0.22	0.31	25.20	157.61	1.83
21	S7-B4	500	34460	2.80	0.33	0.12	32.50	170.45	1.40
22	S8-B4	500	29463	2.20	0.33	0.11	32.60	168.54	1.48

A1.2





K_{tn} = Stress concentration for straight-sided notch with semicircular bottom (U notch), (Dashed lines in above sketch)

$K_{t\alpha}$ = Stress concentration for notch of angle α , with other dimensions the same.

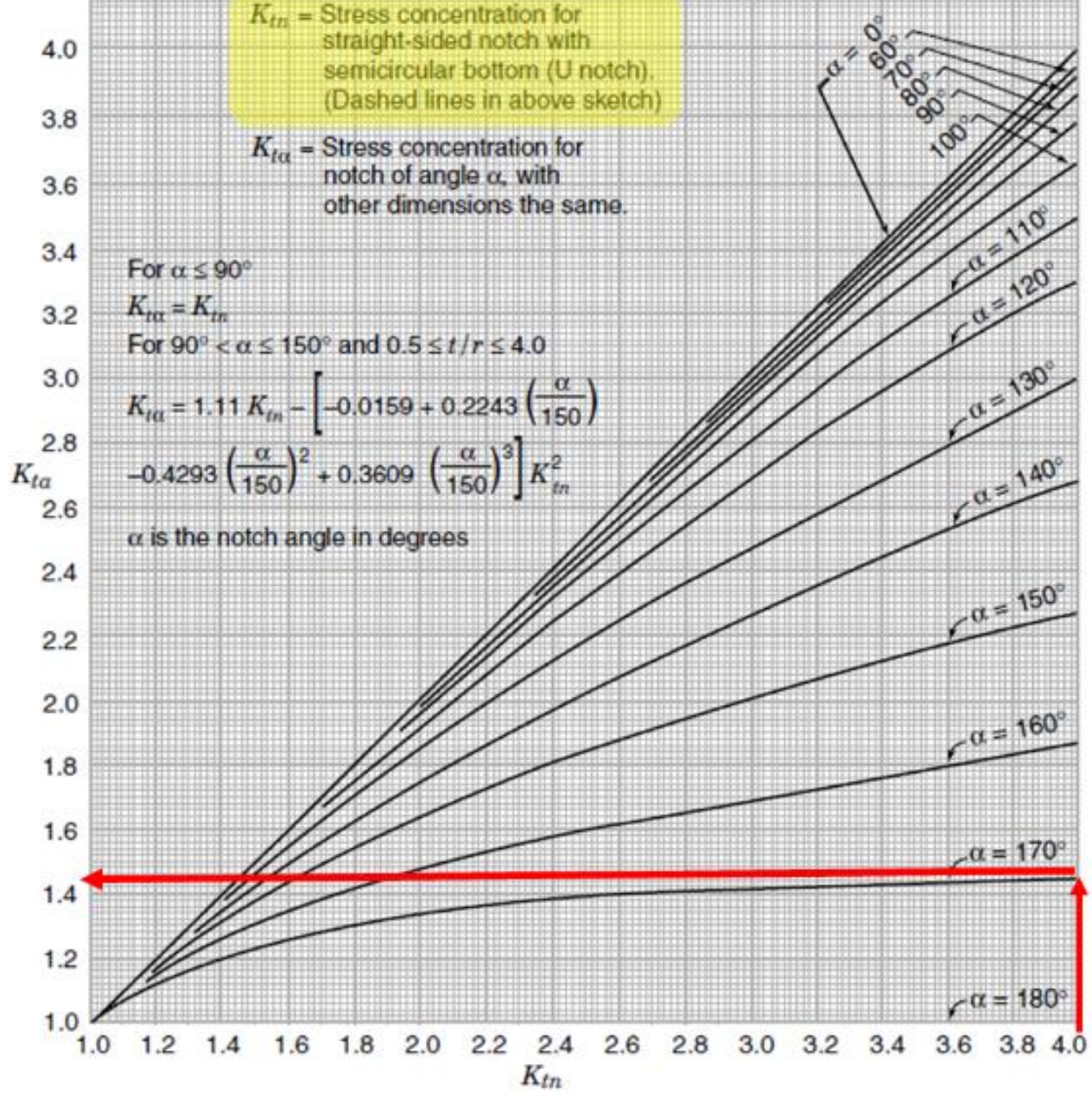
For $\alpha \leq 90^\circ$

$$K_{t\alpha} = K_{tn}$$

For $90^\circ < \alpha \leq 150^\circ$ and $0.5 \leq t/r \leq 4.0$

$$K_{t\alpha} = 1.11 K_{tn} - \left[-0.0159 + 0.2243 \left(\frac{\alpha}{150} \right) - 0.4293 \left(\frac{\alpha}{150} \right)^2 + 0.3609 \left(\frac{\alpha}{150} \right)^3 \right] K_{tn}^2$$

α is the notch angle in degrees



A1.3

Materials Characterization 169 (2020) 110576



Contents lists available at [ScienceDirect](#)

Materials Characterization

journal homepage: www.elsevier.com/locate/matchar



The role of microstructure and local crystallographic orientation near porosity defects on the high cycle fatigue life of an additive manufactured Ti-6Al-4V



This item has been removed due to 3rd Party Copyright. The unabridged version of the thesis can be found in the Lanchester Library, Coventry University.

Statement of contribution to the following publication

Paper title: The role of microstructure and local crystallographic orientation near porosity defects on the high cycle fatigue life of an additive manufactured Ti-6Al-4V

Publication details: Materials Characterization, Volume 169, Nov 2020, 110576

Authors: Muhammad Shamir, Abdul Khadar Syed, Vit Janik, Romali Biswal, Xiang Zhang

Affiliation: Institute for Future Transport and Cities, Faculty of Engineering, Environment and Computing, Coventry University, Coventry CV1 5FB

Author 1: Muhammad Shamir

- Conceived and designed the analysis
- Investigation and data collection
- Formal analysis
- Writing- Original draft preparation

Sign:



Author 2: Abdul Khadar Syed

- Investigation and data collection
- Formal analysis
- Writing- Original draft preparation

Sign:



Author 3: Vit Janik

- Conceived and designed the analysis
- Investigation
- Supervision

Sign:



Author 4: Romali Biswal

- Investigation and data collection
- Formal analysis

Sign:



Author 5: Xiang Zhang

- Supervision
- Resources
- Writing- Reviewing and Editing
- Funding acquisition

Sign:

